

REPORT DOCUMENTATION PAGE			Form Approved OMB No. 0704-0188	
Public reporting burden for this collection of information is estimated to average 1 hour per response, including the time for reviewing instructions, searching existing data sources, gathering and maintaining the data needed, and completing and reviewing the collection of information. Send comments regarding this burden estimate or any other aspect of this collection of information, including suggestions for reducing this burden, to Washington Headquarters Services, Directorate for Information Operations and Reports, 1215 Jefferson Davis Highway, Suite 1204, Arlington, VA 22202-4302, and to the Office of Management and Budget, Paperwork Reduction Project (0704-0188), Washington, DC 20503.				
1. AGENCY USE ONLY (Leave blank)		2. REPORT DATE 24.Oct.99	3. REPORT TYPE AND DATES COVERED THESIS	
4. TITLE AND SUBTITLE SIMULATION OF INTERNAL DAMPING IN A ROTATING SYSTEM SUPPORTED BY MAGNETIC BEARINGS			5. FUNDING NUMBERS	
6. AUTHOR(S) CAPT CERMINARO ANTHONY M				
7. PERFORMING ORGANIZATION NAME(S) AND ADDRESS(ES) TUFTS UNIVERSITY			8. PERFORMING ORGANIZATION REPORT NUMBER	
9. SPONSORING/MONITORING AGENCY NAME(S) AND ADDRESS(ES) THE DEPARTMENT OF THE AIR FORCE AFIT/CIA, BLDG 125 2950 P STREET WPAFB OH 45433			10. SPONSORING/MONITORING AGENCY REPORT NUMBER FY99-321	
11. SUPPLEMENTARY NOTES				
12a. DISTRIBUTION AVAILABILITY STATEMENT Unlimited distribution In Accordance With AFI 35-205/AFIT Sup 1			12b. DISTRIBUTION CODE	
13. ABSTRACT (Maximum 200 words)				
<div style="display: flex; justify-content: space-between; align-items: center;"> <div style="text-align: center;"> DISTRIBUTION STATEMENT A Approved for Public Release Distribution Unlimited </div> <div style="font-size: 2em; font-weight: bold;">19991116 104</div> </div>				
14. SUBJECT TERMS			15. NUMBER OF PAGES 88	
			16. PRICE CODE	
17. SECURITY CLASSIFICATION OF REPORT	18. SECURITY CLASSIFICATION OF THIS PAGE	19. SECURITY CLASSIFICATION OF ABSTRACT	20. LIMITATION OF ABSTRACT	

SIMULATION OF INTERNAL DAMPING IN A ROTATING SYSTEM SUPPORTED BY MAGNETIC BEARINGS

A thesis submitted by

Anthony Michael Cerminaro

In partial fulfillment of the requirements for the degree of

Master of Science

in

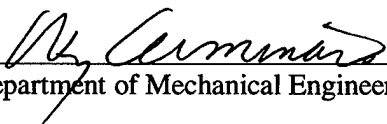
Mechanical Engineering

TUFTS UNIVERSITY

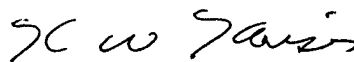
May 1999

© 1999 Anthony Michael Cerminaro

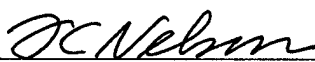
Signature of Author _____


Department of Mechanical Engineering

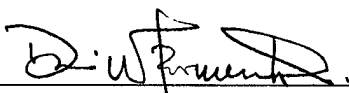
Accepted by _____


Dr. Kenneth W. Kaiser
Technical Supervisor, CSDL

Accepted by _____


Dr. Frederick C. Nelson
Thesis Supervisor, Tufts University

Accepted by _____


Dr. Denis W. Ferment
Tufts University

SIMULATION OF INTERNAL DAMPING IN A ROTATING SYSTEM SUPPORTED BY MAGNETIC BEARINGS

A thesis submitted by

Anthony Michael Cerminaro

In partial fulfillment of the requirements for the degree of

Master of Science in Mechanical Engineering

TUFTS UNIVERSITY

May 1999

© 1999 Anthony M. Cerminaro

Advisors:

Dr. Kenneth W. Kaiser
The Charles Stark Draper Laboratory

Dr. Frederick C. Nelson
Tufts University

Dr. Denis Fermentat
Tufts University

Abstract

A rotor with internal damping is a complex dynamic system. An accurate model is required to design and test controllers for supercritical operation. This thesis developed and validated a model for this purpose.

An existing rotordynamic Finite Element Method (FEM) model and magnetic bearing simulation, developed by Draper Laboratory, were first compared to actual rotor test data. Correlation of predicted and actual parameters such as critical speeds, rigid body modes, and rotor displacements was used to validate the Draper model and simulation. Once this correlation was established, both the model and simulation were modified to include the destabilizing effects of internal damping. Using these improved predictive tools, several Proportional Integral and Derivative (PID) controllers were designed and implemented in an effort to stabilize a rotor system with internal damping. The PID controllers were effective in stabilizing the rotor systems at sub-critical speeds. However, the model developed during this thesis showed that these controllers were unable to counteract the destabilizing effects of internal damping during supercritical operation. This improved rotordynamic model and magnetic bearing simulation is now available to test more complex controller designs in the supercritical regime.

Abstract

A rotor with internal damping is a complex dynamic system. An accurate model is required to design and test controllers for supercritical operation. This thesis developed and validated a model for this purpose.

An existing rotordynamic Finite Element Method (FEM) model and magnetic bearing simulation, developed by Draper Laboratory, were first compared to actual rotor test data. Correlation of predicted and actual parameters such as critical speeds, rigid body modes, and rotor displacements was used to validate the Draper model and simulation. Once this correlation was established, both the model and simulation were modified to include the destabilizing effects of internal damping. Using these improved predictive tools, several Proportional Integral and Derivative (PID) controllers were designed and implemented in an effort to stabilize a rotor system with internal damping. The PID controllers were effective in stabilizing the rotor systems at sub-critical speeds. However, the model developed during this thesis showed that these controllers were unable to counteract the destabilizing effects of internal damping during supercritical operation. This improved rotordynamic model and magnetic bearing simulation is now available to test more complex controller designs in the supercritical regime.

Bibliography of Key Sources

1. Zorzi, E.S., Nelson, H.D., "Finite Element Simulation of Rotor-Bearing Systems with Internal Damping", *Journal of Engineering for Power*, January 1977
2. Nelson, Frederick, Damping in Structural Analysis and Design, *Impact and Friction Solids, Structures, and Machines* Birkhäuser In Press, 1999
3. Gunter, Edgar, J., "Dynamic Stability of Rotor-Bearing Systems", NASA SP-113, 1966
4. Kimball, A.L., *Vibration Prevention in Engineering*, John Wiley & Sons, London, 1932
5. Lund, J.W., "Stability and Damped Critical Speeds of a Flexible Rotor in Fluid Film Bearings", ASME Design Engineering Division, Publication DE v 2 pt. 1, 11th Biennial Conference on Mechanical Vibration and Noise, Rotating Machinery Dynamics, 1987, Boston, MA
6. Ehrich, F.F., "Shaft Whirl Induced by Rotor Internal Damping", *Journal of Applied Mechanics*, June 1964
7. Nelson, H.D., McVaugh, J.M., "The Dynamics of Rotor Bearing Systems: Using Finite Elements", *Journal of Engineering for Industry*, May 1976
8. Nelson, H.D., "A Finite Rotating Shaft Element Using Timoshenko Beam Theory," Engineering Research Center Report ERC-R-77023, Arizona State University, 1977.
9. Antkowiak, B.M., Scholten, J. R., Nelson, F.C., "Rotordynamic Modeling and Control System for an Aircraft Gas Turbine Rotor Suspended on Magnetic Bearings," 1998

SIMULATION OF INTERNAL DAMPING IN A ROTATING SYSTEM SUPPORTED BY MAGNETIC BEARINGS

A thesis submitted by

Anthony Michael Cerminaro

In partial fulfillment of the requirements for the degree of

Master of Science in Mechanical Engineering

TUFTS UNIVERSITY

May 1999

© 1999 Anthony M. Cerminaro

Advisors:

Dr. Kenneth W. Kaiser
The Charles Stark Draper Laboratory

Dr. Frederick C. Nelson
Tufts University

Dr. Denis Fermentat
Tufts University

Abstract

A rotor with internal damping is a complex dynamic system. An accurate model is required to design and test controllers for supercritical operation. This thesis developed and validated a model for this purpose.

An existing rotordynamic Finite Element Method (FEM) model and magnetic bearing simulation, developed by Draper Laboratory, were first compared to actual rotor test data. Correlation of predicted and actual parameters such as critical speeds, rigid body modes, and rotor displacements was used to validate the Draper model and simulation. Once this correlation was established, both the model and simulation were modified to include the destabilizing effects of internal damping. Using these improved predictive tools, several Proportional Integral and Derivative (PID) controllers were designed and implemented in an effort to stabilize a rotor system with internal damping. The PID controllers were effective in stabilizing the rotor systems at sub-critical speeds. However, the model developed during this thesis showed that these controllers were unable to counteract the destabilizing effects of internal damping during supercritical operation. This improved rotordynamic model and magnetic bearing simulation is now available to test more complex controller designs in the supercritical regime.

Abstract

A rotor with internal damping is a complex dynamic system. An accurate model is required to design and test controllers for supercritical operation. This thesis developed and validated a model for this purpose.

An existing rotordynamic Finite Element Method (FEM) model and magnetic bearing simulation, developed by Draper Laboratory, were first compared to actual rotor test data. Correlation of predicted and actual parameters such as critical speeds, rigid body modes, and rotor displacements was used to validate the Draper model and simulation. Once this correlation was established, both the model and simulation were modified to include the destabilizing effects of internal damping. Using these improved predictive tools, several Proportional Integral and Derivative (PID) controllers were designed and implemented in an effort to stabilize a rotor system with internal damping. The PID controllers were effective in stabilizing the rotor systems at sub-critical speeds. However, the model developed during this thesis showed that these controllers were unable to counteract the destabilizing effects of internal damping during supercritical operation. This improved rotordynamic model and magnetic bearing simulation is now available to test more complex controller designs in the supercritical regime.

Bibliography of Key Sources

1. Zorzi, E.S., Nelson, H.D., "Finite Element Simulation of Rotor-Bearing Systems with Internal Damping", *Journal of Engineering for Power*, January 1977
2. Nelson, Frederick, Damping in Structural Analysis and Design, *Impact and Friction Solids, Structures, and Machines* Birkhäuser In Press, 1999
3. Gunter, Edgar, J., "Dynamic Stability of Rotor-Bearing Systems", NASA SP-113, 1966
4. Kimball, A.L., *Vibration Prevention in Engineering*, John Wiley & Sons, London, 1932
5. Lund, J.W., "Stability and Damped Critical Speeds of a Flexible Rotor in Fluid Film Bearings", ASME Design Engineering Division, Publication DE v 2 pt. 1, 11th Biennial Conference on Mechanical Vibration and Noise, Rotating Machinery Dynamics, 1987, Boston, MA
6. Ehrich, F.F., "Shaft Whirl Induced by Rotor Internal Damping", *Journal of Applied Mechanics*, June 1964
7. Nelson, H.D., McVaugh, J.M., "The Dynamics of Rotor Bearing Systems: Using Finite Elements", *Journal of Engineering for Industry*, May 1976
8. Nelson, H.D., "A Finite Rotating Shaft Element Using Timoshenko Beam Theory," Engineering Research Center Report ERC-R-77023, Arizona State University, 1977.
9. Antkowiak, B.M., Scholten, J. R., Nelson, F.C., "Rotordynamic Modeling and Control System for an Aircraft Gas Turbine Rotor Suspended on Magnetic Bearings," 1998

SIMULATION OF INTERNAL DAMPING IN A ROTATING SYSTEM SUPPORTED BY MAGNETIC BEARINGS

A thesis submitted by

Anthony Michael Cerminaro

In partial fulfillment of the requirements for the degree of

Master of Science in Mechanical Engineering

TUFTS UNIVERSITY

May 1999

© 1999 Anthony M. Cerminaro

Advisors:

Dr. Kenneth W. Kaiser
The Charles Stark Draper Laboratory

Dr. Frederick C. Nelson
Tufts University

Dr. Denis Fermentat
Tufts University

Abstract

A rotor with internal damping is a complex dynamic system. An accurate model is required to design and test controllers for supercritical operation. This thesis developed and validated a model for this purpose.

An existing rotordynamic Finite Element Method (FEM) model and magnetic bearing simulation, developed by Draper Laboratory, were first compared to actual rotor test data. Correlation of predicted and actual parameters such as critical speeds, rigid body modes, and rotor displacements was used to validate the Draper model and simulation. Once this correlation was established, both the model and simulation were modified to include the destabilizing effects of internal damping. Using these improved predictive tools, several Proportional Integral and Derivative (PID) controllers were designed and implemented in an effort to stabilize a rotor system with internal damping. The PID controllers were effective in stabilizing the rotor systems at sub-critical speeds. However, the model developed during this thesis showed that these controllers were unable to counteract the destabilizing effects of internal damping during supercritical operation. This improved rotordynamic model and magnetic bearing simulation is now available to test more complex controller designs in the supercritical regime.

Acknowledgments

There are a number of people who have made this thesis possible. These last two years would have been much harder without them.

First and foremost, I want to thank Dr. Kenneth Kaiser for bringing me on board the Draper team and for allowing me to choose the topic that I was most interested in. Whenever I had a problem or was slight fuzzy about a concept, Dr. Kaiser always had the time to explain it to me. What really helped me the most in this area was his tremendous knowledge on every single topic.

Next, I would like to extend my appreciation to Dr. Frederick Nelson, my Tufts advisor. He originally suggested this topic and helped me clarify my goals and theoretical methods. Dr. Nelson constantly reviewed and objectively critiqued my work, thus allowing me to work quickly and make efficient use of my time. His patience and clear way of presenting complex concepts, such as internal damping, was invaluable in this study.

Mr. Bernie Antkowiak and Mr. Jim Scholten both played an active role in the development of this thesis. Mr. Antkowiak, who wrote the original Draper Rotor Finite Element Program, always had a "few free minutes" for helping me out in those tough spots: especially when the hardware and the software just weren't making any sense. Mr. Scholten, who wrote the original Draper Laboratory Magnetic Bearing Simulation, gave me a clear understanding of the simulations and controller development techniques; not to mention helping me make the rotor test rig work when it wasn't behaving.

I also would like to thank Dr. Denis Fermental, Tufts University, for reviewing my results from the magnetic bearings simulations. His suggestions were very helpful in making my figures and text consistent with the accepted industry standards.

Sincere appreciation is extended to the United States Air Force, Draper Laboratory, and Tufts University for giving me this opportunity to perform this research.

Finally, I would like to thank Amy, not only for all her love and patience during this thesis, but also for following me around all these years from California, to Massachusetts, and now to Ohio.


This thesis was prepared at The Charles Stark Draper Laboratory, Inc., under Internal Research and Development Project number 18613. Publication of this thesis does not constitute approval by Draper or the sponsoring agency of the findings or conclusions contained herein. It is published for the exchange and stimulation of ideas. Permission is granted by the author to Tufts University to reproduce any or all of this thesis.


Anthony Michael Cerminaro

Assignment

Draper Laboratory Report Number T-1335

In consideration for the research opportunity and permission to prepare my thesis by and at The Charles Stark Draper Laboratory, Inc., I hereby assign my copyright of the thesis to The Charles Stark Draper Laboratory, Inc., Cambridge, Massachusetts.



Anthony Michael Cerminaro

14 APR 99

(date)

Table Of Contents

Abstract.....	ii
Acknowledgments.....	iii
Assignment.....	iv
List of Figures.....	vi
List of Tables.....	viii
Nomenclature.....	ix
Chapter 1 Introduction.....	1-1
1.1 Background.....	1-1
1.2 Thesis Motivation.....	1-2
1.3 Thesis Outline.....	1-3
Chapter 2 Damping.....	2-1
2.1 External Damping (Viscous Model).....	2-1
2.2 The Linear Viscoelastic Model.....	2-4
2.3 The Internal Viscous Damping Model.....	2-8
2.4 The Internal Hysteretic Damping Model.....	2-10
2.5 Internal Viscous Damping vs. Internal Hysteretic Damping.....	2-15
Chapter 3 Internal Damping in Rotors.	3-1
3.1 Rotordynamic Basics.....	3-1
3.2 Internal Viscous Damping.....	3-5
3.3 Internal Hysteretic Damping	3-10
3.4 The Effect of External Damping on the Instability Threshold.....	3-13
Chapter 4 Finite Element Model of Rotor.....	4-1
4.1 Finite Element Method - A Timoshenko Rotor Element.....	4-1
4.2 Addition of Internal Damping.....	4-3
4.3 Validation of FEM Model.....	4-6
Chapter 5 Magnetic Bearing Simulation Design.....	5-1
5.1 State-Space Model of Rotor - No Internal Damping.....	5-1
5.2 State-Space Model of Rotor - Internal Damping Included.....	5-5
5.3 Magnetic Bearing Simulation Description.....	5-8
5.4 Controller Design.....	5-10
Chapter 6 Modeling and Simulation Predictions and Comparison to Actual Rotor Data-No Internal Damping.....	6-1
6.1 FEM Modeling.....	6-1
6.2 Magnetic Bearing Simulation Results.....	6-8
6.3 Actual Rotor Testing and Comparison to Simulation.....	6-13
Chapter 7 Modeling and Simulation Predictions for a Rotor with Internal Damping.....	7-1
7.1 FEM Modeling.....	7-1
7.2 Magnetic Bearing Simulation Predictions (Internal Damping Included).....	7-9
Chapter 8 Summary and Conclusions.....	8-1
References.....	8-6
Appendix A - Detailed Information on Draper Magnetic Bearing Test Apparatus.....	A-1
Appendix B - A Timoshenko Rotor Element.....	B-1
Appendix C - Input Files for Draper Rotor FEM Program.....	C-1

List of Figures

Figure 1: Newtonian Viscous Damping Model.....	2-3
Figure 2: Stress and Strain Phasor Diagram.....	2-5
Figure 3: Stress-Strain, Energy Dissipation Ellipse for Viscoelastic Material.....	2-6
Figure 4: Linear Model of Viscoelastic Material.....	2-7
Figure 5: Linear Internal Viscous Damping Model.....	2-8
Figure 6: Kimball/Newkirk Testing Apparatus.....	2-11
Figure 7: Stress and Strain Phasor Diagram (Modified).....	2-12
Figure 8: Linear Internal Hysteretic Damping Model.....	2-13
Figure 9: Variation of Energy Dissipated per Cycle with Frequency, [5]	2-17
Figure 11: Jeffcott Rotor.....	3-1
Figure 12: Jeffcott Rotor, Model for Natural Vibration.....	3-2
Figure 13: Jeffcott Rotor, Non-Centered Disc.....	3-3
Figure 14: Campbell Diagram for Jeffcott Rotor.....	3-3
Figure 15: Rotating, Whirling Beam Cross Section, Ehrich, [13].....	3-6
Figure 16: Rotating, Whirling Beam Cross Section Showing Direction of Internal Damping Force, No External Damping.....	3-7
Figure 17: Rotating, Whirling Beam Cross Section Showing Directions of Internal and External Damping Forces.....	3-8
Figure 18: Campbell Diagram for Rotor with Internal and External Viscous Damping.....	3-9
Figure 19: Rotor Configuration for Displacements, Lund.....	3-11
Figure 20: Rotor Configuration for Bending and Shear Forces, Lund.....	3-12
Figure 21: Stability Thresholds for Viscous Internal and Viscous External Damping.....	3-14
Figure 22: Amount of Viscous External Damping Required for Stability with Internal Hysteretic Damping.....	3-15
Figure 23: Log Decrement versus Spin Speed for System with Internal Hysteretic Damping and a Family of Constant External Viscous Damping Curves.....	3-16
Figure 24: Log Decrement versus Spin Speed for System with Internal Hysteretic Damping and a Family of Constant External Hysteretic Damping Curves.....	3-17
Figure 25: Rotor System Configuration, Nelson.....	4-2
Figure 26: Campbell Diagram for Rotor with Internal and External Damping.....	4-6
Figure 27: Draper FEM Model Compared to Nelson Solution, Undamped Rotor Supported by Identical Bearings, Modes 1 and 2.....	4-7
Figure 28: Draper FEM Model Compared to Nelson Solution, Undamped Rotor Supported by Identical Bearings, Modes 1 and 2 (Detailed View) ..	4-8
Figure 29: Log Decrements, Rotor with Viscous Internal Damping, No External Damping, Modes 1 and 2.....	4-8
Figure 30: Log Decrements, Rotor with Viscous Internal Damping, and Viscous External Damping.....	4-9
Figure 31: Log Decrements, Rotor with Hysteretic Internal Damping, No External Damping, Modes 1 and 2.....	4-10

Figure 32: Log Decrements, Rotor with Hysteretic Internal Damping and Viscous External Damping.....	4-10
Figure 33: Simplified Block Diagram of Magnetic Bearing Simulation, (Scholten)	5-9
Figure 34: FEM Model of Entire Rotor.....	6-1
Figure 35: FEM Model of Rotor Actuator.....	6-3
Figure 36: Campbell Diagram for Rotor, Bearing Stiffness = 50 lbs/in, Bearing Damping = 1.5×10^{-2} lbs-sec/in.....	6-4
Figure 37: Bode Plot of Free-Free Rotor Model.....	6-5
Figure 38: Root Loci of Free-Free Rotor Model as Rotation Speed Increases (No Internal or External Damping).....	6-7
Figure 39: Simulation Prediction of Rotor Response during a 0 – 325 Hz Ramp.....	6-9
Figure 40: (A) Plant Response, (B) Controller Response, (C) Plant and Controller Combined (Open-Loop) Response for a Rotor Spin Speed of 150 Hz.....	6-10
Figure 41: Open Loop Gain vs. Phase at 150 Hz.....	6-11
Figure 42: Open and Closed Loop Frequency Response, 150 Hz.....	6-12
Figure 43: PSD of Simulation at Constant Rotor Spin Speed of 148 Hz	6-13
Figure 44: Predicted and Actual Rotor Displacements, 102 Hz.....	6-14
Figure 45: Predicted and Actual Rotor Displacements, 148 Hz.....	6-15
Figure 46: Predicted and Actual Rotor Displacements, 52 Hz.....	6-15
Figure 47: PSD of Actual Rotor at Constant Rotor Spin Speed of 148 Hz.....	6-16
Figure 48: Bode Plot of Free-Free Rotor Model at 250 Hz with Internal Viscous Damping $\eta_v = 2 \times 10^{-6}$	7-2
Figure 49: Bode Plot of Free-Free Rotor Model at 250 Hz with Internal Hysteretic Damping $\eta_H = 2 \times 10^{-4}$	7-3
Figure 50: Bode Plot of Free-Free Rotor Model at 250 Hz with Internal Viscous Damping $\eta_v = 2 \times 10^{-6}$, Internal Hysteretic Damping $\eta_H = 2 \times 10^{-4}$	7-3
Figure 51: Root Loci of Free-Free Rotor Model as Rotation Speed Increases (Internal Viscous Damping $\eta_v = 2 \times 10^{-6}$).....	7-5
Figure 52: Root Loci of Free-Free Rotor Model as Rotation Speed Increases (Internal Hysteretic Damping $\eta_H = 2 \times 10^{-4}$).....	7-6
Figure 53: Root Loci of Free-Free Rotor Model as Rotation Speed Increases (Internal Viscous Damping $\eta_v = 2 \times 10^{-6}$, Internal Hysteretic Damping $\eta_H = 2 \times 10^{-4}$).....	7-8
Figure 54: Simulation Prediction of Rotor Response during a 0 – 400 Hz Ramp, Internal Viscous Damping $\eta_v = 2 \times 10^{-6}$	7-9
Figure 55: (A) Plant Response, (B) Controller Response, (C) Plant and Controller Combined (Open-Loop) Response for a Rotor Spin Speed of 250 Hz, Internal Viscous Damping $\eta_v = 2 \times 10^{-6}$	7-10
Figure 56: Open Loop Gain vs. Phase at 250 Hz, Internal Viscous Damping $\eta_v = 2 \times 10^{-6}$	7-11
Figure 57: Open and Closed Loop Frequency Response at 250 Hz, Internal Viscous Damping $\eta_v = 2 \times 10^{-6}$	7-12
Figure 58: Simulation Prediction of Rotor Response during a 0 – 400 Hz Ramp, Internal Hysteretic Damping $\eta_H = 2 \times 10^{-4}$	7-13

Figure 59: (A) Plant Response, (B) Controller Response, (C) Plant and Controller Combined (Open-Loop) Response for a Rotor Spin Speed of 250 Hz, Internal Hysteretic Damping $\eta_H = 2 \times 10^{-4}$...	7-13
Figure 60: Open Loop Gain vs. Phase at 250 Hz, Internal Hysteretic Damping $\eta_H = 2 \times 10^{-4}$	7-14
Figure 61: Open and Closed Loop Frequency Response at 250 Hz, Internal Hysteretic Damping $\eta_H = 2 \times 10^{-4}$	7-15
Figure 62: Simulation Prediction of Rotor Response during a 0 – 400 Hz Ramp, Internal Viscous Damping $\eta_V = 2 \times 10^{-6}$, Internal Hysteretic Damping $\eta_H = 2 \times 10^{-4}$	7-16
Figure 63: (A) Plant Response, (B) Controller Response, (C) Plant and Controller Combined (Open-Loop) Response for a Rotor Spin Speed of 250 Hz, Internal Hysteretic Damping $\eta_H = 2 \times 10^{-4}$, Internal Viscous Damping $\eta_V = 2 \times 10^{-6}$	7-17
Figure 64: Open Loop Gain vs. Phase at 250 Hz, Internal Hysteretic Damping $\eta_H = 2 \times 10^{-4}$, Internal Viscous Damping $\eta_V = 2 \times 10^{-6}$	7-18
Figure 65: Open and Closed Loop Frequency Response Internal Hysteretic Damping $\eta_H = 2 \times 10^{-4}$, Internal Viscous Damping $\eta_V = 2 \times 10^{-6}$	7-18

List of Tables

Table 1: Forced Excitation of a Single Degree of Freedom System with Viscous or Hysteretic Damping, [5].....	2-17
Table 2: Calculations of Added Mass and Inertia Due to Actuator Rotor.....	6-3
Table 3: Rotor Free-Free Natural Frequencies for $\Omega = 0$	6-4
Table 4: Rotor Whirl Frequency Pairs, Bearing Stiffness = 50 lbs/in, Bearing Damping = 1.5×10^{-2} lbs-sec/in.....	6-5
Table 5: Comparison of Original FEM Model to Original Simulation, FEM Model: Bearing Stiffness = 50 lbs/in, Bearing Damping = 1.5×10^{-2} lbs-sec/in, Simulation: $K_P = 0.05$ lb/mil, $K_I = 3.00$ lb/mil-s, $K_D = 0.002$ lb-sec/mil, Derivative Bandwidth = 1000 Hz.....	6-13
Table 6: Comparison of Original FEM, Modified Simulation and Actual Rotor Rig Data, FEM Model: Bearing Stiffness = 50 lbs/in, Bearing Damping = 1.5×10^{-2} lbs-sec/in Simulation: $K_P = 0.05$ lb/mil, $K_I = 3.00$ lb/mil-s, $K_D = 0.002$ lb-sec/mil, Derivative Bandwidth = 1000 Hz.....	6-17
Table 7: FEM Predicted Rotor Instability Thresholds, Bearing Stiffness = 50 lbs/in, Bearing Damping = 1.5×10^{-2} lbs-sec/in.....	7-2
Table 8: Comparison of Instability Threshold Predictions FEM Model: Bearing Stiffness = 50 lbs/in, Bearing Damping = 1.5×10^{-2} lbs-sec/in, Simulation: $K_P = 0.05$ lb/mil, $K_I = 3.00$ lb/mil-s, $K_D = 0.002$ lb-sec/mil, Derivative Bandwidth = 1000 Hz	7-20

Nomenclature

A	- Cross sectional area of dashpot damper
[A]	- State space dynamic matrix
[B]	- State space actuator matrix
C_1, C_2	- Amplitudes of single degree of freedom solution
c	- Viscous damping constant
c_c	- Critical damping constant
c_e	- External viscous damping constant
c_i	- Internal viscous damping constant
[Cd]	- External damping matrix, $[Cd] = 2[\zeta\omega]$
[C]	- State space sensor matrix
[C _e]	- External damping matrix
D	- Energy dissipated per cycle
E	- Modulus of Elasticity
E'	- Loss Modulus
{f}	- Fixed frame external forces
F	- Forcing function amplitude
\bar{F}, \bar{x}	- Force, displacement (structural)
[G]	- Gyroscopic matrix
[\underline{G}]	- Normalized gyroscopic matrix
[\hat{G}]	- Normalized gyroscopic, external damping matrix (internal damping only)
G	- Shear Modulus
h	- Height of dashpot damper
i	- Complex quantity $\sqrt{-1}$
I	- Moment of Inertia
I_d	- Diametral Moment of Inertia
I_p	- Polar Moment of Inertia
Im []	- Imaginary part of []
[I]	- Identity matrix, diagonal
k	- Stiffness
k_{ij}	- Elements in stiffness matrix [K]
[K]	- Total stiffness matrix (includes bending and shear deformations)
[K _{bend}]	- Bending stiffness matrix
[K _{cir}]	- Circulation stiffness matrix
[K _{shear}]	- Shear stiffness matrix
K_D	- Derivative Constant for PID Controller
K_I	- Integral Constant for PID Controller
K_P	- Proportional Constant for PID Controller
[L]	- $\hat{n} \times \hat{m}$ matrix that inflates the force matrix, {f}, from an $\hat{m} \times 1$ to an $\hat{n} \times 1$ matrix
l	- Element length
m	- Mass
\hat{m}	- Number of forces applied to the rotor
M	- Moment

$[M]$ - Mass matrix
 $[M_{\text{trans}}]$ - Translational mass matrix
 $[M_{\text{rot}}]$ - Rotational mass matrix
 M', V' - Moment and shears on the right side of the stations in the Myklestad-Prohl method
 \hat{n} - Number of modes in modal matrix
 P_n - Elements of the modal matrix (undamped eigenvectors)
 p_1, p_2 - Exponential part of single degree of freedom solution
 $\{q\}$ - Fixed frame physical coordinates
 r - Radial location of element on shaft, internal viscous damping
 r_o - Radius of shaft, viscous internal damping
 R - Radius of whirl, internal viscous damping
 $\text{Re}[]$ - Real part of $[]$
 S_j - Complex eigenvalue solution
 t - Time
 T - Kinetic energy
 u - Velocity in dashpot damper
 V - Potential energy
 v - Velocity in dashpot damper
 V - Centerline displacement in y direction
 V'', W'' - Second derivatives of displacements
 V_{shear} - Contribution to displacement due to shear
 V_{bend} - Contribution to displacement due to bending
 $\langle W \rangle$ - Time average power dissipated
 W - Centerline displacement in x direction
 x - Displacement
 \hat{x} - Amplitude of phasor
 x, \dot{x}, \ddot{x} - Displacement, velocity, acceleration
 y - Distance from center to edge of dashpot damper
 y_o - Shaft deflection, internal viscous damping
 Z_m - Mechanical impedance

$\{\alpha\}$	- State space coordinates
β	- Rotation about y-axis (Jeffcott Rotor) or Rotation around x axis (Nelson)
δ	- Logarithmic decrement or Rotation about x-axis, Jeffcott Rotor
ϵ	- Strain
ϵ_o	- Strain at edge of shaft, internal viscous damping
$\hat{\epsilon}$	- Logarithmic decrement for the internal hysteretic damping of the shaft divided by π
ϕ	- Angular shaft displacement around x-axis (hysteretic)
η	- Loss factor
$[\eta]$	- Internal damping matrix
η_{eff}	- Effective loss factor
$\eta_{\text{H-struct}}$	- Structural hysteretic loss factor
η_{H}	- Internal hysteretic damping coefficient
η_{V}	- Internal viscous damping coefficient
φ	- Phase angle
$[\Phi]$	- Modal matrix
$[\underline{\Phi}]$	- Normalized modal matrix
$[\bar{\Phi}]$	- Shear deformation
Γ	- Rotation around y-axis
κ	- cross sectional shape factor for shear deformation of a shaft
Λ	- Translational shape functions for Timoshenko rotor element
λ	- Whirl orbit grow/decay
μ	- Viscosity
μ_i	- Viscosity, internal damping
μ_e	- Viscosity, external damping
θ	- Angle between shaft whirl and shaft rotation, internal viscous damping
θ	- Angular shaft displacement around y-axis (hysteretic)
Θ	- Rotational shape functions for Timoshenko rotor element
ρ	- Density
σ	- Stress
$\underline{\sigma}$	- Stress (complex quantity)
$\tilde{\sigma}$	- Stress under sinusoidal motion
τ	- Shear stress
ω	- Whirl speed
ω_d	- Frequency of damped vibration
ω_n	- Natural frequency
$[\omega^2]$	- Diagonal matrix, squared eigenvalues
Ω	- Rotor spin speed
Ω_{cr}	- Critical Speed
Ω_{th}	- Instability Threshold
$\{\xi\}$	- Modal coordinates
ζ	- Damping ratio

Chapter 1 Introduction

1.1 Background

The rotors in many commercial and military rotating machines operate above the first, second and even third critical speeds, [1]. Substantial weight and performance advantages are afforded to those machines that can run at these high speeds, [2]. But as the speed increases, eventually the rotor will become unstable.

A primary destabilizing mechanism for these high-speed rotors is the presence of internal damping. This type of damping, due to strain of the shaft material or to micro-movements at shrink fits and/or couplings, can under certain circumstances, feed energy into the shaft vibration and thereby induce instability, [2].

Recently, magnetic bearings have emerged as a possible solution to the destabilizing effects of internal damping. The basic advantage of magnetic bearings over standard bearings is that the stiffness and damping of the magnetic bearings can be varied as a function of spin speed or other conditions of the rotating system. This advantage has already been exploited by the development of closed loop controllers that increase the damping of the magnetic bearings as the rotor passes through a critical speed, and then decrease the damping after critical speed passage.

Furthermore, as the spin speed approaches an instability threshold, it should be possible to develop a controller to increase the external damping of the magnetic bearings (or make other modifications) to counteract the destabilizing effects of the rotor's internal damping. This increased external damping (or other factors) should be able to delay the

onset of instability and allow the rotor to be run at even higher speeds. This thesis will clarify the concepts of internal damping; validate an existing FEM rotor model and magnetic bearing simulation by comparing predictions to actual rotor test data; incorporate internal damping into the rotor model and simulation; and it will test a basic PID controller to determine if it is sufficient to counteract the effect of internal damping.

1.2 Thesis Motivation

In line with its work on Robust Control Schemes for Magnetic Bearings, The Charles Stark Draper Laboratory has developed a rotordynamic finite element model (Antkowiak) that can successfully predict critical speeds. In addition, the program also produces a state space model of the rotordynamic system for use in a magnetic bearing simulation (Scholten). Although the model and simulation were highly detailed, they did not incorporate any destabilizing effects. By adding internal damping to this FEM model, the instability threshold of the system can be predicted, yielding a more accurate state space model for supercritical operation. In addition, this model could now be placed in a magnetic bearing simulation so that different controllers could be designed and tested to achieve improved control and possibly increase the instability threshold, thus allowing the rotor to run at higher speeds.

In addition to the control-based goals mentioned above, the implementation of state-of-the-art technology into current Draper Laboratory projects is an equally important goal of this thesis. The most appropriate project for the magnetic bearing and control technology is the Draper Laboratory Flywheel Energy Storage effort. This

Internal Research and Development project is devoted to demonstrating the first flywheel energy storage system capable for use in space. This thesis is aimed at contributing a high fidelity model and improved simulation to assist in the testing of various controller schemes that could allow the flywheel to operate at higher speeds; thus allowing the storage of more energy. The ability to predict unstable rotordynamic behavior and give a certain, limited amount of control to counteract these effects can also benefit many other ongoing and future projects in the Laboratory.

1.3 Thesis Outline

This chapter briefly discusses some of the challenges in the field of rotordynamics and introduces the possibility of using magnetic bearings to compensate for the destabilizing effects of internal damping. The motivations for the thesis are then described and the goals are presented. A brief overview of subsequent chapters follows.

Chapter Two discusses the concepts of external and internal damping. First, external damping is described, including the external viscous damping model. Internal damping is then defined and further divided into two distinct types: internal viscous and internal hysteretic damping. The models for each case are presented in detail.

Chapter Three takes the concept of internal damping and applies it to rotating systems. Again the distinction between internal viscous and internal hysteretic damping is made. An emphasis is placed on the role of internal damping in determining the instability thresholds. Next, the specific effect of external damping on the instability threshold is addressed.

Chapter Four introduces the finite element method as a means to analyze complex rotordynamic systems. The internal damping models are defined, and the element matrices and the equations of motion are referenced and summarized. The model is then validated using a standard test case from the references.

Chapter Five discusses the development of a detailed state space model (Antkowiak) and a high fidelity simulation (Scholten) that includes internal damping. First the method that the FEM program used to produce the state space model is outlined, then the full simulation configuration is presented. Finally, some details are given on the specific PID controller that was used in the simulation.

Chapter Six presents the original FEM modeling and simulation predictions, for a rotor without internal damping, and compares them to actual rotor test data. First, the rotor FEM model is described for an actual rotor located at Draper Laboratory. Next, the model predictions for the rigid body modes and critical speeds are given. Using the state space model generated by the FEM program, the simulation predictions for the rigid body modes, critical speeds, and rotor displacements are presented. Finally, the FEM and simulation predictions are compared to actual rotor test results.

Chapter Seven presents the modeling and simulation predictions for a rotor with various combinations of internal damping. First, instability threshold predictions from the FEM program are presented. Then, the full simulation results are given, and the effectiveness of the PID controller is discussed.

The thesis is summarized and conclusions are drawn in Chapter Eight. Recommendations are made for future work at Draper Laboratory and also for the fields of rotordynamics and controls in general, using magnetic bearing technology.

Chapter 2 Damping

When a shaft spins, it experiences a jump rope like motion called whirl or precession, due to slight shaft imbalance or other external forces. This whirling motion can put the shaft into alternating states of stress/strain. Since the shaft material is not perfectly elastic, work is performed on the system with every rotation. This additional energy added to the whirling rotor system is due to the internal damping of the shaft. As the speed and work done on the shaft increases, the whirl orbit of the shaft begins to grow. At lower speeds, the bearings of the rotating system are able to dissipate this energy/work by transmitting it to the ground/surroundings (external damping). However, as the rotation speed, energy, and shaft amplitude/orbit increase, the bearings will not be able to dissipate all of the energy and the shaft will become unstable.

There are two common models of internal damping: viscous and hysteretic. Viscous internal damping is defined as a velocity dependent quantity that is represented as a dashpot with coefficient η_v . This type of internal damping tends to destabilize the system only after the first critical speed. Hysteretic internal damping is defined as a displacement dependent quantity expressed by the loss factor η_H . This type of damping can be destabilizing at any speed (except for zero speed).

2.1 External Damping (Viscous Model)

Prior to elaborating on internal damping, the more familiar “external damping”, or damping to ground, will be briefly discussed. If a system with only mass and elasticity,

completely isolated from its surroundings, is disturbed by a perturbation, it will begin to vibrate. Since the system is not connected to its surroundings, no energy can be transferred away from the system and it will continue to vibrate forever. Since this situation never occurs in nature, an energy transfer mechanism must exist between the system and its surroundings, [3]. In many systems, this transfer mechanism gradually converts vibrational energy to heat or sound. This is known as damping or *external damping*, since the energy is taken from the vibrating system and transferred to the “external” surroundings, [4].

The most widely used model for external damping is the linear viscous model. This model assumes that energy is removed from a system in the same manner as energy is removed by the use of a dashpot. A dashpot is a piston-cylinder type device filled with viscous oil or other fluid. As the piston is moved down into the fluid (by a force, with an associated energy) the fluid passes by the piston in a thin fluid layer (see Figure 1). According to Newton’s Laws of viscous flow, the shear stress developed in the fluid layer between the piston and the wall of the cylinder is given by

$$\tau = -\mu \frac{du}{dy} = \frac{v}{h} \quad (1)$$

The shear resisting force developed along the piston is

$$F = -\tau A = -\frac{\mu A}{h} v = -cv \quad (2)$$

where $\frac{\mu A}{h}$ is defined as the viscous damping constant “c”. Therefore, the Newtonian viscous damping model predicts a linear relationship between the damping force and the velocity. More specifically, the damper exerts a force that is proportional to and in anti-phase with the velocity, [4].

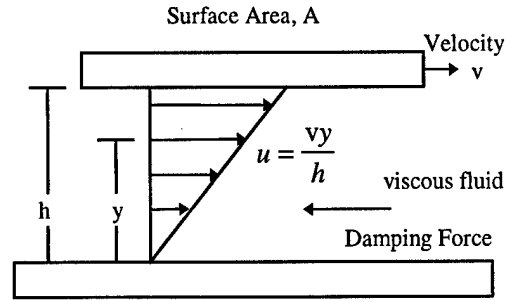


Figure 1: Newtonian Viscous Damping Model

In a single degree of freedom system, the viscous external damping is represented by the $c\dot{x}$ term in the standard equation of motion of

$$m\ddot{x} + c\dot{x} + kx = F \cos \Omega t \quad (3)$$

By assuming the solution to be of the form $x = e^{pt}$, the homogeneous equation (with right-hand side equal to zero) can be solved to give:

$$x(t) = C_1 e^{p_1 t} + C_2 e^{p_2 t}, \quad (4)$$

where

$$p_{1,2} = -\frac{c}{2m} \pm \sqrt{\left(\frac{c}{2m}\right)^2 - \frac{k}{m}} \quad (5)$$

and where the natural frequency of the system is given by

$$\omega_n = \sqrt{\frac{k}{m}}. \quad (6)$$

The critical damping, c_c , is defined as the value of the damping constant for which the terms under the radical in equation (5) become zero. Further, the damping ratio is defined as

$$\zeta = \frac{c}{c_c} \quad (7)$$

and the frequency of damped vibration is given by

$$\omega_d = \omega_n \sqrt{1 - \zeta^2} \quad (8)$$

Using all of these definitions, the homogenous solution or transient solution to equation (3) takes the form of:

$$x = C_1 e^{(-\zeta + \sqrt{\zeta^2 - 1})\omega_n t} + C_2 e^{(-\zeta - \sqrt{\zeta^2 - 1})\omega_n t} \quad (9)$$

If the damping ratio is less than one, underdamped oscillation occurs. This is characterized by oscillatory motion and by the amplitude of vibration decreasing exponentially with time. If the damping ratio is equal to one, the system is critically damped. In this case, the response of the system will be aperiodic and will quickly diminish to zero without oscillation. Finally, if the damping ratio is greater than one, the system is overdamped and the amplitude will also diminish to zero without oscillation (although not quite as fast as the critically damped case), [4].

2.2 The Linear Viscoelastic Model

Viscoelastic materials are materials which exhibit both elastic and viscous behavior, [13]. A true representative of a viscoelastic material is a polymer. In this type of material, the atoms are joined strongly together, although the long chains can be branched or physically entangled (providing either a weak or strong link). While under a cyclic load, the elastic nature of the polymer arises from the stretching of the intermolecular bonds or entangled chains. In addition, the breaking and reforming of the intermolecular bonds contributes to the viscous nature, or damping, of the material, [5].

When dealing with forced (steady state) sinusoidal motions, it is convenient to represent the stress and strain by rotating vectors in the complex plane. Typically, these

vectors are called phasors. For the case of a material under a sinusoidal motion of frequency Ω , the stress can be given as

$$\tilde{\sigma} = \underline{\sigma} e^{i\Omega t}, \quad (10)$$

where $\underline{\sigma}$ represents a complex quantity. Similarly, the strain of the material under the motion is given by

$$\tilde{\varepsilon} = \underline{\varepsilon} e^{i\Omega t} \quad (11)$$

The physical stress and strain can be found by taking the real part of the respective phasors:

$$\sigma(t) = \text{Re}[\tilde{\sigma}] \text{ and } \varepsilon(t) = \text{Re}[\tilde{\varepsilon}]. \quad (12)$$

To show the relationship between the stress and the strain of a material under sinusoidal load, the two phasors are drawn on the complex plane (Figure 2). From observation, it is has been found that the strain lags the stress by the phase angle φ , [6].

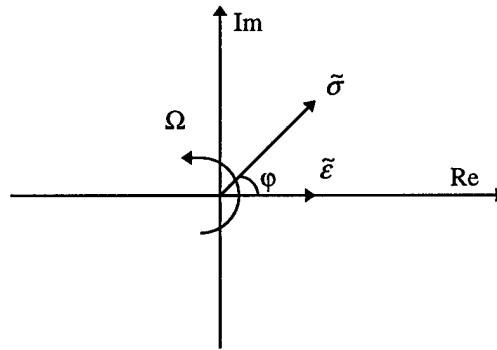


Figure 2: Stress and Strain Phasor Diagram

Plotting this relationship on the real stress-strain axes produces the classic hysteresis ellipse (Figure 3). The dashed line represents a system with no losses, or the constitutive relationship by Hooke of $\sigma = E\varepsilon$. As the losses of the system increase, the

size of the ellipse also begins to increase. Based on the definitions of work and energy, the enclosed area of the ellipse is the energy dissipated per unit volume per cycle of oscillation, [6, 7].

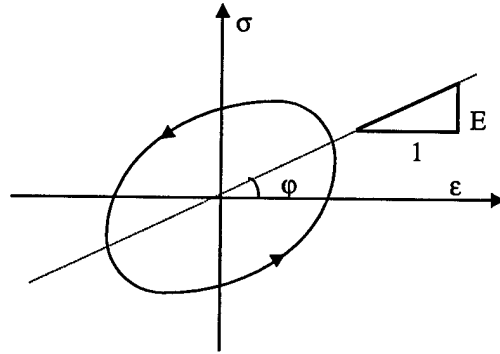


Figure 3: Stress-Strain, Energy Dissipation Ellipse for Viscoelastic Material

The behaviors in Figures 2 and 3 can be summarized in the equation:

$$\underline{\sigma} = \underline{E}\underline{\epsilon} \quad (13)$$

where \underline{E} represents a complex modulus of the form:

$$\underline{E} = E + iE' . \quad (14)$$

The imaginary part E' represents the loss modulus due to the material and is given by

$$E' = E \tan \varphi . \quad (15)$$

where E is the traditional Modulus of Elasticity.

Note that this definition of the total complex modulus and the loss modulus are consistent with Figures 2 and 3.

Substituting the complex modulus into Hooke's constitutive relationship and factoring out E gives:

$$\underline{\sigma} = E(1 + i \frac{E'}{E})\underline{\epsilon} . \quad (16)$$

Now, defining the loss factor η as

$$\eta = \frac{E'}{E} = \tan \varphi, \quad (17)$$

gives the constitutive law of a one-dimensional, linear viscoelastic material:

$$\underline{\sigma} = E(1 + i\eta)\underline{\varepsilon} \quad (18)$$

This is represented by the model in Figure 4, [11, 13, 17].

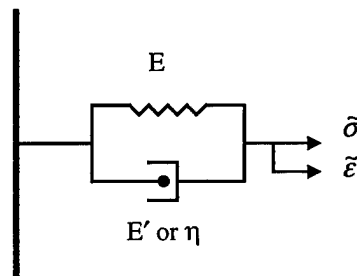


Figure 4: Linear Model of Viscoelastic Material

It is important to note that this linear model is the basis for both types of internal damping. The difference between viscous internal damping and hysteretic internal damping lies in how the loss factor term is defined. Although it is well known that linear models of all types have limitations (the specific limitations of linear internal damping were demonstrated by Graham, [8]), the overriding benefits of a linear stability evaluation have been recognized as a meaningful indication of the effects of internal damping on a rotor system, [2].

2.3 The Internal Viscous Damping Model

One of the simplest mathematical models for describing internal viscous damping is the Voigt Model. It takes the linear viscoelastic model (shown in Figure 4) and designates the damping mechanism as an idealized dashpot with a viscosity of μ_i . Figure 5 shows this standard model for viscous internal damping, [7].

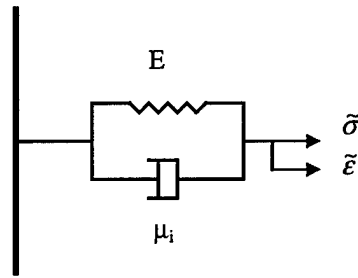


Figure 5: Linear Internal Viscous Damping Model

The constitutive equation for this model is given by:

$$\tilde{\sigma} = E\tilde{\epsilon} + \mu_i \frac{d\tilde{\epsilon}}{dt}, \quad (19)$$

$$\text{or} \quad \underline{\sigma} e^{i\Omega t} = E \underline{\epsilon} e^{i\Omega t} + \mu_i \frac{d(\underline{\epsilon} e^{i\Omega t})}{dt}. \quad (20)$$

If the strain derivative is evaluated and the common exponential term is eliminated, the equation reduces to:

$$\underline{\sigma} = (E + i\Omega\mu_i) \underline{\epsilon}. \quad (21)$$

Now comparing the $\Omega\mu_i$ term to the η term in equation (18) gives the effective loss factor of

$$E\eta_{eff} = \mu_i\Omega \quad \text{or} \quad \eta_{eff} = \eta_v\Omega \quad (22)$$

where the η_v represents the internal viscous damping coefficient defined as

$$\eta_v = \frac{\mu_i}{E}. \quad (23)$$

This result indicates that the effective loss factor for internal viscous damping increases linearly with frequency, [11, 13, 17].

The internal damping coefficient η_v is related to the internal damping dashpot constant, c_i , if one inserts equation (23) into the following equation derived by Gunter [9]:

$$c_i = \left(\frac{\pi}{l} \right)^3 \mu_i l \quad (24)$$

where μ_i is the internal viscosity and l is the length of the material. Note equation (24) is for a beam (shaft) only.

To determine the energy dissipated per unit cycle, the dashpot in the viscous internal damping model is treated exactly the same as an external viscous dashpot. This yields the familiar equation of motion:

$$m\ddot{x} + c_i\dot{x} + kx = F \cos \Omega t \quad (25)$$

where again c_i is the internal damping constant. Similar to an external damper, the internal damper exerts a force that is proportional to and in anti-phase with the velocity. The mechanical impedance of equation (25) is given by:

$$Z_m = c_i + i\left(m\Omega - \frac{k}{\Omega}\right) \quad (26)$$

and the time average power dissipated by an oscillator is given by the equation:

$$\langle W \rangle = \frac{1}{2} \dot{\hat{x}}^2 \operatorname{Re}[Z_m] \quad (27)$$

where the $\dot{\hat{x}}^2$ term is the amplitude of the velocity phasor or $\Omega \hat{x}$, [5, 6]. To calculate the energy dissipated per cycle the following equation is used:

$$D = \langle W \rangle \frac{2\pi}{\Omega}, [5] \quad (28)$$

The energy dissipated per cycle for the viscous damping case is then calculated to be:

$$D = \pi \Omega \hat{x}^2 c_i \quad (29)$$

Like equation (21), this also confirms that the internal viscous damping model is rate dependent; in particular, it is linear with frequency, [4, 6].

Another consequence of this rate dependence can be seen from Figure 3. Since the angle ϕ in Figure 3 is related to the loss factor, from equation (17), both depend on the frequency. This means that as the frequency changes, the size of the ellipse also changes.

2.4 The Internal Hysteretic Damping Model

The first researches to identify internal hysteretic damping in rotating systems were Newkirk and Kimball in 1924 [8, 10]. They conducted rotordynamic tests on a series of different materials over a frequency range of 0.03 to 50 Hz at low stress amplitudes. Their experiment involved connecting a weight to the “overhang” end of the shaft by a bearing as shown in Figure 6. This allowed the shaft to rotate freely with a constant downward force. Newkirk and Kimball found that as the shaft was rotated, a

small deflection of the weight to one side occurred no matter what rotation speed was used.

After an analysis, they concluded that the angular deflection ϕ , shown in Figure 6, was caused by a force associated with the internal hysteretic damping of the material. By measuring this angle ϕ , and using it to calculate the amount of work done by the system to overcome the internal damping/friction, the log decrement associated with the material was determined. Since these initial tests, much experimental evidence has been gathered to confirm that internal hysteretic damping in a material is rate-independent, [7, 10]. In addition, it has been found that this damping force is in anti-phase with the velocity but proportional to the displacement, [6].

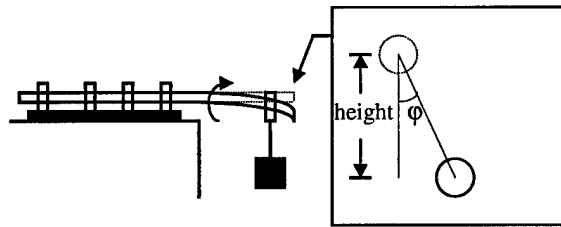


Figure 6: Kimball/Newkirk Testing Apparatus

To find the material loss factor from the measured angle ϕ , Kimball and Newkirk used the relationships between the stress and strain derived in Section 2.2. A summary is shown in Figure 7.

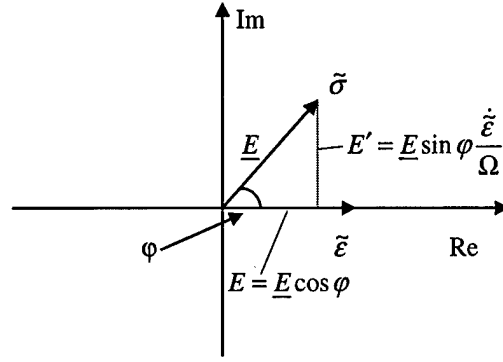


Figure 7: Stress and Strain Phasor Diagram (Modified)

Their analysis proceeds as follows: starting from the basic sine relationship of

$$\sin \varphi = \frac{E'}{\sqrt{(E)^2 + (E')^2}} \quad (30)$$

Factoring out E from the denominator and using equation (17) gives:

$$\sin \varphi = \frac{E'}{E \sqrt{(1)^2 + \left(\frac{E'}{E}\right)^2}} = \frac{\frac{E'}{E}}{\sqrt{1 + \left(\frac{E'}{E}\right)^2}} = \frac{\eta_H}{\sqrt{1 + \eta_H^2}} \quad (31)$$

Hence if φ is measured by the apparatus of Figure 6, η_H can be solved from the quadratic relationship given by equation (31). Again, for these types of materials, E and η are essentially constant. In contrast to the viscous model, having a constant loss factor dictates that the energy dissipation ellipse in Figure 3 does not change size with changing frequencies. It is also important to point out that the relationship between the material loss factor η_H and the structural loss factor ($\eta_{H\text{-struct}}$) depends on the geometry and loading of the structure. [6]

To calculate the axial stress/strain constitutive equation for the hysteretic model shown in Figure 8, the components of the complex storage modulus \underline{E} are used.

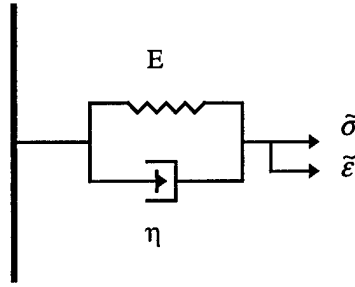


Figure 8: Linear Internal Hysteretic Damping Model

The component along the real axis in Figure 7 (associated with Young's Modulus) is found using the familiar in-phase stress strain of:

$$\text{Re}[\tilde{\sigma}] = \underline{E} \cos \varphi \tilde{\epsilon} \quad (32)$$

The component in the imaginary direction of the complex storage modulus is found from the quadrature stress-strain law which gives:

$$\text{Im}[\tilde{\sigma}] = \underline{E} \sin \varphi \frac{\dot{\tilde{\epsilon}}}{\Omega} \quad (33)$$

Together, they give

$$\tilde{\sigma} = \underline{E} \left[\tilde{\epsilon} \cos \varphi + \frac{\dot{\tilde{\epsilon}}}{\Omega} \sin \varphi \right] \quad (34)$$

Recalling equation (31) and recognizing that

$$\cos \varphi = \frac{1}{\sqrt{1 + \eta_H^2}} \quad (35)$$

gives the constitutive relationship

$$\tilde{\sigma} = \underline{E} \left[\frac{\tilde{\epsilon}}{\sqrt{1 + \eta_H^2}} + \frac{\dot{\tilde{\epsilon}} \eta_H}{\Omega \sqrt{1 + \eta_H^2}} \right] \quad (36)$$

which agrees with references [2, 8].

Writing equation (36) in complex notation gives:

$$\underline{\sigma}e^{i\Omega t} = \underline{E} \left[\frac{\underline{\varepsilon}e^{i\Omega t}}{\sqrt{1+\eta_H^2}} + \frac{d}{dt}(\underline{\varepsilon}e^{i\Omega t}) \frac{1}{\Omega} \frac{\eta_H}{\sqrt{1+\eta_H^2}} \right] \quad (37)$$

Evaluating the derivative and canceling out the appropriate terms yields:

$$\underline{\sigma} = \underline{E} \left[\frac{1}{\sqrt{1+\eta_H^2}} + i \frac{\eta_H}{\sqrt{1+\eta_H^2}} \right] \underline{\varepsilon} \quad (38)$$

or

$$\underline{\sigma} = \underline{E} \frac{1}{\sqrt{1+\eta_H^2}} [1 + i\eta_H] \underline{\varepsilon} \quad (39)$$

From Figure 7, it can be shown that

$$\underline{E} = \sqrt{(E)^2 + (E')^2} = E \sqrt{(1)^2 + \left(\frac{E'}{E}\right)^2} = E \sqrt{1+\eta_H^2} \quad (40)$$

If this substitution is made, the resulting equation

$$\underline{\sigma} = E(1 + i\eta_H) \underline{\varepsilon} \quad (41)$$

is in agreement with equation (18) and the previous results given in section 2.2.

It is important to note that unlike equation (21), the frequency, Ω , no longer remains in equation (41) when the material has internal hysteretic damping, validating the experimental results obtained by Kimball and Newkirk.

To calculate the energy dissipated per unit cycle, one must transform the variables from local material properties like E (Young's Modulus) to global structural properties like k (stiffness), to give:

$$\bar{F} = k(1 + i\eta_{H-struct}) \bar{x}. \quad (42)$$

In this equation the force and displacements are written as phasors while the structural stiffness is given by k , [6].

Now, if the lumped mass is included in the system, equation (42) becomes:

$$\tilde{F} = m\ddot{\tilde{x}} + k(1 + i\eta_H)\tilde{x} . \quad (43)$$

The mechanical impedance of this equation is found to be:

$$Z_m = \frac{k\eta_H}{\Omega} + i(m\Omega - \frac{k}{\Omega}) \quad (44)$$

Using the time average power dissipation equation, equation (27), the energy dissipated per unit cycle for the hysteretic model is calculated to be:

$$D = \pi \hat{x}^2 k \eta_H \quad (45)$$

This also confirms that the internal hysteretic damping model is independent of frequency, [6].

Although, the hysteretic damping model is typically associated with internal damping, occasionally, some have used this model for external damping. This external hysteretic damping model has the same frequency independence and energy dissipation characteristics as the internal model. But unlike internal damping, the external hysteretic damping model is always connected physically to the surrounding and always dissipates energy from the system, [6].

2.5 Internal Viscous Damping vs. Internal Hysteretic Damping

Once again, the difference between internal viscous damping and internal hysteretic damping lies in how the loss factor term is defined. For internal viscous damping, the η_v coefficient has been identified with the damping constant in equation (24), and was also shown to increase linearly with frequency, [6, 7, 8]. This damping force associated with the $c_v \dot{x}$ term is proportional to and in anti-phase with the velocity. For the internal hysteretic damping coefficient, η_H , experimental and analytical methods have been used to confirm its rate-independence, [10]. This damping force is in anti-phase with the velocity but proportional to the displacement.

To get a clear graphical explanation of the differences, recall that the enclosed area of the hysteresis ellipse in Figure 3 is the energy dissipated per cycle. For viscous internal damping, the angle between the stress and strain increases as the frequency increases, resulting in a larger and larger ellipse. In contrast, since the hysteretic internal damping coefficient and the angle remain constant, the ellipse does not change size or orientation with changing frequency.

To summarize the differences and to show how the models compare to some examples of real materials, Figure 9 and Table 1 are provided.

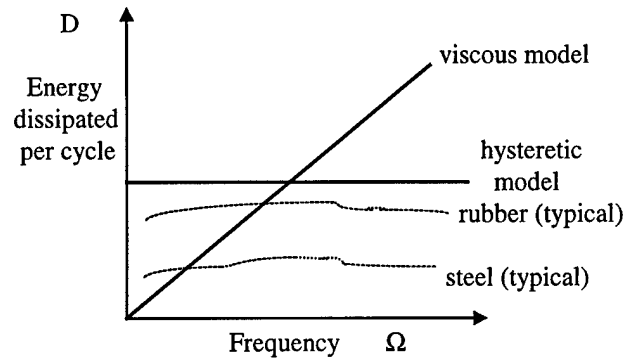


Figure 9: Variation of Energy Dissipated per Cycle with Frequency, [5]

Table 1: Forced Excitation of a Single Degree of Freedom System with Viscous or Hysteretic Damping, [5]

	Viscous Damping	Hysteretic Damping
Differential Equation	$m\ddot{x} + c\dot{x} + kx = F \cos \Omega t$	$m\ddot{x} + k(1 + i\eta_H)x = \text{Re}[Fe^{i\Omega t}]$
Particular Solution	$\frac{F}{\sqrt{(k - m\omega^2)^2 + (c\omega)^2}}$	$\frac{F}{\sqrt{(k - m\omega^2)^2 + (k\eta_H)^2}}$
Energy dissipated/cycle	$D = \pi\Omega\hat{x}^2c$	$D = \pi\hat{x}^2k\eta_H$
Resonant Frequency	Decreases with increasing value of c	Independent of value of η_H
Static Displacement at $x = 0$	$\frac{F}{k}$	Depends on η_H
Resonant Amplitude	Depends on all equation parameters	Independent of mass

From the figure and reference [5], it is clear that most systems do not appear to have a substantial amount of viscous damping. Although most materials do exhibit some characteristics of hysteretic internal damping, many experts admit that the subject matter is not well understood, [5, 8, 11]. Nevertheless, combinations and slight modifications of the two models appear to be useful for many applications.

Chapter 3 - Internal Damping in Rotors

3.1 Rotordynamic Basics

The simplest rotor model consists of a rigid circular disc centered on a massless shaft supported by rigid bearings. The rigid disc is only allowed to move in the x-y plane. This model, the Jeffcott or Laval rotor, is shown in Figure 11. The free vibration of this rotor is very similar to the two degree of freedom system in Figure 12 where the spring and dashpot pairs are perpendicular to one another. The equations of motion for any rotation speed are given by:

$$\begin{aligned} m\ddot{x} + c\dot{x} + kx &= 0 \\ m\ddot{y} + c\dot{y} + ky &= 0 \end{aligned} \tag{46}$$

The solution to these two equations describes the path of the shaft center and does not depend on the rotation speed of the shaft. In general, the natural motion of the shaft takes the form of an ellipse or in special cases a circle or a straight line, [12].

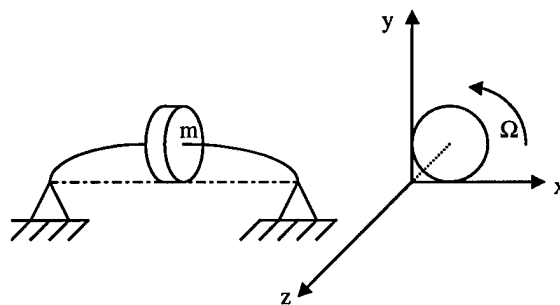


Figure 11: Jeffcott Rotor

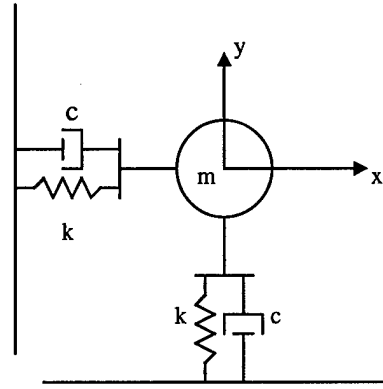


Figure 12: Jeffcott Rotor, Model for Natural Vibration

If the circular disc is not centered on the shaft, then gyroscopic forces, the moments of inertia of the disc, and the shaft spin speed all must be taken into account, [12]. A Jeffcott rotor with a non-central disc has equations of motion given by:

$$\begin{aligned}
 m\ddot{x} + k_{22}x - k_{23}\beta &= 0 \\
 m\ddot{y} + k_{22}y + k_{23}\delta &= 0 \\
 I_d\ddot{\delta} + I_p\Omega\dot{\beta} + k_{23}y + k_{33}\delta &= 0 \\
 I_d\ddot{\beta} - I_p\Omega\dot{\delta} - k_{23}x + k_{33}\beta &= 0
 \end{aligned}
 \tag{47a,b,c,d}$$

where the displacements are given by x and y and the rotations are given by δ and β as in Figure 13. The diametral and polar moments of inertia are given by I_d and I_p respectively while elements in the stiffness matrix are given by k_{ij} . The moments associated with the polar moment of inertia and the rotation speed in equations (47c,d) are gyroscopic moments.

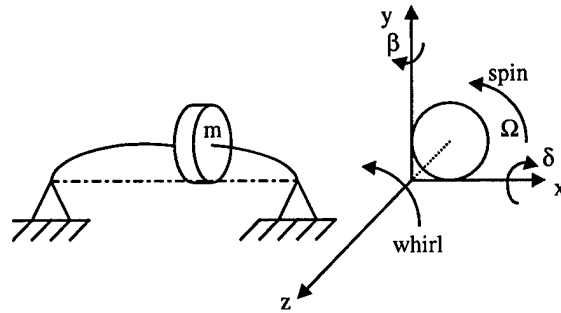


Figure 13: Jeffcott Rotor, Non-Centered Disc

By writing the equations in (47) in matrix notation, and assuming an exponential solution, four pairs of complex conjugate eigenvalues result in the form $S_j = \pm i\omega_j$.

These four natural frequencies result from the gyroscopic terms in equations (47) and the fact that the system has four degrees of freedom. A Campbell Diagram, such as Figure 14, shows how the eigenvalues change as the shaft spin speed increases, [12].

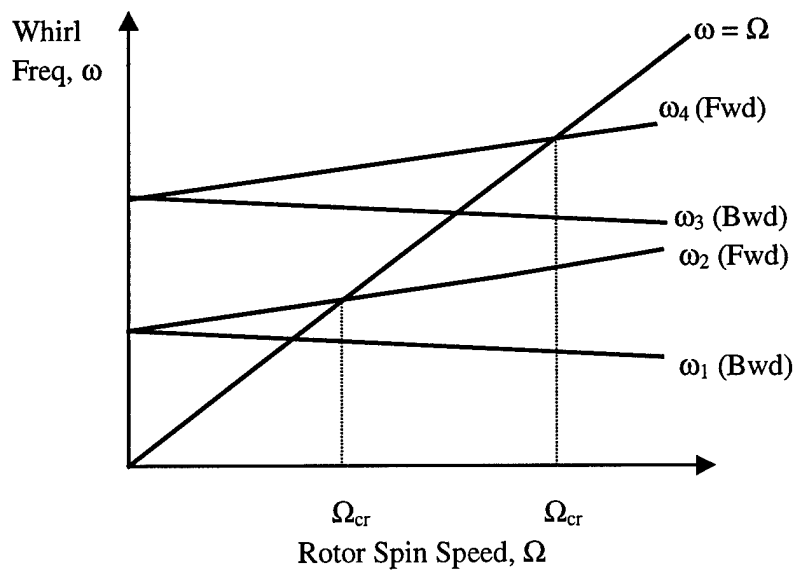


Figure 14: Campbell Diagram for Jeffcott Rotor

Based on the eigenvectors or mode shapes of the solution, the positive roots were labeled as the forward whirl frequencies, while the negative roots were labeled as the backward whirl frequencies. These definitions also correspond to physical observation as the positive roots were demonstrated by forward whirl (precession or whirl in the same direction of the rotation of the shaft) while the negative roots resulted in backward whirl (precession in the opposite direction of the rotation of the shaft), [12].

On Figure 14, it is important to point out two places where the rotor spin speed matches that of the forward natural whirling frequency of the rotor. These two locations are called critical speeds. A critical speed, is characterized by a large local amplitude vibration, similar to resonance, [9].

An important difference between the model with a non-central disc (or any shaft/rotor with gyroscopic forces) and the centered disc model is that the natural motion of the non-central disc is circular. In addition, it should be noted that the Jeffcott rotor with the centered disc only has a single natural frequency while the models with gyroscopic forces have four which depend on the shaft rotation speed, [12].

The simple model of a rotor with a non-centered disc can be further extended to include many other factors. Flexible bearings with external damping, an unbalance in the disc, and all forms of internal damping in the shaft can also be included to improve the model. The discussion by Kramer in [12] is a good reference that shows the development of these improved models.

3.2 Internal Viscous Damping

In 1933, Smith, [6], evaluated the effects of internal viscous damping on a rotating system. He proved that by including internal viscous damping in a rotating system without external damping, the system would become unstable at the first critical speed. This speed was called the instability threshold. He also showed that internal viscous damping actually has stabilizing effects if the system is kept at sub-critical speeds, and destabilizing effects above the critical speed.

A few years later, the study by Smith was confirmed by a number of authors. These included, but were not limited to, Kramer, [12], Ehrich, [13], Gunter, [9], and Dimarogonas, [14]. These authors clarified Smith's claim and showed that the introduction of internal viscous damping caused unstable, sub-synchronous rotor motion above the lowest critical speed, never below. Although the methods each author used to calculate the actual instability threshold differed, all of the general conclusions were the same. In addition, they also noted that if external damping is added to the system, the stability threshold can be made greater than the lowest critical speed, [9].

A direct and simple method to achieve the same results was introduced by Ehrich, [13]. He first began with the constitutive relationship given by equation (19):

$$\tilde{\sigma}_x = E\tilde{\epsilon}_x + \mu_i \frac{d\tilde{\epsilon}_x}{dt} \quad (19)$$

Using the linearized beam theory or plane sections remain plane (where the strain is proportional to the distance from the neutral axis) yields:

$$\epsilon_x = \epsilon_o \left(\frac{r}{r_o} \right) \cos \theta \quad (48)$$

where ϵ_0 is the strain at $r = r_0$, $\theta = 0$, see Figure 15.

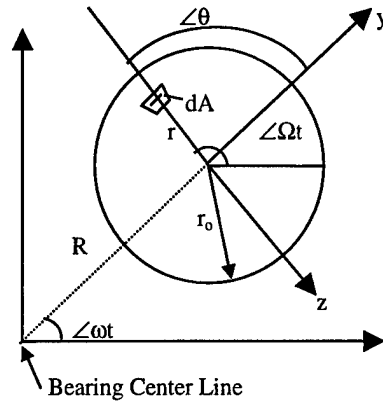


Figure 15: Rotating, Whirling Beam Cross Section, Ehrich, [13]

In this figure, the shaft is whirling about the bearing centerline with a speed of ω and spinning about the center of the shaft with speed of Ω . The y-axis is an extension of the whirl radius R and also rotates about the bearing centerline with a speed ω . Note that the z-axis remains perpendicular to the y-axis and the shaft rotates about the x-axis with respect to the y-z plane. Looking at the angles defined by the figure,

$$\theta = \Omega t - \omega t \text{ or } \dot{\theta} = \Omega - \omega \quad (49)$$

where $\dot{\theta}$ is the rotation rate of the shaft with respect to x, y, and z. If the motion is synchronous, i.e. $\Omega = \omega$, then $\dot{\theta} = 0$ and the shaft does not rotate with respect to the x, y, and z axes. Assuming sub-synchronous motion and combining equations (19), (48), and (49), gives

$$\sigma_x = \epsilon_0 \left(\frac{r}{r_0} \right) [E \cos \theta - \mu_i (\Omega - \omega) \sin \theta]. \quad (50)$$

If this stress is multiplied by the distance from the neutral axis of the shaft (z-axis) and integrated over the cross sectional area, the resulting moments become:

$$M_z = \int_A \sigma_x r \cos \theta dA = \frac{\epsilon_o}{r_o} EI \quad (51)$$

$$M_y = \int_A \sigma_x r \sin \theta dA = -\frac{\epsilon_o}{r_o} \mu_i I (\Omega - \omega) \quad (52)$$

The moment in the z direction is due to the bending of the shaft in the x-y plane (bearings remain fixed, shaft experiences jump rope like motion, or whirl). Since the shaft is not bent in the x-z plane, the moment in the y direction must be balanced by additional forces. To achieve equilibrium, a viscous internal damping force must be tangent to the shaft whirl orbit (see Figure 16). The particular direction of the force depends on the sign of the $(\Omega - \omega)$ term. For sub-synchronous motion it is positive (i.e. the spin speed is greater than the whirl speed). In this case the force is in the direction of the whirling shaft and feeds energy into the system, [6].

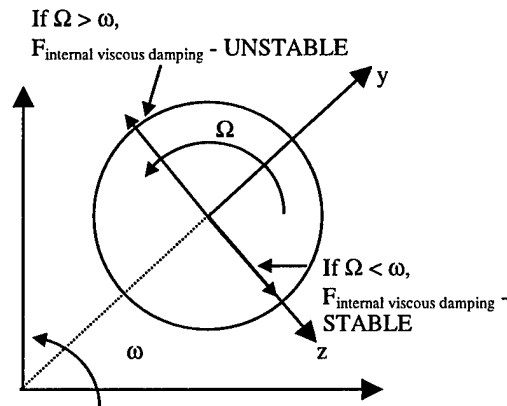


**Figure 16: Rotating, Whirling Beam Cross Section
Showing Direction of Internal Damping Force, No External Damping**

Recall the claim that any amount of external damping can improve the stability of the system. This fits into the above argument due to the fact that these external damping forces are always in the opposite direction of the shaft whirl, thereby removing energy

from the system. The stability lies in the comparison of the two forces (see Figure 17). If the external damping force dominates, the shaft is stable, but if the internal damping force dominates, the shaft is unstable. The instability threshold occurs where they exactly cancel.

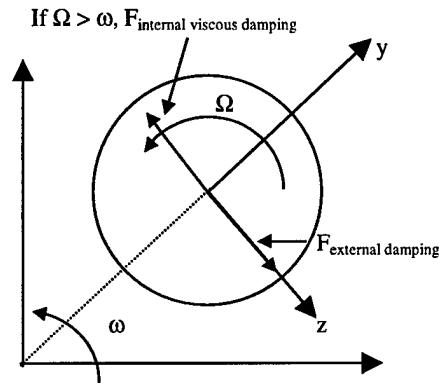


**Figure 17: Rotating, Whirling Beam Cross Section
Showing Directions of Internal and External Damping Forces**

Ehrich continues in the derivation to define values of both the internal and external forces and obtains:

$$F_{\text{internal damping}} = \mu_i (\Omega - \omega) I \frac{d^4 y}{dx^4} = c_i y_o (\Omega - \omega) \quad (53)$$

$$F_{\text{external damping}} = \mu_e \omega y_o = c_e y_o \omega \quad (54)$$

where y_o is the maximum shaft deflection.

At the instability threshold, the two forces are set equal to one another giving:

$$c_i (\Omega - \omega) = c_e \omega \quad (55)$$

At this point, the shaft will be whirling at its critical speed, (Ω_{cr}). This has been confirmed by observations made by Kimball, [10], and by a separate analysis by Ehrich, [13]. Making the $\omega = \Omega_{cr}$ substitution and rearranging the terms in a non-dimensional form leads to:

$$\frac{\Omega_{th}}{\Omega_{cr}} = \left(1 + \frac{c_e}{c_i} \right) \quad (56)$$

which agrees with Smith's original equation, [8].

To graphically represent the effects of viscous internal damping, Figure 18 shows a typical Campbell Diagram with whirl speed ω and rotor spin speed Ω . The first critical speed, Ω_{cr} , and the instability threshold speed, Ω_{th} , are shown on the spin speed axis. In this case, since the rotor does not become unstable at the first critical speed, a certain amount of external damping exists. Eventually, as the rotation speed, energy, and shaft amplitude/orbit increase, the bearings will not be able to dissipate all of the energy and the shaft will become unstable.

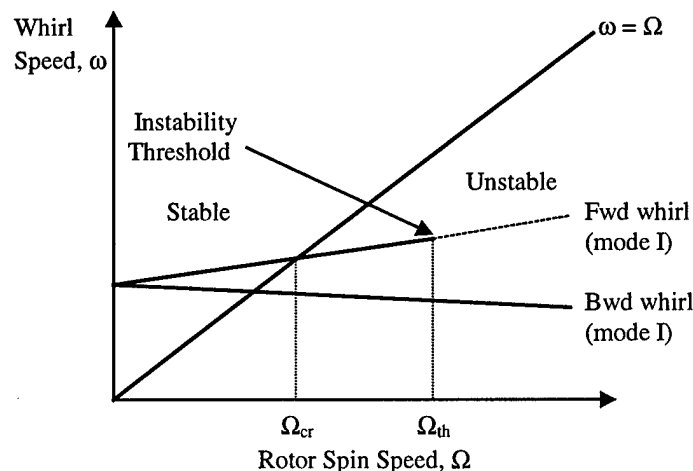


Figure 18: Campbell Diagram for Rotor with Internal and External Viscous Damping

3.3 Internal Hysteretic Damping

As noted previously in Chapter 2, the first researchers to study internal hysteretic damping in rotating systems were Newkirk and Kimball in 1924, [10]. While performing their tests and doing analyses, they concluded that internal hysteretic damping might be a possible cause for the shaft whirl and instability. Years later, Dimentberg, [15], and Lund, [11], took advantage of the work done by Kimball and incorporated internal hysteretic damping into the rotordynamic equations of motion.

Lund began his derivation with the internal hysteretic damping model (defined in Chapter 2). The constitutive relationship between the bending strain and bending stress for this model was originally expressed by Lund as:

$$\begin{aligned}\frac{d\theta}{dz} &= \frac{1}{EI} M_z \cos \gamma - \frac{1}{EI} M_y \sin \gamma = \frac{1}{EI\sqrt{1+\hat{\epsilon}^2}} \cdot (M_x - \hat{\epsilon} M_y) \\ \frac{d\phi}{dz} &= \frac{1}{EI} M_z \sin \gamma + \frac{1}{EI} M_y \cos \gamma = \frac{1}{EI\sqrt{1+\hat{\epsilon}^2}} \cdot (M_y + \hat{\epsilon} M_x)\end{aligned}\tag{57a,b}$$

where θ and ϕ are angular shaft displacement defined in Figure 19. The logarithmic decrement for the internal hysteretic damping of the shaft was related to the quantity $\hat{\epsilon}$ by

$$\hat{\epsilon} = \frac{\delta}{\pi}\tag{58}$$

and

$$\delta = \frac{2\pi\lambda}{\omega}\tag{59}$$

where the λ and the ω are the real and imaginary parts of the eigenvalue solution to the equations of motion. Note that the constitutive equations already suggest an iterative solution.

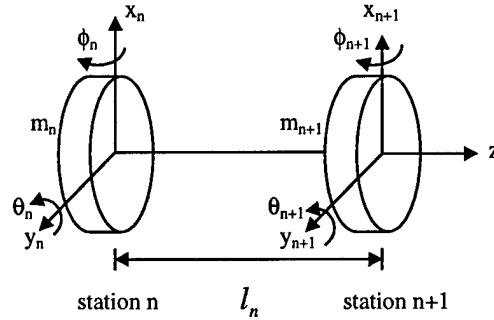


Figure 19: Rotor Configuration for Displacements, Lund

Note: Later Nelson, [2], refined the constitutive relationship into a more familiar form relating stress and strain directly, as described in Chapter 2:

$$\tilde{\sigma} = E \left[\frac{\tilde{\epsilon}}{\sqrt{1 + \eta_H^2}} + \frac{\dot{\tilde{\epsilon}} \eta_H}{\Omega \sqrt{1 + \eta_H^2}} \right] \quad (36)$$

Next, Lund modified the conventional FEM beam equations to include internal hysteretic damping and then converted them into a form suitable for the Myklestad-Prohl numerical method. This method involved representing the rotor by a series of lumped masses located at stations connected by uniform shaft sections, (somewhat similar to the modern finite element method). This technique produced the following equations used to solve for the displacement at the next station, $n+1$, based on the displacement of the previous one:

$$x_{n+1} = x_n + l_n \theta_n + \frac{1}{(EI)_n \sqrt{1 + \hat{\varepsilon}^2}} \cdot \left[\frac{l_n^2}{2} (M'_{xn} - \hat{\varepsilon} M'_{yn}) + \left(\frac{l_n^3}{6} - \frac{(lEI)_n}{(\kappa GA)_n} \right) (V'_{yn} + \hat{\varepsilon} V'_{xn}) \right] \quad (60a,b)$$

$$y_{n+1} = y_n + l_n \phi_n + \frac{1}{(EI)_n \sqrt{1 + \hat{\varepsilon}^2}} \cdot \left[\frac{l_n^2}{2} (M'_{yn} + \hat{\varepsilon} M'_{xn}) + \left(\frac{l_n^3}{6} - \frac{(lEI)_n}{(\kappa GA)_n} \right) (V'_{yn} - \hat{\varepsilon} V'_{xn}) \right]$$

$$\theta_{n+1} = \theta_n + \frac{1}{(EI)_n \sqrt{1 + \hat{\varepsilon}^2}} \cdot \left[l_n^2 (M'_{xn} - \hat{\varepsilon} M'_{yn}) + \frac{l_n^2}{2} (V'_{xn} - \hat{\varepsilon} V'_{yn}) \right] \quad (61a,b)$$

$$\phi_{n+1} = \phi_n + \frac{1}{(EI)_n \sqrt{1 + \hat{\varepsilon}^2}} \cdot \left[l_n^2 (M'_{yn} + \hat{\varepsilon} M'_{xn}) + \frac{l_n^2}{2} (V'_{yn} + \hat{\varepsilon} V'_{xn}) \right]$$

$$M_{x,n+1} = M'_{xn} + l_n V'_{xn}$$

$$M_{y,n+1} = M'_{yn} + l_n V'_{yn}$$

$$V_{x,n+1} = V'_{xn}$$

$$V_{y,n+1} = V'_{yn}$$

(62,a,b,c,d)

where the moments and shears are represented by M and V, and the shaft material and physical properties as κ , G, E, A and I (see Figure 20).

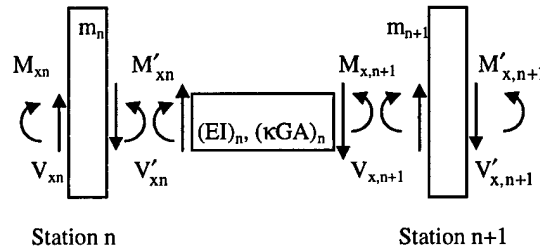


Figure 20: Rotor Configuration for Bending and Shear Forces, Lund

In addition to the displacements of the rotor, the Myklestad-Prohl method was also used to solve for the eigenvalues of the equations of motion. This solution took the form of $S = \lambda \pm i\omega$, where the real part indicated the growth/decay of the whirl orbit and the imaginary part represented the whirl speed noted previously. Lund then further

reduced this result into a more manageable form by the use of the log decrement given in equation (59):

$$\delta = -\frac{2\pi\lambda}{\omega} \quad (63)$$

Lund added the negative sign to indicate that positive values of the logarithmic decrement resulted in stable systems while negative values resulted in unstable systems.

Using this log decrement notation, the case for an undamped (no external damping) rotor system with internal hysteretic damping was solved. Lund found that the log decrement for all forward modes was always negative, which indicated instability. In addition, he found that the log decrement for all backward modes was always positive, which indicated stability. In a separate study mentioned by Lund, [11], he added external damping through the bearings to the rotating system, and found that the forward mode stability could be achieved for all speeds. The results and conclusions obtained by Lund agreed with the earlier analysis conducted by Dimentberg, [15].

3.4 The Effect of External Damping on the Instability Threshold

To assist in the study of the effect of external damping on the instability threshold, the Draper Laboratory FEM Rotor program was employed (see Chapter 4 for discussion and verification of this program). For this short numerical study, viscous external damping was applied separately to two rotor systems: one with internal viscous damping and one with internal hysteretic damping.

The first case that was run on the program, verified the results obtained by Smith and Ehrich, where the instability threshold for a system with internal and external viscous damping was given by:

$$\frac{\Omega_{th}}{\Omega_{cr}} = \left(1 + \frac{c_e}{c_i} \right) \quad (56)$$

Figure 21, shows the non-dimensional ratios of the instability threshold and the critical speed versus the ratio of the external viscous damping to internal viscous damping. The data from the finite element model solution match closely with equation (56). As more finite elements were added to the program, the results continued to approach the exact solution.

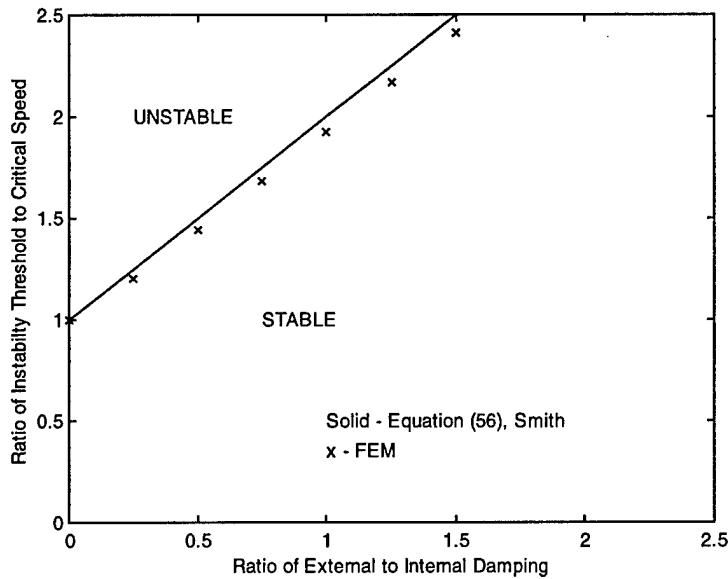


Figure 21: Stability Thresholds for Viscous Internal and Viscous External Damping

The next configuration involved adding viscous external damping to a rotor system with only hysteretic internal damping. Since the ratio of viscous external damping and hysteretic internal damping cannot be put in a non-dimensional form, a plot

different from Figure 21 was required to show the relationship. Figure 22 shows the values of viscous external damping (given by μ_e/E) required to maintain stability at all speeds for given values of internal hysteretic damping. For zero internal hysteretic damping, no viscous external damping is required to maintain stability. For increasing values of internal hysteretic damping, the required viscous damping to maintain stability at all speeds increases linearly. If the external viscous damping is less than that given by Figure 22, all of the forward modes will be unstable in a range of spin speeds beginning at $\Omega = 0+$.

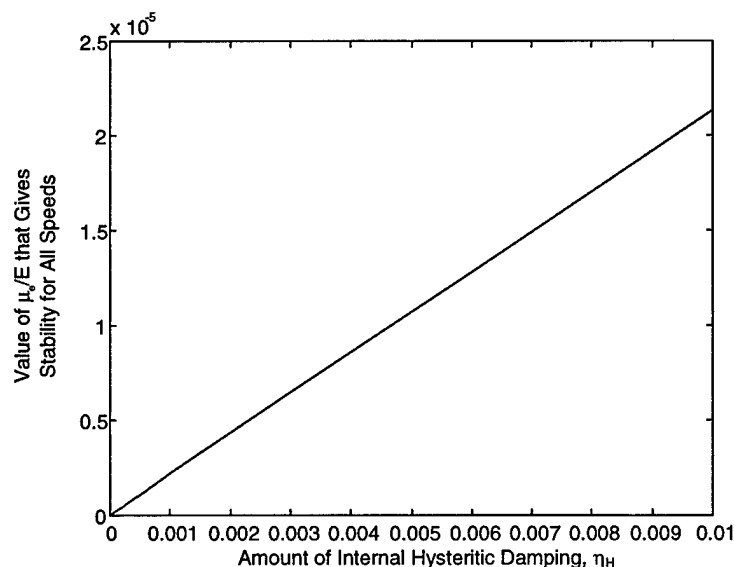


Figure 22: Amount of Viscous External Damping Required for Stability with Internal Hysteretic Damping

Another way to demonstrate this relationship is shown in Figure 23. This plots the log decrement of the eigenvalue solution (as defined by Lund, [11]) for fixed internal hysteretic damping as a function rotor spin speed Ω . It also shows a family of curves, which represent constant viscous external damping. Although it seems unlikely that the rotating system will ever be spun at the high speeds shown, it does appear that the rotor

would eventually become stable. As the external damping increases, the speed at which the system becomes stable approaches the origin. One conclusion from Figure 23 is that even though the rotor internal damping is speed independent (due to the internal hysteretic damping), the stability of the total system is indeed speed dependent due to the external viscous damped bearings. Figure 22 is consistent with the conclusions reached by Lund, [11] and Dimentberg, [15], but Figure 23 gives some new results on the interaction between external viscous damping and internal hysteretic damping.

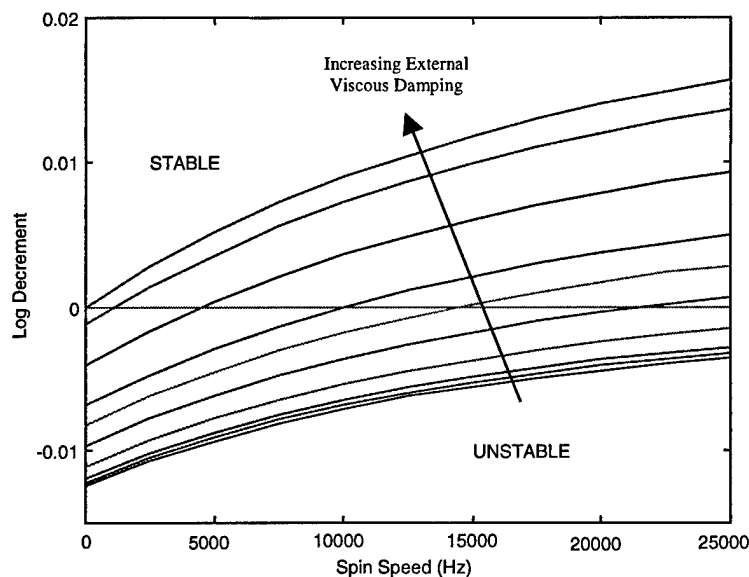


Figure 23: Log Decrement versus Spin Speed for System with Internal Hysteretic Damping and a Family of Constant External Viscous Damping Curves

The final configuration involved adding hysteretic external damping to a rotor system with only hysteretic internal damping. Although, the FEM model was not modified to represent the external hysteretic damping, it could be argued that one could draw the plot based on intuitive reasoning. First, since both external and internal damping are hysteretic, or speed independent, the logarithm decrement of the eigenvalue

solution versus the spin speed would be horizontal lines. (Note: In the next section, the FEM does actually support this claim for the case of zero external hysteretic damping. See Figure 31). Therefore, similar to the previous figure, Figure 24 plots the log decrement of the eigenvalue solution for fixed internal hysteretic damping as a function rotor spin speed Ω . But this time, the family of curves represents the constant external hysteretic damping. Note that as the external hysteretic damping is increased, the parallel lines shift toward the origin and toward stability.

Unlike the external viscous damping where the spin speed determines stability (no matter how much external damping is applied), the external hysteretic damping is the only factor in determining stability for this case. Figure 24 is consistent with the conclusions reached by Lund, [11] and Dimentberg, [15], although it clarifies them in the respect to the influence of external hysteretic damping to the stability of the system.

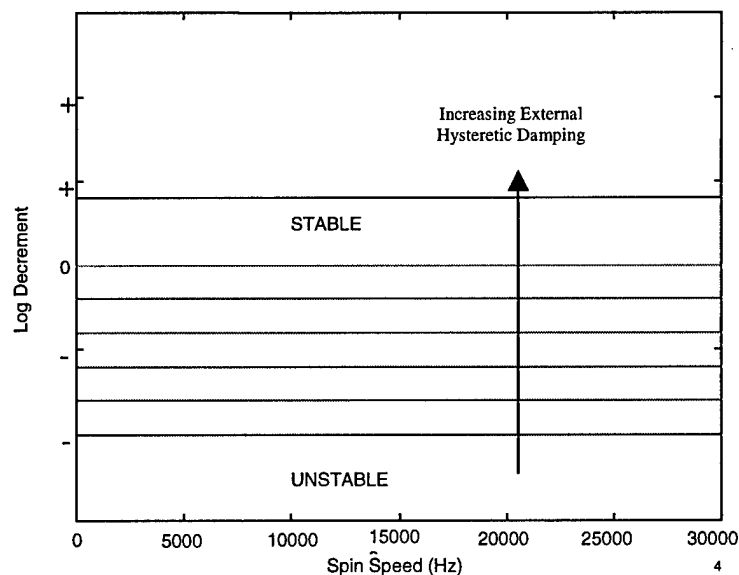


Figure 24: Log Decrement versus Spin Speed for System with Internal Hysteretic Damping and a Family of Constant External Hysteretic Damping Curves

One can now draw the following conclusions:

- If the external and internal damping are both viscous in nature, then the rotor will always be stable in its sub-critical speed range. Stability can be extended into the supercritical regime by adding external damping according to the results obtained by Smith in equation (56).
- If the external and internal damping are both hysteretic, the rotor will be unstable for all speeds unless the external damping is large enough to establish stability. In this case, the rotor will be stable for all speeds.
- If the external damping is viscous and the internal damping is hysteretic, the rotor will be unstable in a range of speeds beginning at $\Omega = 0+$. As the external viscous damping increases, this speed range shrinks toward $\Omega = 0$ until the external damping reaches a value that results in stability for all speeds, i.e. for $\Omega \geq 0$.

Chapter 4 Finite Element Model of Rotor

4.1 Finite Element Method - A Timoshenko Rotor Element

In recent years, the finite element method has been successfully applied to rotordynamic systems. Although all rotor elements are based on the simple beam element, a number of variations have been developed. One such element is based on Timoshenko beam theory. This element has 2 nodes and 8 Degrees of Freedom and uses third order shape functions to describe the bending of the elements. All additional inertia are assumed to be rigid discs with lumped mass properties and the bearings are assumed to be linear and discrete. The model includes rotary inertia, gyroscopic moments, and shear deformation effects. A more detailed discussion of a Timoshenko rotor element is located in Appendix B.

In the late seventies, Nelson published several papers, [16, 17], to determine the accuracy of the Timoshenko rotor element and to document current works. His technique used the Lagrangian approach and was based on the potential and kinetic energy of the rotating element in Figure 25.

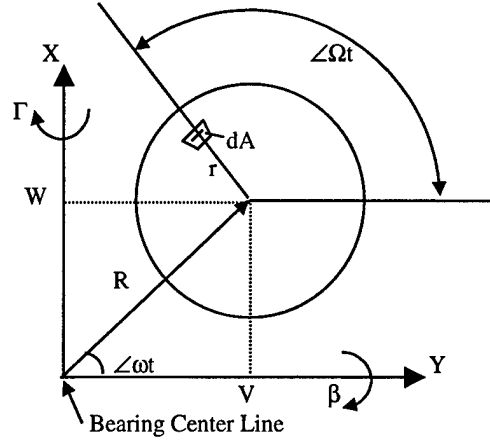


Figure 25: Rotor System Configuration, Nelson

The potential energy of the rotor was stored in two forms, bending deformation, and shear deformation (axial loads were neglected) and was given by:

$$V = \int_0^l \frac{1}{2} EI \begin{Bmatrix} V''_{bend} \\ W''_{bend} \end{Bmatrix}^T \begin{Bmatrix} V''_{bend} \\ W''_{bend} \end{Bmatrix} dz + \int_0^l \frac{1}{2} \kappa AG \begin{Bmatrix} V''_{shear} \\ W''_{shear} \end{Bmatrix}^T \begin{Bmatrix} V''_{shear} \\ W''_{shear} \end{Bmatrix} dz \quad (64)$$

where the shear deformation factor is given by κ and the second derivative of the bending deformation in the y direction is represented by V''_{bend} . The rotor kinetic energy included Timoshenko effects of rotary inertia, shear deformation, and the gyroscopic energy. It was given by:

$$T = \int_0^l \frac{1}{2} \rho A \begin{Bmatrix} \dot{V} \\ \dot{W} \end{Bmatrix}^T \begin{Bmatrix} \dot{V} \\ \dot{W} \end{Bmatrix} dz + \int_0^l \frac{1}{2} \rho I_d \begin{Bmatrix} \dot{\beta} \\ \dot{\Gamma} \end{Bmatrix}^T \begin{Bmatrix} \dot{\beta} \\ \dot{\Gamma} \end{Bmatrix} dz + \int_0^l \frac{1}{2} \rho I_p \Omega^2 ds - \int_0^l I_p \Omega \beta \dot{\Gamma} dz \quad (65)$$

Evaluating these integrals leads to the familiar forms for equations (64) and (65):

$$V = \frac{1}{2} \{q\}^T ([K_{bend}] + [K_{shear}]) \{q\} \quad (66)$$

$$T = \frac{1}{2} \{\ddot{q}\}^T ([M_{trans}] - [M_{rot}]) \{\ddot{q}\} - \Omega \{\dot{q}\}^T ([G]) \{\dot{q}\} + \frac{1}{2} I_p \Omega^2 \quad (67)$$

Nelson then proceeded to systematically derive the element matrices in equations (66) and (67) (see Appendix B). By the application of Hamilton's extended principle, and using the above equations, Nelson produced the following undamped matrix equations of motion:

$$([M_{trans}] + [M_{rot}]) \{\ddot{q}\} - \Omega [G] \{\dot{q}\} + [C_e] \{\dot{q}\} + [K] \{q\} = \{f\} \quad (68)$$

where:

$\{q\}$ - fixed frame physical coordinates

$\{f\}$ - fixed frame external forces

$[C_e]$ - external damping matrix

Similar to the Jeffcott rotor with the non-central disc, the eigenvalues for the undamped equation of motion (where $[C_e] = 0$) occur in conjugate pairs. The eigenvalues are given by: $S_j = \pm i\omega_j$, where the imaginary pair $\pm i\omega$ represents the forward and backward whirl frequencies of the shaft.

4.2 Addition of Internal Damping

Based on the work of Zorzi and Nelson, [2], the previous derivation of the rotordynamic equations of motion can be extended to include the contributions of internal damping. Nelson used both of the internal viscous and hysteretic damping models discussed in the previous chapters. Adding the constitutive relationship of equations (19) and (36) yields the following equation:

$$\sigma_x = E \left\{ \frac{\epsilon_x}{\sqrt{1+\eta_H^2}} + \left(\eta_v + \frac{\eta_H}{\Omega \sqrt{1+\eta_H^2}} \right) \dot{\epsilon}_x \right\} \quad (69)$$

After substituting the modified constitutive relationship into the internal bending moments and performing the integrations, the moments can be expressed as:

$$\begin{Bmatrix} M_z \\ M_y \end{Bmatrix} = EI \begin{bmatrix} \frac{1+\eta_H}{\sqrt{1+\eta_H^2}} & \left(\frac{1+\eta_H}{\sqrt{1+\eta_H^2}} + \eta_v \Omega \right) \\ \left(\frac{1+\eta_H}{\sqrt{1+\eta_H^2}} + \eta_v \Omega \right) & -\frac{1+\eta_H}{\sqrt{1+\eta_H^2}} \end{bmatrix} \begin{Bmatrix} V'' \\ W'' \end{Bmatrix} + EI \begin{bmatrix} \eta_v & 0 \\ 0 & -\eta_v \end{bmatrix} \begin{Bmatrix} \dot{V}'' \\ \dot{W}'' \end{Bmatrix} \quad (70)$$

where the internal damping matrix was defined as:

$$[\eta] = \begin{bmatrix} \frac{1+\eta_H}{\sqrt{1+\eta_H^2}} & \left(\frac{1+\eta_H}{\sqrt{1+\eta_H^2}} + \eta_v \Omega \right) \\ \left(\frac{1+\eta_H}{\sqrt{1+\eta_H^2}} + \eta_v \Omega \right) & -\frac{1+\eta_H}{\sqrt{1+\eta_H^2}} \end{bmatrix} \quad (71)$$

Now placing the energy contributions from these moment equations into the appropriate kinetic or potential energy equations (Lagrangian approach), Nelson finally proceeds to derive the equation of motion for a Timoshenko shaft finite element with internal damping. This is given by:

$$([M_{trans}] + [M_{rot}])\{\ddot{q}\} + (\eta_v[K] - \Omega[G] + [C_e])\{\dot{q}\} + \left[\frac{1+\eta_H}{\sqrt{1+\eta_H^2}}[K] + \left(\eta_v \Omega + \frac{\eta_H}{\sqrt{1+\eta_H^2}} \right)[K_{cir}] \right]\{q\} = \{f\} \quad (72)$$

All of the instabilities of the system are characterized in the new skew-symmetric circulation stiffness matrix, [2]. It is given by:

$$[K_{cir}] = \frac{EI}{l^3} \begin{bmatrix} 0 & & & & & & & \\ -12 & 0 & & & & & & \\ 6l & 0 & 0 & & & & & \\ 0 & 6l & -4l^2 & 0 & & & & \\ 0 & -12 & 6l & 0 & 0 & & & \\ 12 & 0 & 0 & 6l & -12 & 0 & & \\ 6l & 0 & 0 & 2l^2 & -6l & 0 & 0 & \\ 0 & 6l & -2l^2 & 0 & 0 & -6l & -4l^2 & 0 \end{bmatrix} \quad (73)$$

(Incidentally, the circulation matrix given in reference [2] was incorrect due to misplaced negative signs. Equation (73) is the correct circulation matrix.) It is also important to point out the significance of the $\eta_v[K]\{\dot{q}\}$ term in equation (72). Although this term involves the viscous internal damping coefficient, it does not produce instabilities. Recall Figure 16 where the direction of the internal viscous damping force depended on the sign of the $(\Omega - \omega)$ term in equation (53). Equation (72) takes this effect into account by the $\eta_v[K]\{\dot{q}\}$ term. At spin speeds less than the critical speed (for systems without external damping), this term dominates, resulting in a stable system. But at speeds above the critical speed, the terms involved with the circulation matrix dominate, resulting in an unstable system. This is in agreement with the findings documented by Smith [6] and Ehrich [13], and is also consistent with Figure 16 in Chapter 3.

Solving the equations of motion with internal damping results in eigenvalues in the now familiar form of: $S_j = \lambda_j \pm i\omega_j$, where again, ω provides shaft whirl frequency and λ provides the orbit growth/decay rate after a perturbation. Nelson then followed Lund's logarithm decrement approach in determining where the rotor system became unstable. (Recall that the instability threshold occurs when the δ crosses zero when approaching from positive values.) The Campbell Diagram in Figure 26 shows a rotor

with both internal viscous and hysteretic damping and external damping. It gives a good indication of how the stability of the rotor changes as the values of δ approach and surpass zero (at the instability threshold).

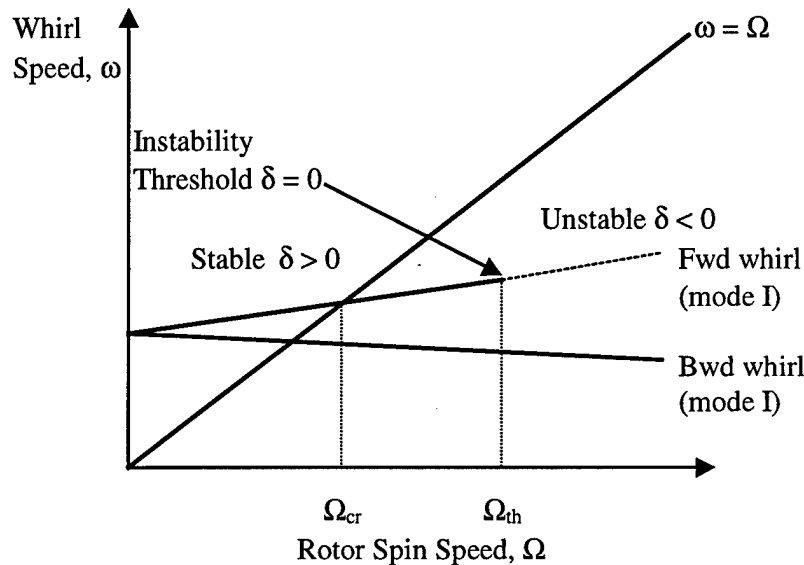


Figure 26: Campbell Diagram for Rotor with Internal and External Damping

4.3 Validation of FEM Model

In line with its work on magnetic bearings, The Charles Stark Draper Laboratory has produced a rotor dynamic finite element model (Antkowiak) that is based on undamped Timoshenko beam theory. In this model, all additional inertia are assumed to be rigid discs with lumped mass properties and the bearings are assumed to be discrete, undamped, and linear. The model includes rotary inertia, gyroscopic moments, and shear deformation effects.

After making the appropriate modifications to include internal and external damping, several test cases were run to check the accuracy of the extended rotor model. The bulk of the test cases were taken directly from Nelson, [2]. The following gives details on some of the validation of the extended rotor FEM model.

The first case involved an undamped (no internal or external damping) steel rotor supported by identical bearings. The physical dimensions of the rotor were a length of 1.27 meters and a diameter of 10.16 cm. The stiffness of the undamped isotropic bearings was 1.75×10^7 N/m.

Figures 27 and 28 show the agreement between the Draper extended model and Nelson's solution. The first critical speed given by Nelson was 4950 rpm, while the Draper FEM model calculated 4976 rpm. The small discrepancies could be attributed to the fact that this particular example by Nelson did not take into account shear effects.

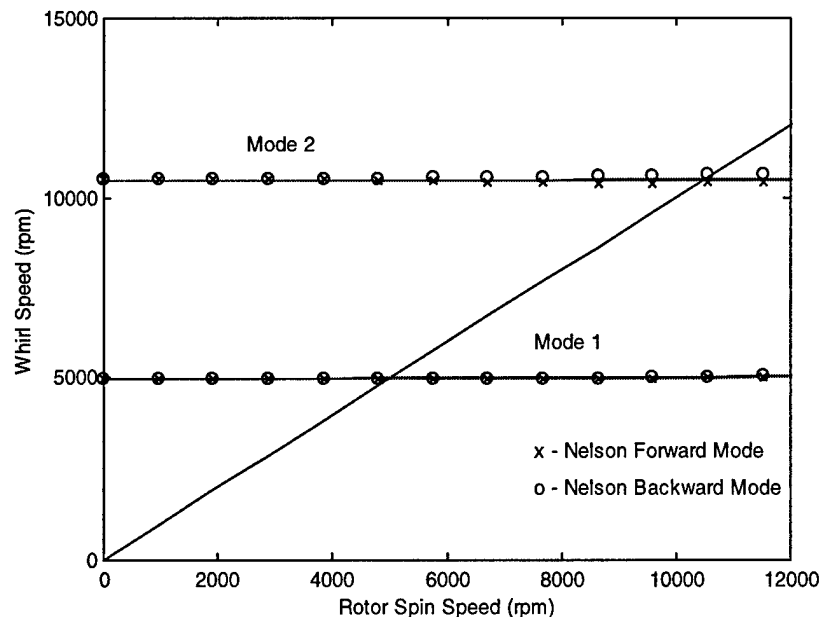


Figure 27: Draper FEM Model Compared to Nelson Solution, Undamped Rotor Supported by Identical Bearings, Modes 1 and 2

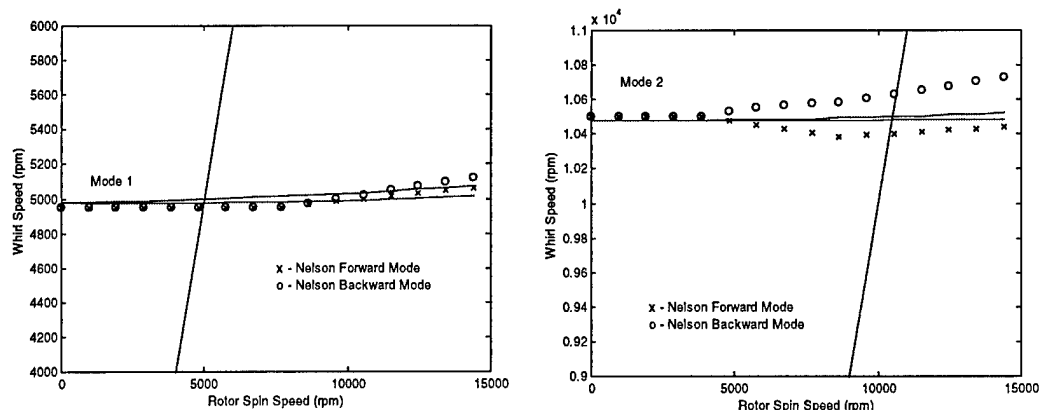


Figure 28: Draper FEM Model Compared to Nelson Solution, Undamped Rotor Supported by Identical Bearings, Modes 1 and 2 (Detailed View)

The next test case involved the same rotor but also included internal viscous damping in the rotor (no external damping). The amount of internal viscous damping was $\eta_v = 0.0002 \text{ sec}^{-1}$. Figure 29 shows the logarithm decrements of the first and second modes (both forward and backward) as a function of spin speed. The positive values of the log decrement indicate that the system is stable, while the negative values indicate instability. Good agreement is shown between the Draper FEM extended model and Nelson.

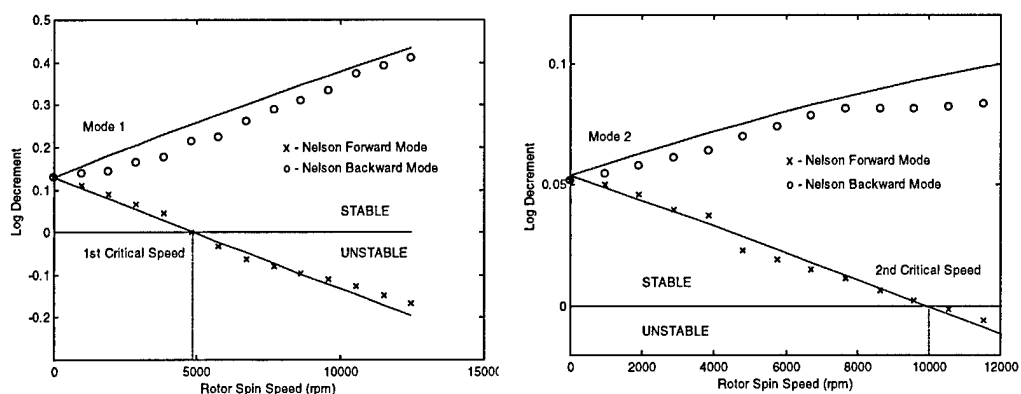


Figure 29: Log Decrements, Rotor with Viscous Internal Damping, No External Damping, Modes 1 and 2

It is important to point out that the log decrements for the all of the backward modes are increasing and therefore will always be stable. On the other hand, the forward modes initially are stable for speeds under their respective critical speeds, then become unstable as the log decrement crosses the x-axis. Note that this agrees with the theory of internal viscous damping described in Chapter 3.

Figure 30 shows the logarithm decrements of the first and second modes when external viscous damping is added to the rotor system through the bearings. The exact amount of external damping added to the bearings was 1.75×10^3 Ns/m. Close agreement is again shown. Note that the stability of the system was improved, i.e. the instability threshold was moved approximately 5,000 rpm higher than the first critical speed. In fact, the second forward mode will remain stable past 15,000 rpm. This effect of adding external damping to the system also agrees with the internal viscous damping model in Chapter 3 and in Figure 21.

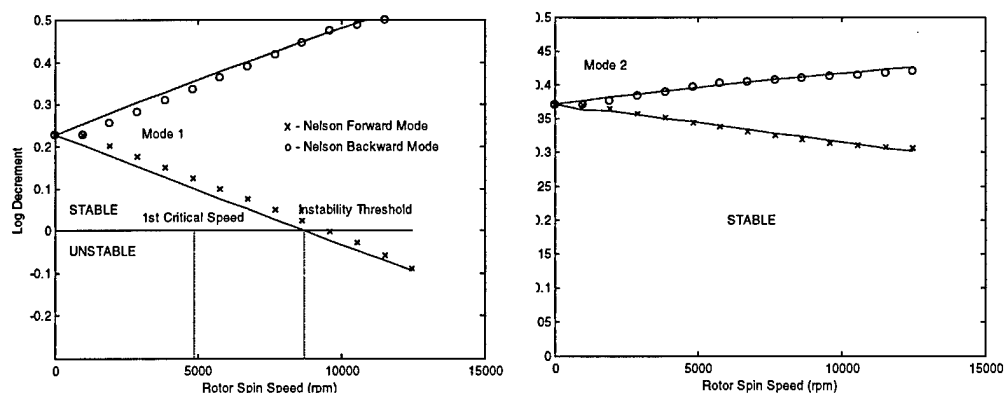


Figure 30: Log Decrements, Rotor with Viscous Internal Damping and Viscous External Damping

The next validation involved returning to the same rotor and this time only included internal hysteretic damping ($\eta_H = 0.0002$). Figure 31 shows good agreement

between the log decrements calculated by the Draper FEM extended model and Nelson. Similar to the results calculated by Lund and Dimentberg (described in Chapter 3), all of the forward modes are unstable and all of the backward modes are stable.

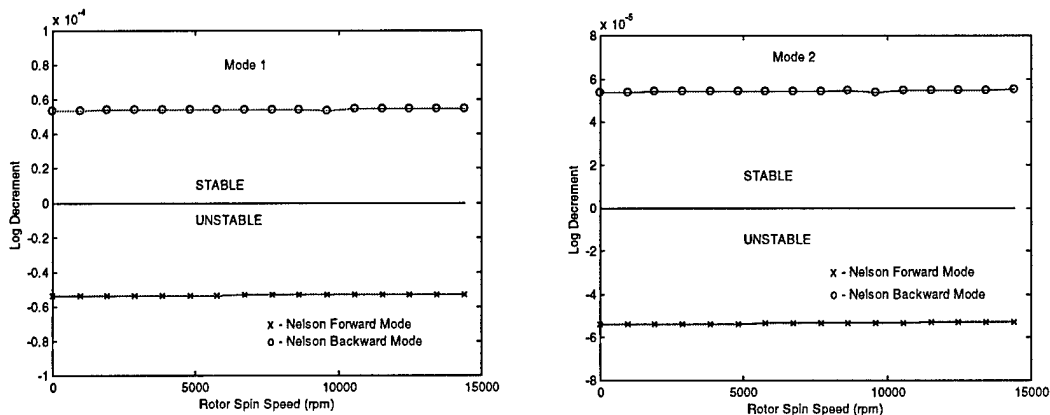


Figure 31: Log Decrements, Rotor with Hysteretic Internal Damping, No External Damping, Modes 1 and 2

Figure 32 shows the logarithm decrements of the first and second modes when external viscous damping is added through the bearings to this rotor system. This addition of 1.75×10^3 Ns/m per bearing completely overcame the effects of the internal hysteretic damping ($\eta_H = 0.0002$), resulting in a rotor system stable for all speeds (both forward and backward modes).

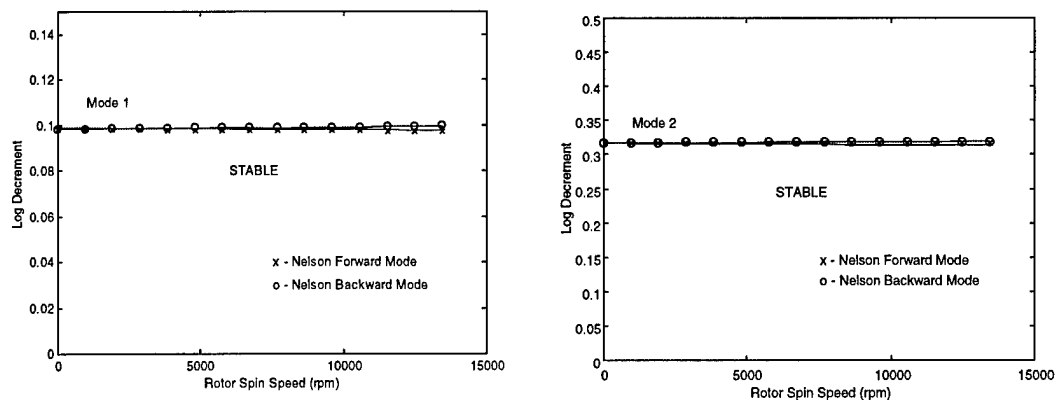


Figure 32: Log Decrements, Rotor with Hysteretic Internal Damping and Viscous External Damping

The extended rotor FEM model was successfully validated with the test cases provided by Nelson, [2]. Now it could be used to predict the critical speeds and instability thresholds for other rotors.

Chapter 5 Magnetic Bearing Simulation Design

5.1 State-Space Model of Rotor – No Internal Damping

In addition to calculating the critical speeds, the original Draper Lab FEM program (Antkowiak) was also designed to produce state space matrices that described the rotor system. This state space model was then placed in a Matlab™ magnetic bearing simulation developed by Draper Laboratory (Scholten) to test the closed loop control of the entire rotor system. Originally, the program produced a state-space model that did not include internal damping and only included a small amount of external damping estimated by the relationship:

$$[C_e] \approx 2[\zeta\omega], \text{ diagonal} \quad (74)$$

where the external viscous damping ratio was given by ζ .

The original FEM model used generalized eigenvectors, modal coordinates and state space coordinates to calculate the state-space model. First, the undamped, non-rotating, homogeneous equation of motion in physical coordinates,

$$[M]\{\ddot{q}\} + [K]\{q\} = [0] \quad (75)$$

was used to find a set of eigenvectors and eigenvalues. These eigenvectors were then placed in the $\hat{n} \times \hat{n}$ modal matrix $[\Phi]$, where each column represented a different eigenvector or mode.

$$[\Phi] = \begin{bmatrix} P_1^{(1)} & P_1^{(2)} & \dots & P_1^{(\hat{n})} \\ P_2^{(1)} & P_2^{(2)} & & \\ \vdots & & \ddots & \\ P_{\hat{n}}^{(1)} & & & P_{\hat{n}}^{(\hat{n})} \end{bmatrix} \quad (76)$$

The eigenvectors were then mass normalized by the following equation:

$$[\underline{\Phi}] = \left[\frac{\{\Phi^{(1)}\}}{\sqrt{\{\Phi^{(1)}\}^T [M] \{\Phi^{(1)}\}}} \quad \frac{\{\Phi^{(2)}\}}{\sqrt{\{\Phi^{(2)}\}^T [M] \{\Phi^{(2)}\}}} \quad \dots \quad \frac{\{\Phi^{(\hat{n})}\}}{\sqrt{\{\Phi^{(\hat{n})}\}^T [M] \{\Phi^{(\hat{n})}\}}} \right] \quad (77)$$

If one converts the entire non-homogeneous differential equation derived by Nelson,

$$([M_{trans}] + [M_{rot}])\{\ddot{q}\} - \Omega[G]\{\dot{q}\} + [C_e]\{\dot{q}\} + [K]\{q\} = \{f\} \quad (69)$$

to modal coordinates, it becomes:

$$([M_{trans}] + [M_{rot}])[\underline{\Phi}]\{\ddot{\xi}\} + ([C_e] - \Omega[G])[\underline{\Phi}]\{\dot{\xi}\} + [K][\underline{\Phi}]\{\xi\} = \{f(t)\} \quad (78)$$

where the output in physical coordinates q is given by modal coordinates, ξ , in the form of:

$$\{q\} = [\underline{\Phi}]\{\xi\} \quad (79)$$

Now, if equation (78) is pre-multiplied by the transpose of the mass normalized modal matrix, $[\underline{\Phi}]^T$, it gives

$$[\underline{\Phi}]^T ([M_{trans}] + [M_{rot}])[\underline{\Phi}]\{\ddot{\xi}\} + [\underline{\Phi}]^T ([C_e] - \Omega[G])[\underline{\Phi}]\{\dot{\xi}\} + [\underline{\Phi}]^T [K][\underline{\Phi}]\{\xi\} = [\underline{\Phi}]^T \{f(t)\} \quad (80)$$

This form of the equation lends itself to the use the property of orthogonality where:

$$\begin{aligned} [\underline{\Phi}]^T ([M_{trans}] + [M_{rot}])[\underline{\Phi}] &= [I], \text{ diagonal} \\ [\underline{\Phi}]^T (-\Omega[G] + [C_e])[\underline{\Phi}] &= ([G] + 2[\zeta\omega]) \\ [\underline{\Phi}]^T [K][\underline{\Phi}] &= [\omega^2], \text{ diagonal} \end{aligned} \quad (81a,b,c)$$

At this point, a modal reduction technique was used to reduce the number of states in the mass, stiffness, and gyroscopic matrices of equations (81). This eliminated the higher frequency modes outside the speed range of interest.

When the property of orthogonality is used, equation (80) reduces to:

$$\{\ddot{\xi}\} + (2[\zeta\omega] + [G])\{\dot{\xi}\} + [\omega^2]\{\xi\} = [\Phi]^T [L]\{f(t)\} \quad (82)$$

where again, the external damping is estimated by:

$$[C_e] \approx 2[\zeta\omega], \text{ diagonal} \quad (74)$$

It is important to emphasize that this is an approximation since $[\Phi]^T [C_e] [\Phi]$ will not, in general, be diagonal.

If one lets \hat{m} forces be applied to rotor at the appropriate nodal points, the force vector force vector $\{f(t)\}$ in equation (82) must be modified to account for the difference between the number of forces applied, \hat{m} , and the number of modes in the modal matrix, \hat{n} . This inflation is accomplished by the $\hat{n} \times \hat{m}$ matrix $[L]$ where

$$\begin{array}{ccc} [L] & \{f\} & \longrightarrow [L]\{f\} \\ \hat{n} \times \hat{m} & \hat{m} \times 1 & \hat{n} \times 1 \end{array} \quad (83)$$

To construct the state space model, the equations of motion must now be converted to state space coordinates of the form:

$$\{\alpha\} = [\{\xi\}, \{\dot{\xi}\}]^T \quad (84)$$

With this substitution, the equation of motion (82), in matrix notation, becomes:

$$[0] \quad [I] \{\dot{\alpha}\} + [\omega^2] \quad [(2[\zeta\omega] + [G])] \{\alpha\} = [\Phi]^T [L]\{f(t)\} \quad (85)$$

If equation (85) is combined with the identity

$$[I] \quad [0] \{\dot{\alpha}\} + [0] \quad -[I] \{\alpha\} = 0 \quad (86)$$

it gives:

$$\begin{bmatrix} [I] & [0] \\ [0] & [I] \end{bmatrix} \{\dot{\alpha}\} + \begin{bmatrix} [0] & -[I] \\ [\omega^2] & -(2[\zeta\omega] + [\underline{G}]) \end{bmatrix} \{\alpha\} = [\underline{\Phi}]^T [L] \{f(t)\} \quad (87)$$

Now using the standard definitions for state space theory, equation (87) can also be written as

$$\{\dot{\alpha}\} = [A]\{\alpha\} + [B]\{f(t)\} \quad (88)$$

where the state space dynamics matrix $[A]$ is defined as

$$[A] = \begin{bmatrix} [0] & [I] \\ -[\omega^2] & -(2[\zeta\omega] + [\underline{G}]) \end{bmatrix}, 2\hat{n} \times 2\hat{n} \quad (89)$$

and the state space actuator matrix, $[B]$, is defined as

$$[B] = \begin{bmatrix} [0] \\ [\underline{\Phi}]^T [L] \end{bmatrix}, 2\hat{n} \times \hat{m} \quad (90)$$

To recover the physical displacements of the output at all nodes (or locations defined by the actuator matrix), state space theory requires that

$$\{q\} = [C]\{\alpha\} \quad (91)$$

where the sensor matrix, $[C]$, is defined as:

$$[C] = [\underline{\Phi} \quad [0]], \hat{m} \times 2\hat{n} \quad (92)$$

Although this definition of the sensor matrix requires the displacement sensors to be co-located at the positions that the forces are applied, the original model and simulation did take into account the fact that the sensors were not exactly collocated with the magnetic bearing actuators.

5.2 State-Space Model of Rotor – Internal Damping Included

If internal damping is included in the FEM model and equations of motion (creating the new extended rotor model), the method to calculate the state-space model remains the same, but the results are more complicated. Starting with the same undamped, non-rotating, homogeneous equation of motion in physical coordinates,

$$[M]\{\ddot{q}\} + [K]\{q\} = [0] , \quad (75)$$

a set of eigenvalues and eigenvectors are calculated. These eigenvectors were then placed in the modal matrix $[\Phi]$, and were mass normalized by equation (77). If one converts the entire non-homogeneous differential equation derived by Nelson,

$$([M_{trans}] + [M_{rot}])\{\ddot{q}\} + (\eta_v[K] - \Omega[G] + [C_e])\{\dot{q}\} + \left[\frac{1 + \eta_H}{\sqrt{1 + \eta_H^2}}[K] + (\eta_v\Omega + \frac{\eta_H}{\sqrt{1 + \eta_H^2}})[K_{cir}] \right]\{q\} = \{f(t)\} \quad (71)$$

to modal coordinates, it becomes:

$$([M_{trans}] + [M_{rot}])[\Phi]\{\ddot{\xi}\} + (\eta_v[K] - \Omega[G] + [C_e])[\Phi]\{\dot{\xi}\} + \left[\frac{1 + \eta_H}{\sqrt{1 + \eta_H^2}}[K] + (\eta_v\Omega + \frac{\eta_H}{\sqrt{1 + \eta_H^2}})[K_{cir}] \right][\Phi]\{\xi\} = \{f(t)\} \quad (93)$$

where the output in physical coordinates, q , is given by modal coordinates, ξ , in the form of:

$$\{q\} = [\Phi]\{\xi\} \quad (79)$$

Now, if equation (93) is pre-multiplied by the transpose of the mass normalized modal matrix, $[\Phi]^T$, it gives

$$\begin{aligned}
& [\underline{\Phi}]^T ([M_{trans}] + [M_{rot}]) [\underline{\Phi}] \{\ddot{\xi}\} + [\underline{\Phi}]^T (\eta_v [K] - \Omega [G] + [C_e]) [\underline{\Phi}] \{\dot{\xi}\} + \\
& [\underline{\Phi}]^T \left[\frac{1 + \eta_H}{\sqrt{1 + \eta_H^2}} [K] + (\eta_v \Omega + \frac{\eta_H}{\sqrt{1 + \eta_H^2}}) [K_{cir}] \right] [\underline{\Phi}] \{\xi\} = [\underline{\Phi}]^T \{f(t)\}
\end{aligned} \tag{94}$$

This form of the equation lends itself to the use the property of orthogonality where:

$$\begin{aligned}
& [\underline{\Phi}]^T ([M_{trans}] + [M_{rot}]) [\underline{\Phi}] = [I], \text{ diagonal} \\
& [\underline{\Phi}]^T (\eta_v [K] - \Omega [G] + [C_e]) [\underline{\Phi}] = [\hat{G}] \\
& [\underline{\Phi}]^T \left[\frac{1 + \eta_H}{\sqrt{1 + \eta_H^2}} [K] + (\eta_v \Omega + \frac{\eta_H}{\sqrt{1 + \eta_H^2}}) [K_{cir}] \right] [\underline{\Phi}] = [\underline{K}]
\end{aligned} \tag{95a,b,c}$$

At this point, a modal reduction technique was used to reduce the number of states in the mass, stiffness, and gyroscopic matrices of equations (95). This eliminated the higher frequency modes outside the speed range of interest.

When the property of orthogonality is used, equation (94) reduces to:

$$\{\ddot{\xi}\} + ([\hat{G}]) \{\dot{\xi}\} + [\underline{K}] \{\xi\} = [\underline{\Phi}]^T [L] \{f(t)\}, \tag{96}$$

where this time, the external damping is not approximated by the damping ratio. Also, note that the new $[\underline{K}]$ matrix does not have the advantage of being diagonal (which complicates the solution).

Again, if one lets \hat{m} forces be applied to the rotor at the appropriate nodal points, the force vector force vector $\{f(t)\}$ in equation (96) must be modified to account for the difference between the number of forces applied, \hat{m} , and the number of modes in the modal matrix, \hat{n} . This inflation is accomplished by the $\hat{n} \times \hat{m}$ matrix $[L]$ where

$$\begin{array}{ccc}
[L] & \{f\} & \longrightarrow [L]\{f\} \\
\hat{n} \times \hat{m} & \hat{m} \times 1 & \hat{n} \times 1
\end{array} \tag{83}$$

To construct the state space model, the equations of motion must be converted to state space coordinates of the form:

$$\{\alpha\} = [\{\xi\}, \{\dot{\xi}\}]^T \quad (84)$$

With this substitution, the equation of motion (96), in matrix notation, becomes:

$$\begin{bmatrix} 0 & I \end{bmatrix} \{\dot{\alpha}\} + \begin{bmatrix} K & \hat{G} \end{bmatrix} \{\alpha\} = [\Phi]^T [L] \{f(t)\} \quad (97)$$

If equation (97) is combined with the identity

$$\begin{bmatrix} I & 0 \end{bmatrix} \{\dot{\alpha}\} + \begin{bmatrix} 0 & -I \end{bmatrix} \{\alpha\} = 0 \quad (85)$$

it gives:

$$\begin{bmatrix} I & 0 \\ 0 & I \end{bmatrix} \{\dot{\alpha}\} + \begin{bmatrix} 0 & -I \\ K & -(\hat{G}) \end{bmatrix} \{\alpha\} = [\Phi]^T [L] \{f(t)\} \quad (98)$$

Now using the standard definitions for state space theory, equation (98) can also be written as

$$\{\dot{\alpha}\} = [A] \{\alpha\} + [B] \{f(t)\} \quad (88)$$

where the state space dynamics matrix [A] is defined as

$$[A] = \begin{bmatrix} 0 & I \\ -K & -(\hat{G}) \end{bmatrix}, 2\hat{n} \times 2\hat{n} \quad (99)$$

and the state space actuator matrix, [B], is defined as

$$[B] = \begin{bmatrix} 0 \\ [\Phi]^T [L] \end{bmatrix}, 2\hat{n} \times \hat{m} \quad (90)$$

To recover the physical displacements of the output at the nodes, state space theory requires that

$$\{q\} = [C] \{\alpha\} \quad (91)$$

If one assumes that displacement sensors where located exactly where the forces where applied, the sensor matrix [C] is defined as:

$$[C] = [\Phi] \quad 0, \hat{m} \times 2\hat{n} \quad (92)$$

Note that the [B] and [C] matrices remain the same if internal damping is added to the system. Only the state space dynamics matrix, [A], is affected.

One final item to discuss is the speed dependence of the [A] matrix for either case (with or without internal damping). This means that a unique [A] matrix exists for every spin speed Ω . To overcome this, a fitting function based on the quadratic Lagrange Polynomial was used in the improved simulation (originally by Scholten) to calculate the individual [A] matrices as the speed varied.

5.3 Magnetic Bearing Simulation Description

After the FEM program calculated the state space matrices, they were placed in a Matlab™ magnetic bearing simulation developed by Draper Laboratory (Scholten) to test the closed loop control of the entire rotor system. It used numerical integration to produce time history plots of rotor displacement in mils, bearing forces in lb, bearing slew rates in lb/s, etc. The numerical integration was performed using a Runge-Kutta method with a variable step size ranging from 1×10^{-8} to 1×10^{-3} seconds.

The original simulation included the state space model for a rotor without internal damping, mathematical models for the bearings, disturbance functions, and rotor imbalance and included appropriate time delays/lags to capture the workings of the entire system. Figure 33 shows a simplified block diagram based on the Simulink™ model (Scholten).

The flux-feedback shown in the figure attempts to compensate for the magnetic materials non-linearities. The flux-feedback, actuator magnetics and power amplifiers are

assumed to work together as a linear actuator, modeled as having force and slew rate limits combined with a low pass frequency response, [18].

Due to the modal reduction technique mentioned in the previous section, the state space matrices used by the simulations only included frequencies up to the first critical speed. By eliminating the higher frequency modes outside the speed range of interest, simulation calculations were completed faster.

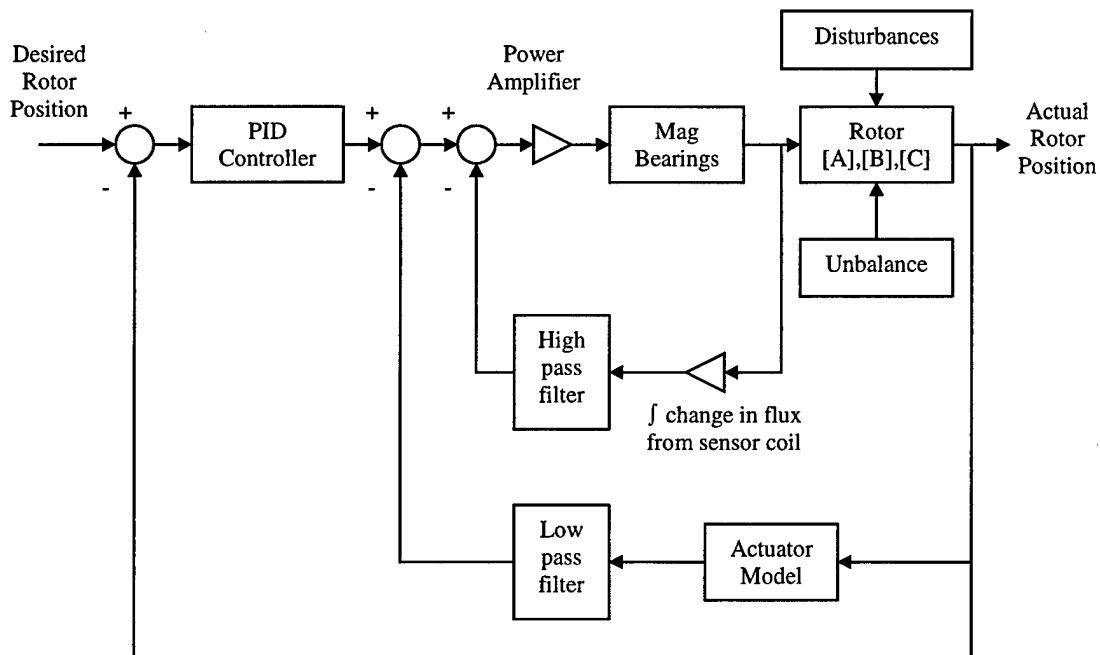


Figure 33: Simplified Block Diagram of Magnetic Bearing Simulation, (Scholten)

5.4 Controller Design

The bearing controllers used for the simulation were designed in the frequency domain using linear Matlab™ based software tools developed at Draper Laboratory. The control system individually controlled each axis on the bearing, or employed a decentralized control strategy. The algorithm used for the controller was classical PID. This included the proportional control for broad band stiffness, the integrator control (with anti-windup) for high load carrying capacity, and derivative control to damp disturbances, [18].

The actual values used for the proportional and derivative constants were extremely important in characterizing the maximum stiffness and damping characteristics of the bearings. The proportional constant, in units of lb/mil, provided the maximum stiffness that the magnetic bearings could provide. The derivative constant, in units of lb-sec/mil, gave the maximum damping that the bearings could provide.

Chapter 6 Modeling and Simulation Predictions and Comparison to Actual Rotor Data – No Internal Damping

In line with its work on magnetic bearings, Draper Laboratory produced a rotor dynamic finite element model (Antkowiak), an accompanying magnetic bearing simulation (Scholten), and a rotor/magnetic bearing testing apparatus. To determine the accuracy of the FEM modeling and the simulation, several test runs were made on the rotor test apparatus. Appendix A details the data acquisition rate and other important information regarding actual rotor testing.

6.1 FEM Modeling

The actual rotor modeled by the original FEM program included a 3/8" diameter, 14.7" long stainless steel shaft, two magnetic actuator rotors and an elastic coupling attached to one end. Figure 34 shows the basic configuration.

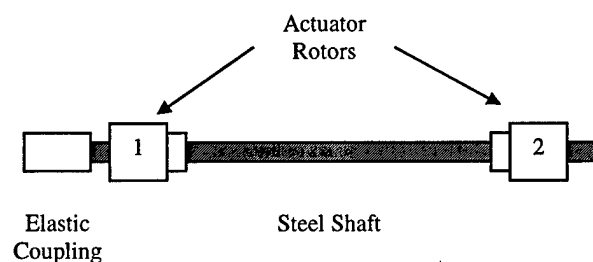


Figure 34: FEM Model of Entire Rotor

The pertinent physical properties of the shaft material included a Modulus of Elasticity of 29.5×10^6 psi, a Poisson's ratio of 0.33, and a density of 7.27×10^{-4} lbf/in³. The shaft was modeled as 20 Timoshenko rotor elements.

As Figure 34 shows, an elastic coupling was necessary to connected the shaft to the drive motor. This elastic coupling was modeled as the first element in the FEM model with a Modulus of Elasticity of 10.0×10^6 psi, a Poisson's ratio of 0.45, and a density of 7.50×10^{-4} lbf/in³, [19].

The two magnetic actuator rotors consisted of a magnetic alloy laminated onto a common aluminum housing secured by a brass nut. Each was modeled geometrically as a stiffened shaft with added mass and gyroscopic inertia. This meant that each of these rotor sections would have the same diameter as the shaft (in the FEM input file), but would have an artificially increased stiffness to compensate for the effects of the larger diameter rotor. This increased bending stiffness was calculated to be 4.69 times that of steel. Due to the interference fit, only half of this value was used to modify the Modulus of Elasticity. This resulted in a Modulus of Elasticity of 69.3×10^6 psi, a Poisson's ratio of 0.33, and a density of 8.40×10^{-4} lbf/in³, for the elastic coupling, [19].

With regard to the additional mass and inertia, Figure 35 shows the locations where they were concentrated along the rotor axial length. In addition, Table 2 shows a summary of the added mass and inertia for the magnetic actuator rotor. The input file for the FEM program describing this rotor is located in Appendix C.

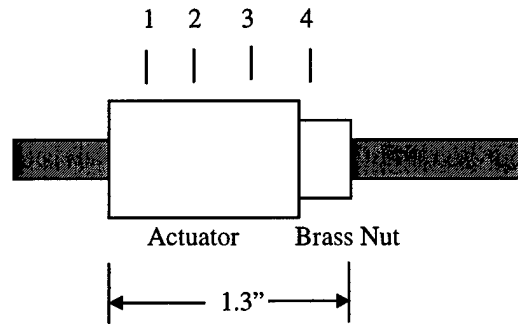


Figure 35: FEM Model of Rotor Actuator

Table 2: Calculations of Added Mass and Inertia Due to Actuator Rotor

Location	1	2	3	4
Axial Length (1.3 in)	0.18	0.43	0.47	0.22
Mass (188 lbm) $\times 10^{-6}$	26.	62.	68.	32.
$I_{yy} \times 10^{-6} \text{ in}^4$	1.2	3.6	4.1	1.5
$I_{xx} \times 10^{-6} \text{ in}^4$	2.2	5.3	5.8	2.7

An important part of the FEM analysis was determining the stiffness and damping characteristics of the bearings. Although magnetic bearings are able to change their stiffness and damping depending on the position of the shaft, the FEM program required constant values for its calculations. In an attempt to model the magnetic bearings, the stiffness and damping was estimated to be 50 lbs/in and 1.5×10^{-2} lbs-sec/in, respectively. These were based upon the maximum stiffness and damping that the controller could provide. More specifically, they were taken directly from the proportional and derivative constants (in units of lb/mil and lb-s/mil, respectively) of the PID controller with the time delays and system lags taken into account.

The rotor free-free natural frequencies are presented in Table 3. The first four modes show the rigid body modes at zero Hertz since both rotor ends are free. (The additional zero frequency modes are present due to the forward and backward components of the state-space model.) These rigid body modes consist of the conical

mode and the cylindrical (or bounce) mode. The last entries in the table are the first three natural frequencies of the non-rotating rotor.

Table 3: Rotor Free-Free Natural Frequencies for $\Omega = 0$

Mode #	Rotor Natural Frequencies (Hz)
1 – 2	0.0
3 – 4	0.0
5 – 6	269.9
7 – 8	790.5
9 – 10	1,559.7

Figure 36 presents the Campbell Diagram for the rotor model. The symmetric bearings have a stiffness and damping of 50 lbs/in and 1.5×10^{-2} lbs-sec/in, respectively. The intersections between the diagonal line (synchronous whirl) and the whirl frequency pairs indicate possible critical speeds. The rigid body modes, the whirl frequency pairs, and the critical speeds for the rotor model are given in Table 4. The critical speed for each mode is in bold text.

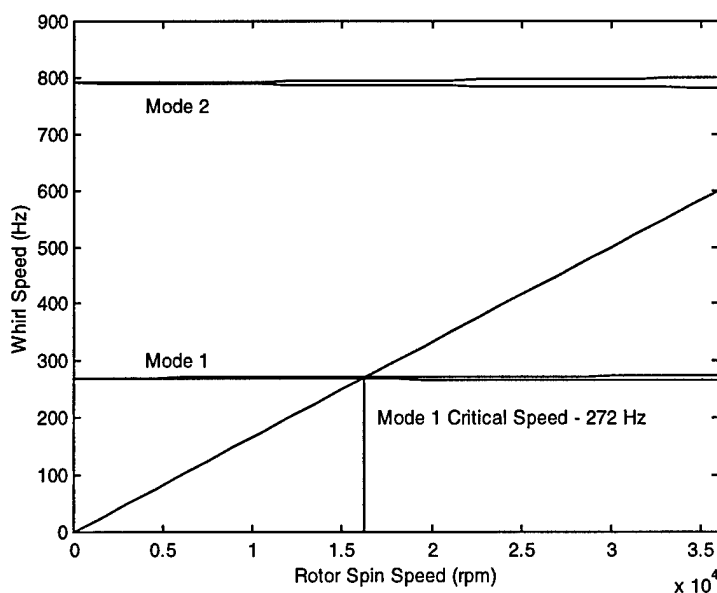


Figure 36: Campbell Diagram for Rotor
Bearing Stiffness = 50 lbs/in, Bearing Damping = 1.5×10^{-2} lbs-sec/in

Table 4: Rotor Whirl Frequency Pairs
Bearing Stiffness = 50 lbs/in, Bearing Damping = 1.5×10^{-2} lbs-sec/in

Mode	Rotor Whirl Frequency Pairs (Hz)	
Rigid Body	42.1, 67.2 ¹	
	Backward	Forward ²
1	268.9	272.5
2	779.7	802.0
3	1,531	1,590

¹ Rigid body modes are uncoupled, ² Rotor Critical Speeds

Note: The original FEM program predicted two rigid body modes (conical and bounce) and gave their uncoupled values. In reality, the two rigid body modes are actually coupled. This coupling typically results in only one noticeable rigid body mode (a combination of both conical and bounce modes), [19].

After the whirl speed analysis was complete, the original FEM program (Antkowiak) generated state space matrices for the rotor model. The bode plot of the free-free rotor model is given in Figure 37. It shows the first critical speed at approximately 1700 rad/sec or 270 Hz, which is consistent with Table 3.

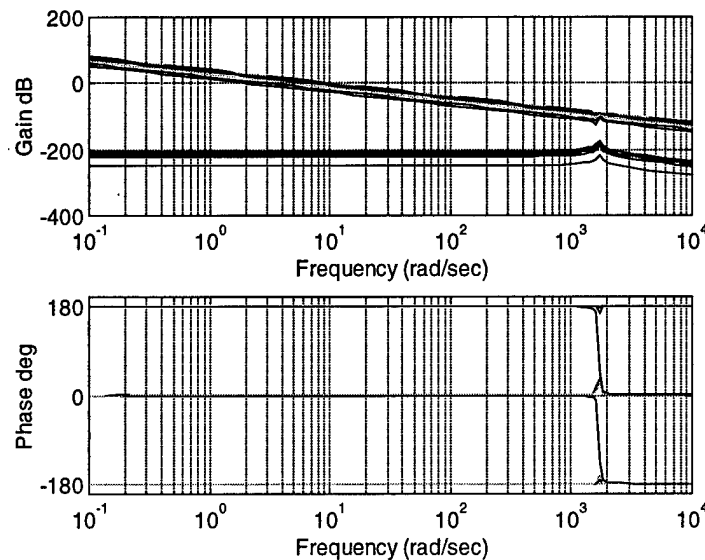
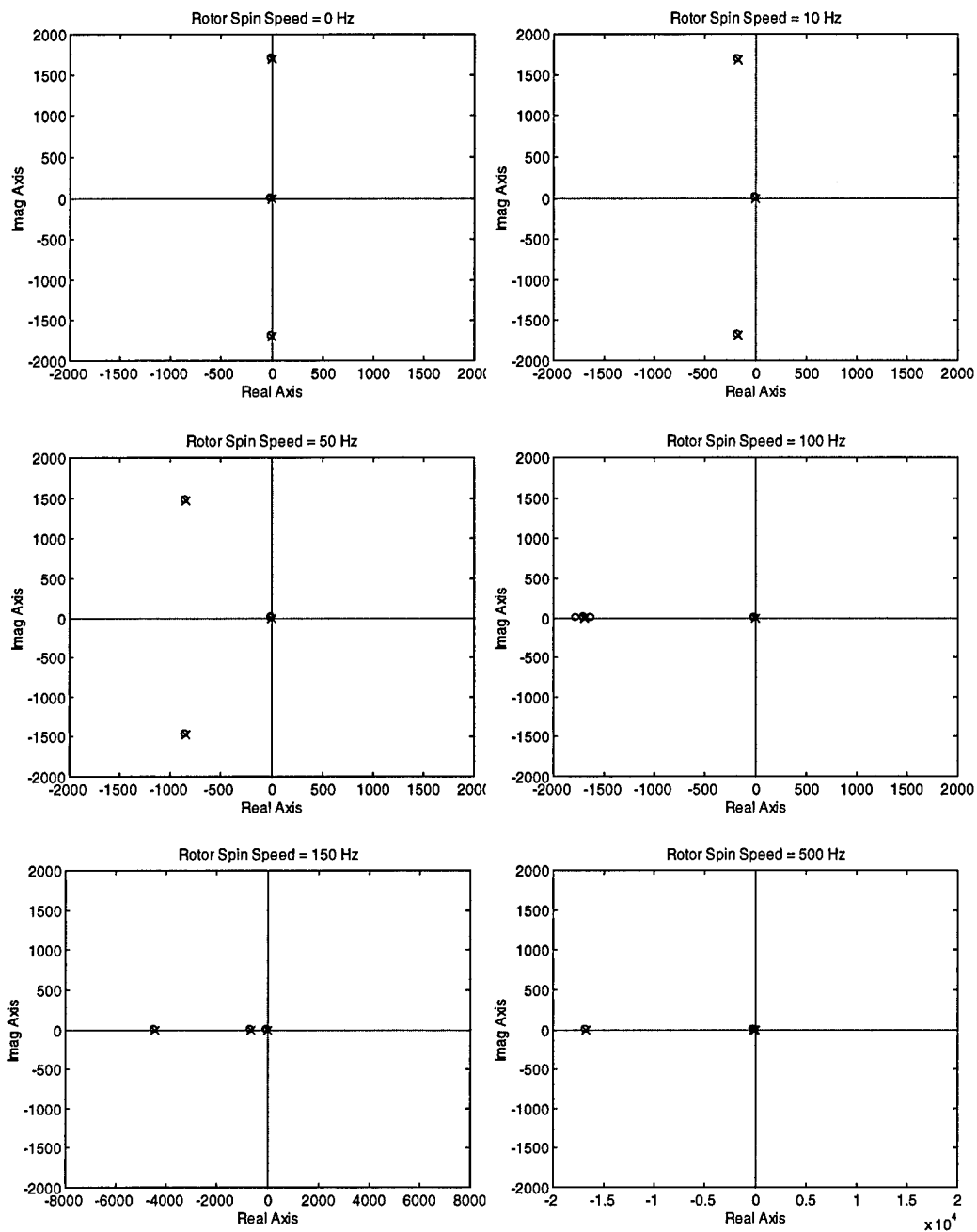


Figure 37: Bode Plot of Free-Free Rotor Model

Prior to entering the rotor model into the simulation, the root loci of the free-free rotor model was plotted. A root locus plot illustrates how the closed loop poles and zeros of a system change as the gain is varied. Although proportional gain is a simple choice for a controller, it gives a quick look at the system stability, gives insight on possible controller designs, and illustrates the complexity of the dynamic model.

Figure 38 shows the how the root loci change as the rotation speed changes. Note that due to the scale of the plots, the root loci lines between the poles (zero gain) and the zeros (infinite gain) are not visible. At zero rotational speed, all of the poles and zeros are located on the imaginary axis. As the rotation speed increases, the poles and zeros move in a curved path toward the negative real axis. Once aligned with the real axis, some begin to migrate towards negative infinity and some approach (but never reach) the origin. Since the poles of this system never cross into the right half plane, the system should be stable for all rotation speeds. In addition, since the zeros of the system never enter the right half-plane, it indicates that a simple controller might be sufficient to control the system, [20].



**Figure 38: Root Loci of Free-Free Rotor Model as Rotation Speed Increases
(No Internal or External Damping)**

6.2 Magnetic Bearing Simulation Results

Using the calculated state-space matrices from the original FEM model (Antkowiak), the magnetic bearing simulation (Scholten) predicted the critical speeds and rigid body modes for the rotor. Figure 39 shows the simulated response of the rotor to a 0 to 325 Hz ramp in one second. The top time history plot shows the displacement of the rotor at bearing one (located next to the elastic coupling) in both the vertical and horizontal axes. The second time history shows the displacement of the rotor at bearing two. Underneath the time histories, additional plots are provided to show the radial shaft orbit during the simulated test run. The dashed lines in the orbit plots represent the touchdown bearings (8 mil air gap). In general, the results of Figure 39 indicate that the PID controller can successfully control the rotor as it passes through the first critical speed (occurring at approximately 0.92 seconds or 290 Hz) without contacting the touchdown bearings. This also confirms the assumption based on the root loci plots (Figure 38) that a simple controller would be sufficient to control this system.

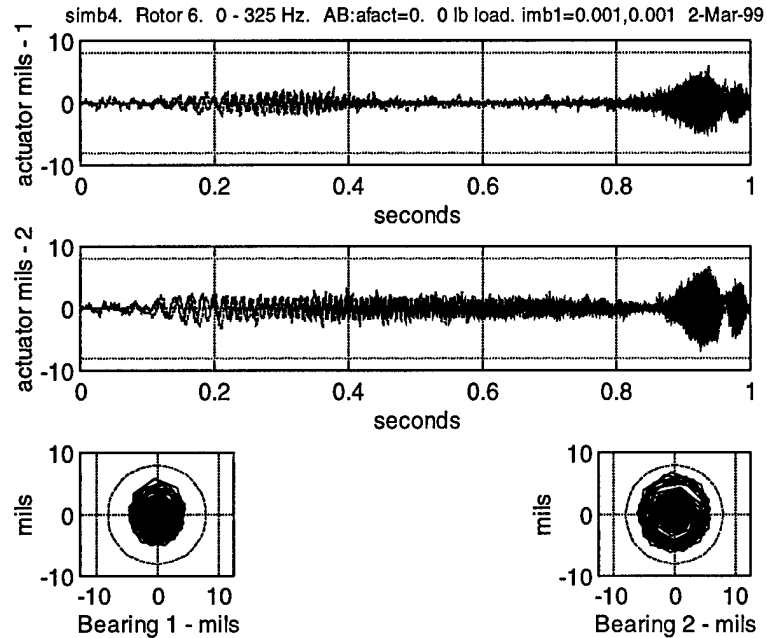


Figure 39: Simulation Prediction of Rotor Response during a 0 – 325 Hz Ramp

To get a better insight on the closed loop control of the plant, a number of plots were generated using frequency domain based tools developed at Draper Laboratory. Figure 40 shows the frequency response of the rotor located at bearing number two (farthest away from the elastic coupling) in terms of magnitude (output/input ratio in dB) and phase (output – input in degrees) for a rotor speed of 150 Hz. This spin speed was chosen as a representative operating speed for the rotor due to motor speed limitations. The first response, A, shown is the plant model. For this case, the plant includes bearing one represented by a first order lag model. The second response, B, shows the controller response, which includes calculation and zero-order-hold delays. The final pair of plots, C, shows the open loop (without feedback) response of the plant and the controller combined. Phase is positive from approximately 40 to 300 Hz indicating the frequency band where damping occurs, [22].

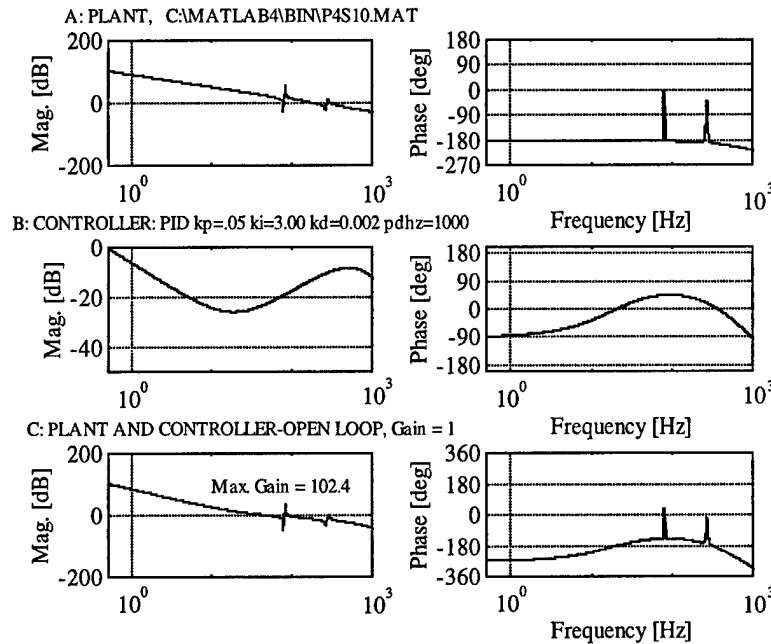


Figure 40: (A) Plant Response, (B) Controller Response, (C) Plant and Controller Combined (Open-Loop) Response for a Rotor Spin Speed of 150 Hz

Figure 41 is a Nichols plot of the magnitude versus the phase from the open-loop plant and controller combined case shown in Figure 40. The rotor speed is 150 Hz. The 'X' indicates the operating point of the control law relative to the complex structure of the rotordynamics. The distance of the 'X' from the line gives the gain margin as 15 dB and the phase margin as 30 degrees. These adequate margins indicate that the controller will be reliably stable, with a damped response to disturbances, [21].

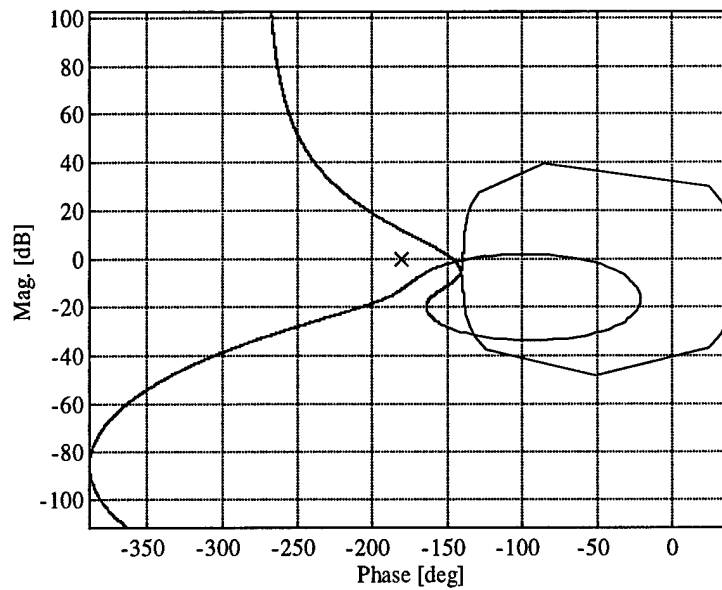


Figure 41: Open Loop Gain vs. Phase at 150 Hz

Figure 42 presents the open and closed loop frequency response of the controlled bearing furthest away from the motor (bearing 2). The dashed line corresponds to the uncontrolled rotor (combined plant and controller response of Figures 40 and 41) and the solid line shows the controlled rotor. The difference between the two represents the action of the magnetic bearings upon the rotor. At lower frequencies the effect is large because the bearings can tightly constrain the rotor. At high frequencies the effect is minimal due to the inherent difficulty of moving the rotor since the displacement is proportional to force/frequency², [21]. In addition, these higher frequencies are beyond the actuator bandwidth. The critical speed for the closed loop system shown in this figure is 289 Hz, which is close to the value estimated from Figure 39.

Plant and Controller Combined Open/Closed-Loop FRF: [PID kp=.05 ki=3.00 kd=0.002 pdhz=1000] Gain = 1

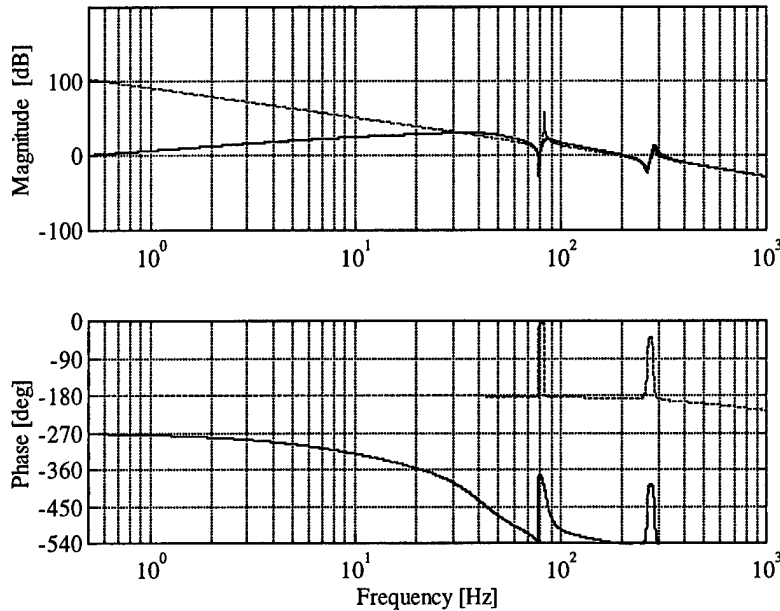


Figure 42: Open and Closed Loop Frequency Response, 150 Hz

To find the rigid body modes predicted by the simulation, a Power Spectral Density plot of the rotor system, at a constant speed of 148 Hz, was produced. Similar to a Bode plot, a PSD takes all of the modes acting on the system and plots them as a function of frequency. Figure 43 shows the dominant mode of 148 Hz (related to the rotor spin speed) and a small peak occurring at 289 Hz (critical speed). Although there is not a distinct peak, the relative maximum of the curve gives a rigid body mode estimate of 47 Hz. A comparison of the FEM model predictions to the closed loop simulation is given in Table 5.

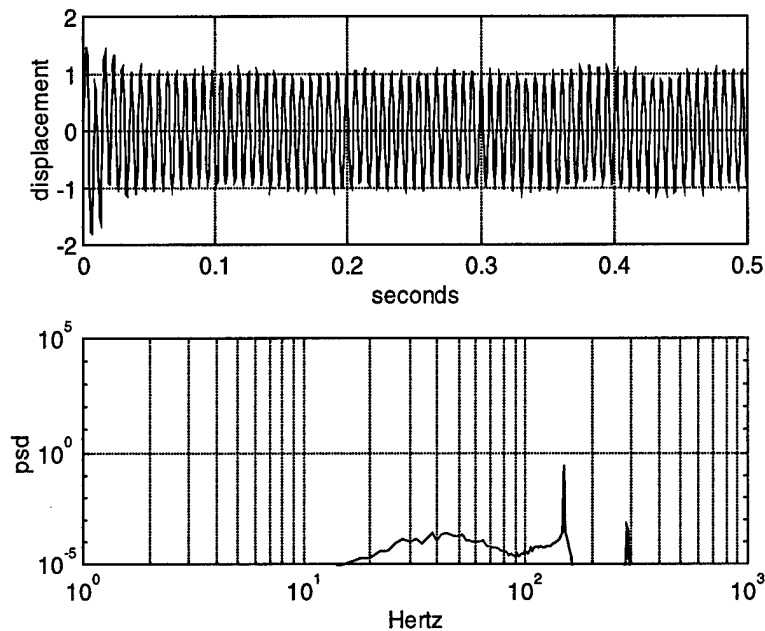


Figure 43: PSD of Simulation at Constant Rotor Spin Speed of 148 Hz

Table 5: Comparison of Original FEM Model to Original Simulation
FEM Model: Bearing Stiffness = 50 lbs/in, Bearing Damping = 1.5×10^{-2} lbs-sec/in
Simulation: $K_p = 0.05$ lb/mil, $K_I = 3.00$ lb/mil-s, $K_D = 0.002$ lb-sec/mil,
Derivative Bandwidth = 1000 Hz

Mode	FEM Prediction	Simulation
Rigid Body Mode	42.1, 67.2*	47
1 st Critical Speed	272.5	289

* Rigid body modes are uncoupled.

6.3 Actual Rotor Testing and Comparison to Simulation

To determine the accuracy of the FEM model and the Matlab™ magnetic bearing simulation, several test runs were made on a rotor test apparatus located at Draper Laboratory. Appendix A details the data acquisition rate and other important information regarding actual rotor testing.

Figures 44 and 45 show two representative simulation predictions compared to actual rotor rig test data. For each pair of plots, the simulation predictions are located on the left and the actual rotor test runs are shown on the right. All cases were run at a constant rotation speed and all displacements were measured in mils from the bearing centerline. Figures 44 and 45 show good agreement in terms of the predicted and actual displacements for bearing number 2, although the simulation predicted somewhat lower displacements for the bearing near the elastic coupling. This suggests that more work needs to be done on the elastic coupling block of the simulation. In terms of the vertical displacements at the bearings, the simulation had good correlation to the actual rotor data, while the predicted horizontal displacements were slightly smaller than the actual rotor data.

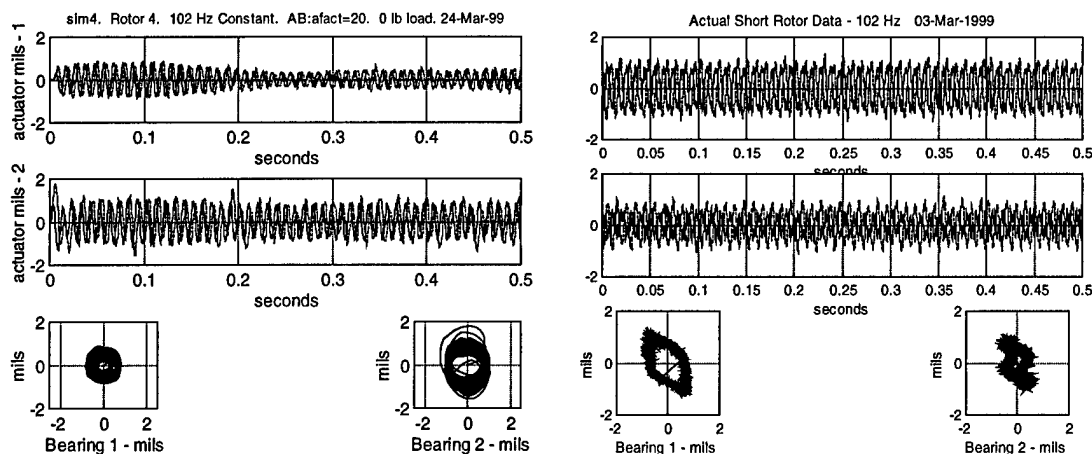


Figure 44: Predicted and Actual Rotor Displacements, 102 Hz

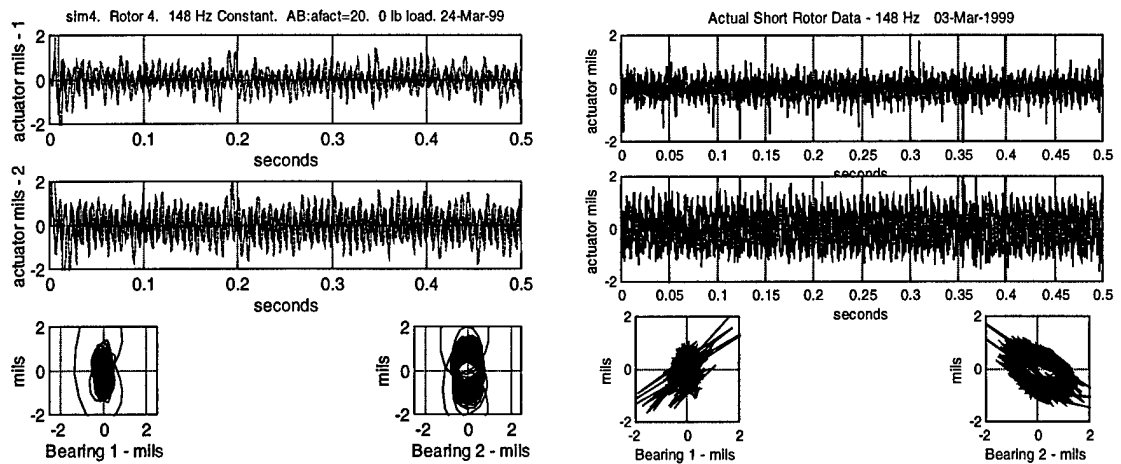


Figure 45: Predicted and Actual Rotor Displacements, 148 Hz

The only area where the simulation had poor accuracy with regard to the actual rotor displacements was in the speed range near the rigid body mode. Since the simulation predicted the rigid body mode at 47 Hz, its displacement predictions at the actual rigid body mode of 52 Hz would not be as large. This is shown in Figure 46 with the simulation prediction on the left and the actual rotor data on the right.

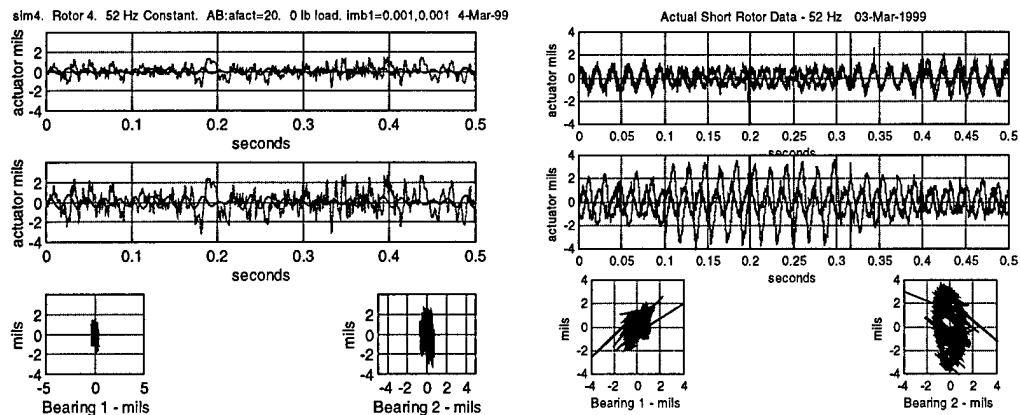


Figure 46: Predicted and Actual Rotor Displacements, 52 Hz

A more important measure of the simulation was its ability to predict the location of the rigid body modes and the critical speeds. With regard to the first critical speed, the actual rotor could not be subjected to a ramp from 0 to 325 Hz in one second (like the simulation). In addition, hardware limitations prevented the rotor from achieving speeds greater than 200 Hz. Therefore, to determine the first critical speed and get another estimate of the rigid body mode, a PSD plot was made from actual rotor data at 148 Hz. Figure 47 shows the dominate mode of 148 Hz (related to the rotor spin speed), a peak at 52 Hz (rigid body mode) and a small peak occurring at 295 Hz (critical speed).

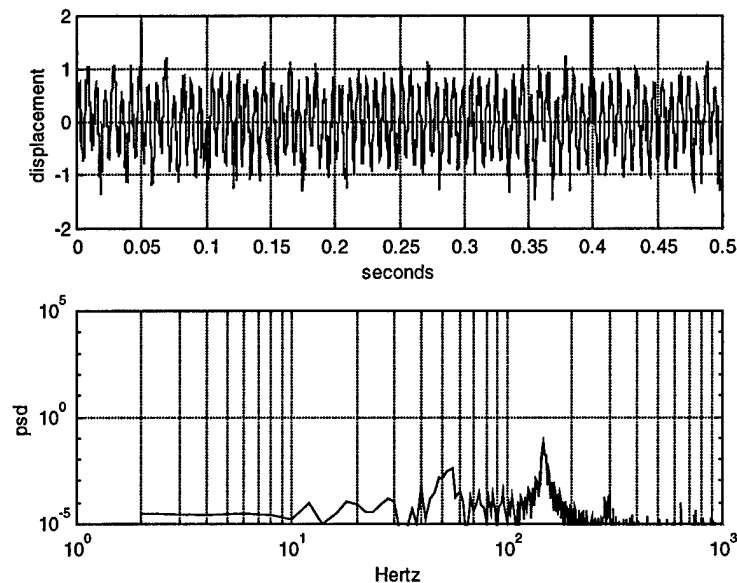


Figure 47: PSD of Actual Rotor at Constant Rotor Spin Speed of 148 Hz

Table 6 presents a summary of the results for the FEM rotor model, the simulation, and the actual rotor data. The FEM critical speed prediction was slightly lower than the actual rotor rig critical speed. This was probably due to the simplicity of the FEM model. This model did not take into account rotor unbalance, it assumed that the bearing and properties were constant, and it did not model any other overall system effects such as magnetic bearing material non-linearity, actuator lag, etc. (Note: Since the

FEM produced uncoupled rigid body modes, they could not be directly compared to the actual rotor rig data.)

Table 6: Comparison of Original FEM, Modified Simulation and Actual Rotor Rig Data, FEM Model: Bearing Stiffness = 50 lbs/in, Bearing Damping = 1.5×10^{-2} lbs-sec/in, Simulation: $K_P = 0.05$ lb/mil, $K_I = 3.00$ lb/mil-s, $K_D = 0.002$ lb-sec/mil, Derivative Bandwidth = 1000 Hz

Mode	FEM Prediction	Simulation Prediction	Actual Rotor Rig Data
Rigid Body Mode	42.1, 67.2	47	52
1 st Critical Speed	272.5	289	295*

* Indicates condition not tested.

In contrast to the simple FEM, the high fidelity simulation (originally by Scholten with slight modifications described in Chapter 5) predicted a first critical speed that closely matched the actual rotor test data, although the rigid body mode predictions were not as accurate. With regard to the displacements predicted by the simulation, good agreement was seen in terms of the predicted and actual displacements for bearing number 2, although the modified simulation predicted somewhat lower displacements for the bearing near the elastic coupling. This suggests that more work needs to be done on the elastic coupling block of the simulation. In terms of the vertical displacements at the bearings, the modified simulation had good correlation to the actual rotor data, while the predicted horizontal displacements were slightly smaller than the actual rotor data. The only area where the simulation had poor accuracy with regard to the actual rotor displacements was in the speed range near the rigid body mode. Since the simulation predicted the rigid body mode at 47 Hz, its displacement predictions at the actual rigid body mode of 52 Hz would not be as large.

Chapter 7 Modeling and Simulation Predictions for a Rotor with Internal Damping

7.1 FEM Modeling

The same rotor at Draper Laboratory was again modeled using the extended FEM program. But for these cases, a number of different combinations of internal damping was included in the rotor. First, internal viscous damping ($\eta_V = 2 \times 10^{-6}$) was included. Next, only internal hysteretic damping ($\eta_H = 2 \times 10^{-4}$) was included in the rotor. Finally, both internal hysteretic and viscous damping were added to the rotor.

The actual amounts of internal damping that were included in the rotor were estimated based on references, [2, 10, and 11]. Even though the actual amount of internal damping in the rotor remains unknown, these estimated values are still useful to show how the simulation (Scholten) and controller would react to the destabilizing effects of internal damping in general.

An important part of the FEM analysis was determining the stiffness and damping characteristics of the bearings. Although magnetic bearings were able to change their stiffness and damping depending on the position of the shaft, the FEM program required constant values for its calculations. In an attempt to model the bearings, the stiffness and damping was assumed to be 50 lbs/in and 1.5×10^{-2} lbs-sec/in respectively. These were based upon the maximum stiffness and damping that the controller could provide. More specifically, they were taken directly from the proportional and derivative constants of the PID controller (in units of lb/mil and lb-s/mil, respectively) with the time delays and system lags taken into account. The FEM calculated whirl frequency pairs and estimates

of the instability thresholds for the various combination of internal damping are given in Table 7. The critical speed for the first mode is in bold text.

Table 7: FEM Predicted Rotor Instability Thresholds
Bearing Stiffness = 50 lbs/in, Bearing Damping = 1.5×10^{-2} lbs-sec/in

Internal Damping	FEM Whirl Frequencies (Hz)		Instability Threshold (Hz)
	Backward	Forward	
$\eta_V = 2 \times 10^{-6}$	268.9	272.5*	441
$\eta_H = 2 \times 10^{-4}$	268.9	272.5*	Stable for all Speeds
$\eta_V = 2 \times 10^{-6}, \eta_H = 2 \times 10^{-4}$	268.9	272.5*	425

* Critical speed

After the whirl speed analysis was complete, the FEM program generated state space matrices for the three rotor models. The bode plots of the free-free rotor models (without external damping or stiffness) are given in Figures 48-50. All plots show the same values for the first critical speed at approximately 1700 rad/sec or 270 Hz, which is consistent with Table 7. In addition, all plots show the erratic tendencies of the phase as the frequency is increased. This could be a result of adding internal damping to the system, and needs further investigation.

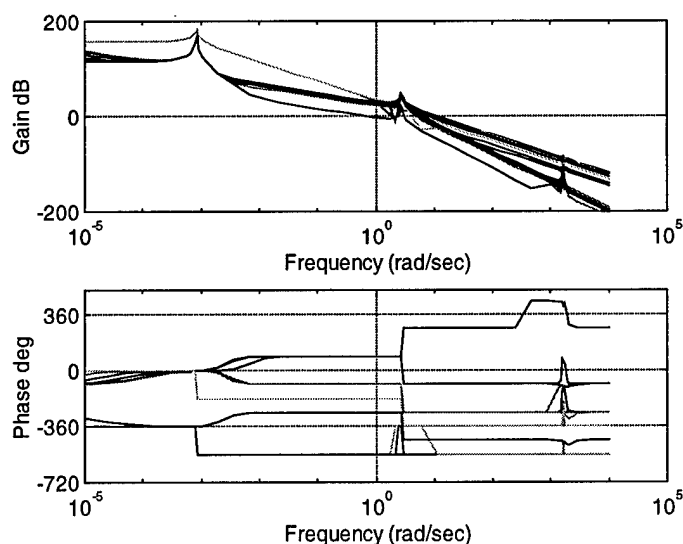


Figure 48: Bode Plot of Free-Free Rotor Model at 250 Hz
with Internal Viscous Damping $\eta_V = 2 \times 10^{-6}$

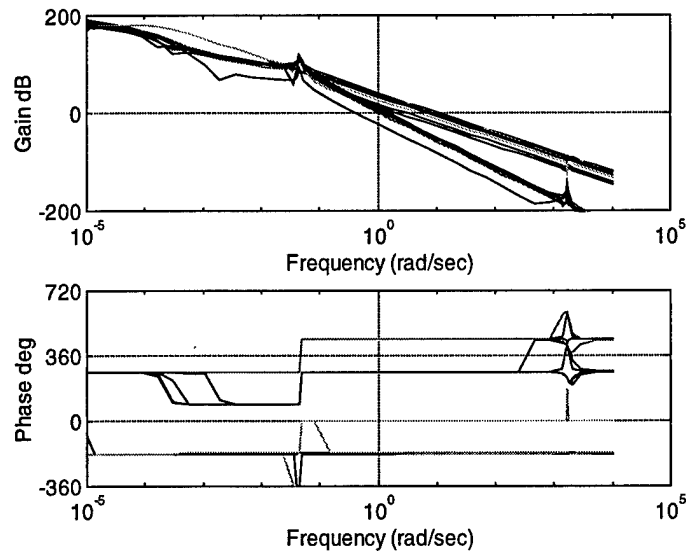


Figure 49: Bode Plot of Free-Free Rotor Model at 250 Hz with Internal Hysteretic Damping $\eta_H = 2 \times 10^{-4}$

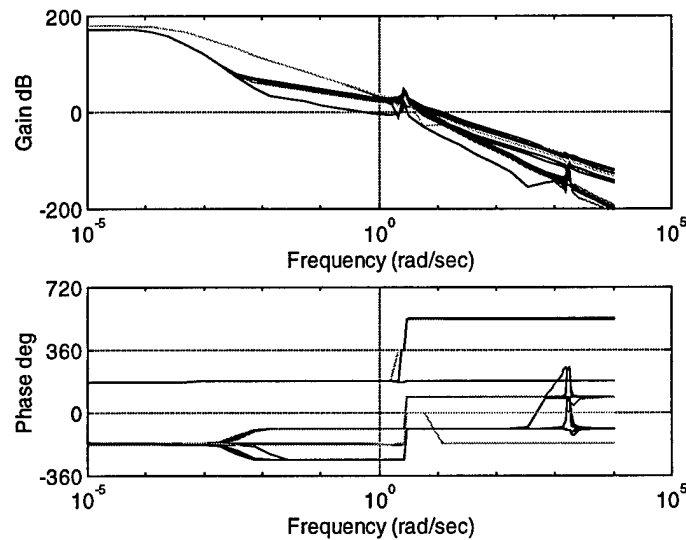


Figure 50: Bode Plot of Free-Free Rotor Model at 250 Hz, with Internal Viscous Damping $\eta_V = 2 \times 10^{-6}$, Internal Hysteretic Damping $\eta_H = 2 \times 10^{-4}$

Prior to entering the rotor model, into the modified simulation, the root loci of the free-free rotor models were plotted. Figure 51 shows the how the root loci of the rotor with internal viscous damping change as the rotation speed changes. At zero rotational speed, a few poles and zeros are located at the origin, with the rest in the stable left half plane. As the rotation speed increases, the two pairs of poles and zeros begin to migrate toward the imaginary axes. Between 250 and 300 Hz the pairs actually cross over into

the unstable region. This crossover occurs at the critical speed of the free-free rotor. This is consistent with the general characteristics of internal viscous damping (see the discussion in Chapter 3). Since the poles and zeros of this rotor do cross over into the right half plane, this indicates that a rotor with internal viscous damping might be difficult to control at speeds above its critical speed, [20].

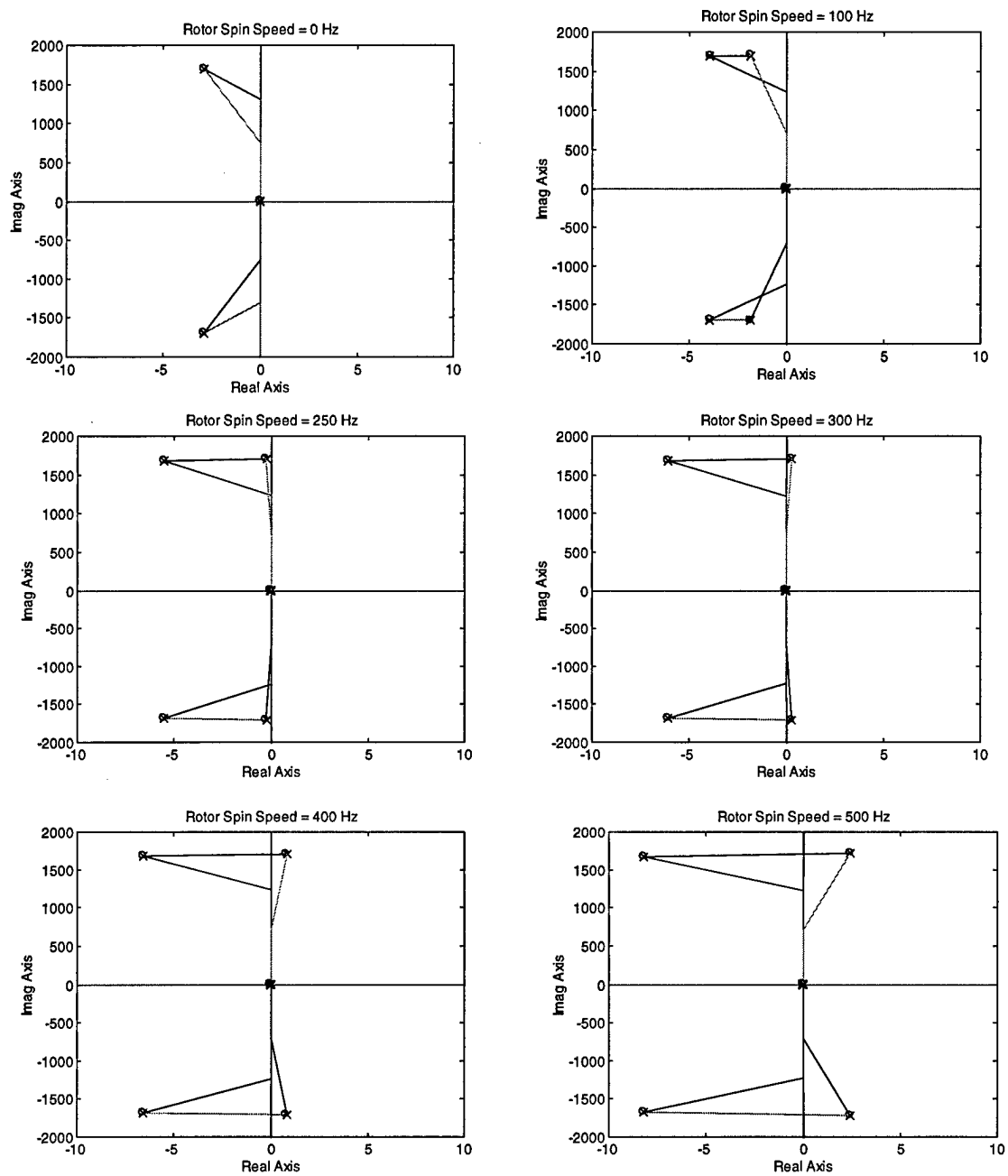


Figure 51: Root Loci of Free-Free Rotor Model as Rotation Speed Increases (Internal Viscous Damping $\eta_v = 2 \times 10^{-6}$)

Figure 52 shows the how the root loci of the rotor with internal hysteretic damping change as the rotation speed changes. For all rotational speeds, a pair of poles is located in the left and right half planes. This indicates that the free-free rotor will be

unstable for all speeds. These results are consistent with the general characteristics of internal hysteretic damping (see the discussion in Chapter 3). As the rotation speed increases, the two pairs of zeros begin to migrate toward the poles. Since this system has poles and zeros located in the right half plane, this indicates that a rotor with internal hysteretic damping might be difficult to control at all speeds, [20].

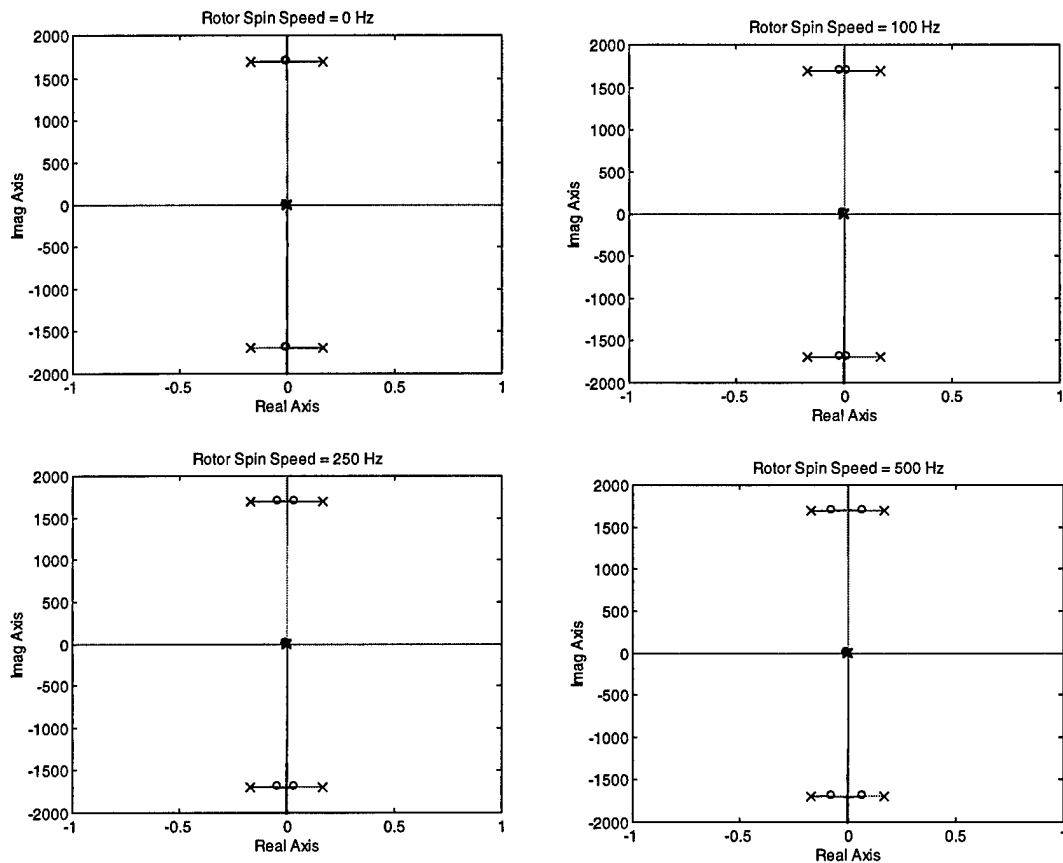


Figure 52: Root Loci of Free-Free Rotor Model as Rotation Speed Increases (Internal Hysteretic Damping $\eta_H = 2 \times 10^{-4}$)

Figure 53 shows the how the root loci of the rotor with internal viscous and hysteretic damping change as the rotation speed changes. In general, the trend is very similar to Figure 51 (internal viscous damping only), where the poles and zeros migrate toward and cross into the unstable region. The difference lies in that the system can be

unstable at all speeds depending on the value of the gain. This is most apparent in the top left-hand corner of Figure 53 (rotor spin speed of 1 Hz). Similar to the internal viscous damping only case, these results indicate that a rotor with both internal viscous and hysteretic damping might also be difficult to control at speeds above its critical speed, [20].

Although it may appear odd that this free-free rotor (without external damping) can be stable even though it has internal hysteretic damping, one must recall the importance Figure 16 from Chapter 3 or the stabilizing term, $\eta_v[K]\{\dot{q}\}$, from equation (72). The figure shows that the particular direction of the internal viscous damping force depends on the sign of the $(\Omega - \omega)$. For this particular rotor, the internal hysteretic damping was in the same direction as the rotor whirl and the internal viscous damping was in the opposite direction. So, for speeds below the critical speed of the system, the stabilizing effects of internal viscous damping counteracted the destabilizing effects of the internal hysteretic damping.

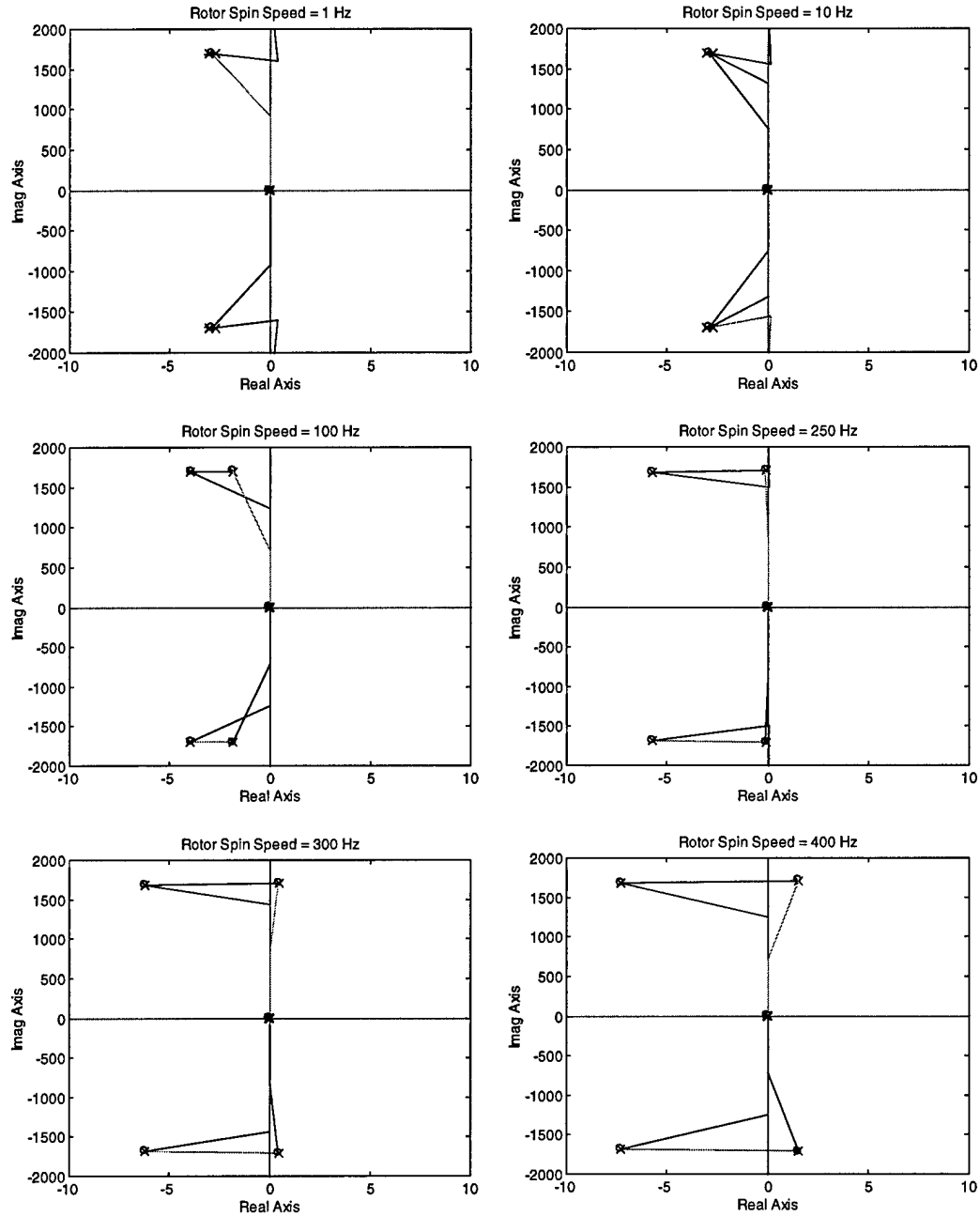


Figure 53: Root Loci of Free-Free Rotor Model as Rotation Speed Increases
 (Internal Viscous Damping $\eta_V = 2 \times 10^{-6}$, Internal Hysteretic Damping $\eta_H = 2 \times 10^{-4}$)

7.2 Magnetic Bearing Simulation Predictions (Internal Damping Included)

Using the calculated state-space matrices from the extended FEM model, the simulation attempted to predict the instability thresholds for the various combinations of internal damping. Figure 54 shows the simulated response of the rotor with internal viscous damping during a 0 to 400 Hz ramp in one second. At the closed-loop system's critical speed of 289 Hz (approximately 0.72 seconds) the rotor becomes unstable. This instability threshold is well below the FEM predicted speed of 441 Hz found in Table 7.

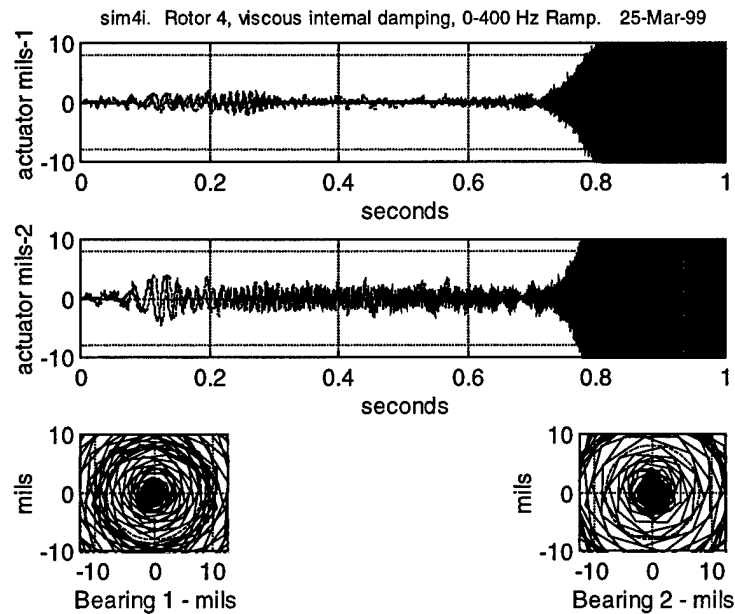


Figure 54: Simulation Prediction of Rotor Response during a 0 – 400 Hz Ramp, Internal Viscous Damping $\eta_v = 2 \times 10^{-6}$

To get a better insight on the closed loop control of the plant, a number of plots were generated using frequency domain based tools developed at Draper Laboratory. Figure 55 shows the frequency response of the rotor located at bearing number two in terms of magnitude (output/input ratio in dB) and phase (output – input in degrees) for a

rotor speed of 250 Hz. The first response, A, shown is the plant model. For this case, the plant includes bearing one represented by a first order lag model. The second response, B, shows the controller response. The final pair of plots, C, shows the open loop (without feedback) response of the plant and the controller combined. Similar to the bode plot in Figure 48, note the sudden phase angle changes for both the plant and for the combined open loop plant and controller.

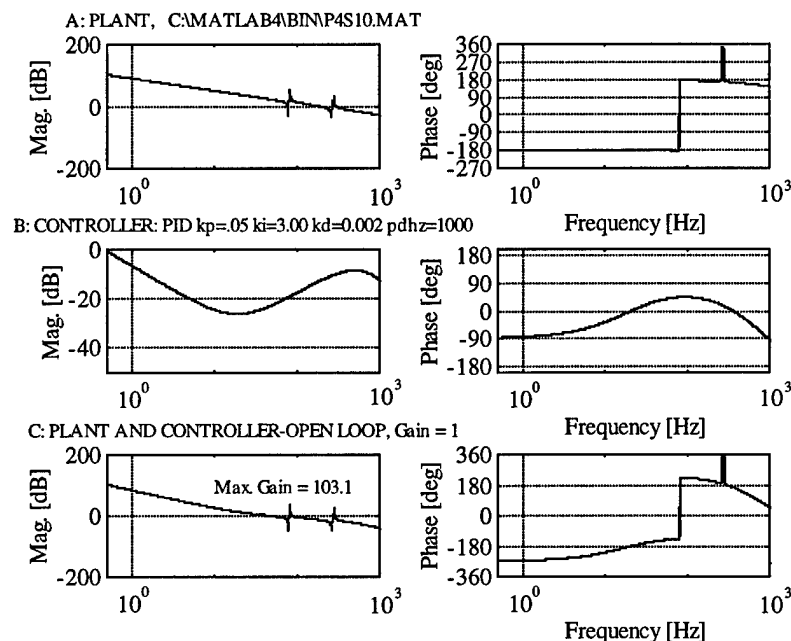
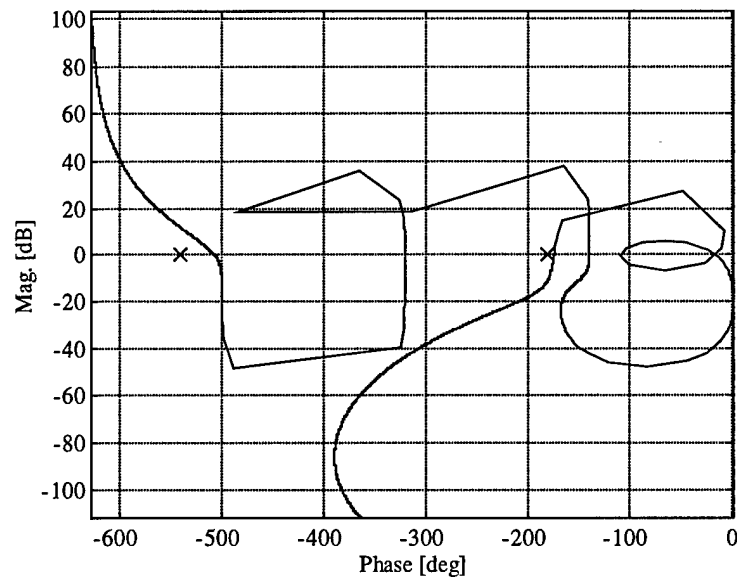


Figure 55: (A) Plant Response, (B) Controller Response, (C) Plant and Controller Combined (Open-Loop) Response for a Rotor Spin Speed of 250 Hz, Internal Viscous Damping $\eta_v = 2 \times 10^{-6}$

A number of different PID controllers were tested in an attempt to stabilize the rotor above its critical speed. These efforts focused on controller design in the frequency domain with subsequent testing in the full simulation. Increasing (or decreasing) the proportional, integral, and derivative constants had little effect on the stability of the system.

In a sense, the PID controller was “boxed in” by the complex rotordynamics. This is shown best by the Nichols plot in Figure 56. The smallest gain and phase margins for the controller are 11 dB and 5 degrees. Although the open loop system is stable at this spin speed (250 Hz), these margins will decrease even further as the rotor spin speed increases, leading to instability.



**Figure 56: Open Loop Gain vs. Phase at 250 Hz,
Internal Viscous Damping $\eta_v = 2 \times 10^{-6}$**

Figure 57 presents the open and closed loop frequency response of the controlled bearing furthest away from the motor. The dashed line corresponds to the uncontrolled rotor (open loop plant and controller response combined from Figures 55 and 56) and the solid line shows the controlled rotor. The difference between the two represents the action of the magnetic bearings upon the rotor. Again, note the sudden phase angle changes.

Plant and Controller Combined Open/Closed-Loop FRF: [PID kp=.05 ki=3.00 kd=0.002 pdhz=1000] Gain = 1

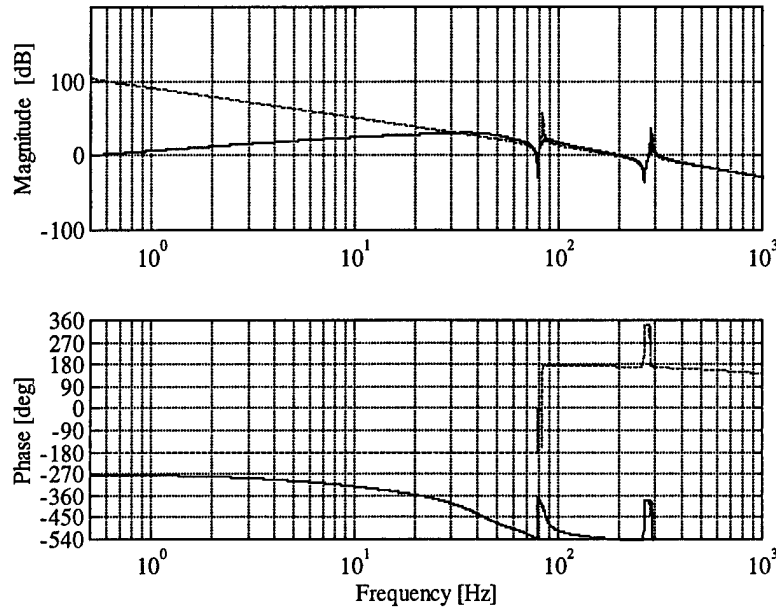


**Figure 57: Open and Closed Loop Frequency Response at 250 Hz,
Internal Viscous Damping $\eta_v = 2 \times 10^{-6}$**

Based on the results from Figures 54-57, and based on the earlier results of the root loci plots (Figure 51) it appears that a PID controller is not sufficient to control a rotor with internal viscous damping above its critical speed.

If only internal hysteretic damping was included in the shaft, the simulation remained stable for all spin speeds tested. Figure 58 shows the simulated response of the rotor during a 0 to 400 Hz ramp in one second. This figure agrees with the FEM results (Table 7) and also is consistent with the characteristics of a system with internal hysteretic damping. In this case, it appears that the external damping provided by the magnetic bearings was sufficient to overcome the amount of internal hysteretic damping in this speed range.

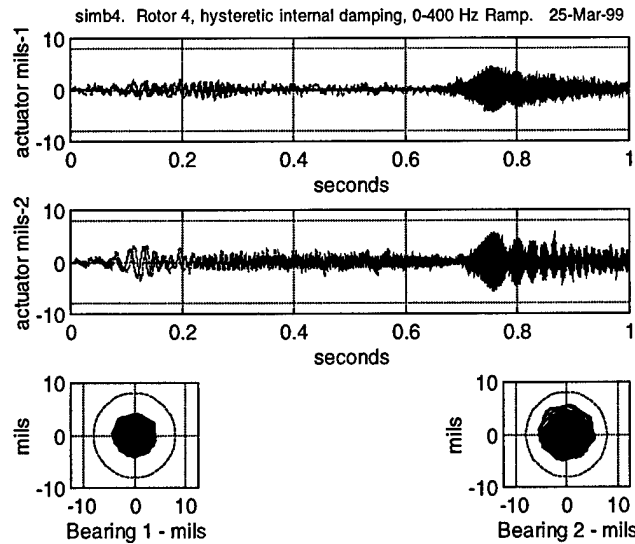


Figure 58: Simulation Prediction of Rotor Response during a 0 – 400 Hz Ramp
Internal Hysteretic Damping $\eta_H = 2 \times 10^{-4}$

Figure 59 shows the frequency response of the rotor located at bearing number two in terms of magnitude and phase for a rotor speed of 250 Hz. The first response shown is the plant. The second plots show the controller response while the final plots shows the plant and controller combined response.

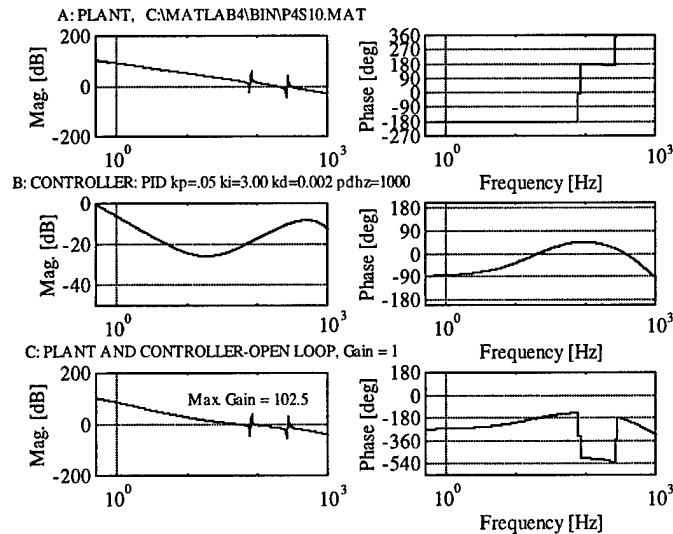
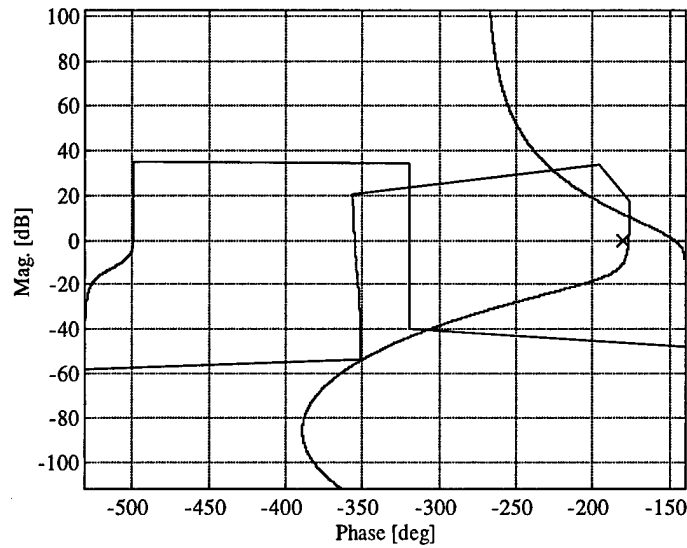


Figure 59: (A) Plant Response, (B) Controller Response, (C) Plant and Controller Combined (Open-Loop) Response for a Rotor Spin Speed of 250 Hz
Internal Hysteretic Damping $\eta_H = 2 \times 10^{-4}$

Figure 60 plots the magnitude versus phase from the open loop plant and controller combined case shown in Figure 59. This plot indicates that the combined open loop system is unstable at this speed, and is consistent with the root loci plots in Figure 52.



**Figure 60: Open Loop Gain vs. Phase at 250 Hz,
Internal Hysteretic Damping $\eta_H = 2 \times 10^{-4}$**

Figure 61 presents the open and closed loop frequency response of the controlled bearing furthest away from the motor. The dashed line corresponds to the uncontrolled rotor (open loop plant and controller response combined from Figures 59 and 60) and the solid line shows the controlled rotor.

Plant and Controller Combined Open/Closed-Loop FRF: [PID kp=.05 ki=3.00 kd=0.002 pdhz=1000] Gain = 1

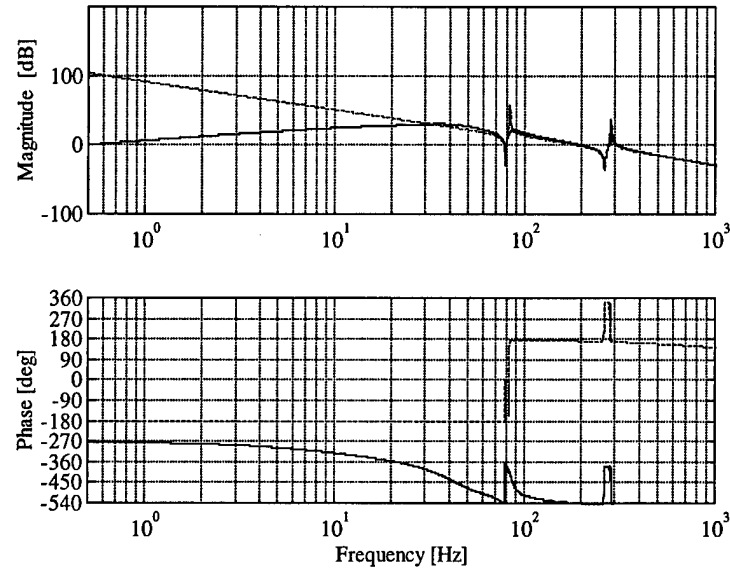


**Figure 61: Open and Closed Loop Frequency Response at 250 Hz,
Internal Hysteretic Damping $\eta_H = 2 \times 10^{-4}$**

Although the results from Figures 58-61 indicate that a PID controller can maintain stability for the speed range tested, in reality the inherent limitations of a PID controller will eventually cause the rotor to become unstable. Eventually as the speed increases, the PID controller will have to lower its gain (including lowering the amount of external damping applied to the system). During this “roll off” period, the amount of external damping will fall below the amount of internal hysteretic damping and will cause the rotor to become unstable, [21].

When internal viscous and hysteretic damping was added to the shaft, the simulation predicted that the rotor would be stable below its closed loop critical speed of 289 Hz. Similar to the internal viscous damping case, this instability threshold is well below the FEM predicted speed of 422 Hz found in Table 7. Figure 62 shows the simulated response of the rotor during a 0 to 400 Hz ramp in one second.

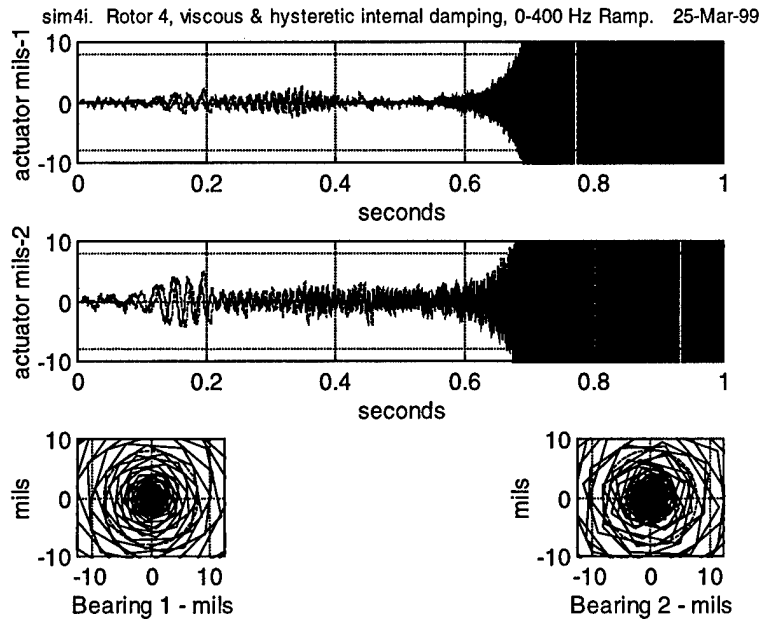


Figure 62: Simulation Prediction of Rotor Response during a 0 – 400 Hz Ramp, Internal Viscous Damping $\eta_V = 2 \times 10^{-6}$, Internal Hysteretic Damping $\eta_H = 2 \times 10^{-4}$

Figure 63 shows the frequency response of the rotor located at bearing number two in terms of magnitude and phase for a rotor speed of 250 Hz. The first response shown is the plant. The second pair of plots show the controller response while the final pair show the plant and controller combined response. Note the similarities in the phase angle to Figure 55 (internal viscous damping only).

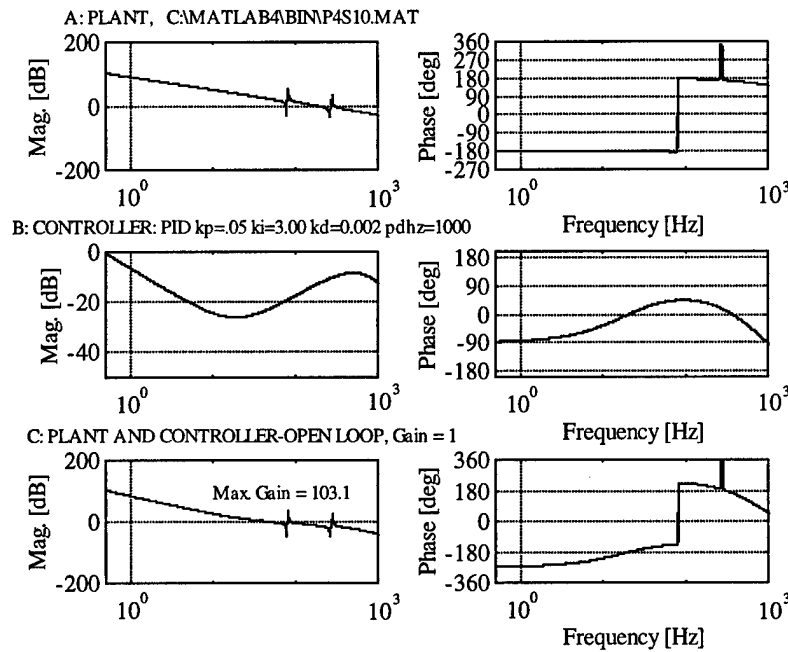


Figure 63: (A) Plant Response, (B) Controller Response, (C) Plant and Controller Combined (Open-Loop) Response for a Rotor Spin Speed of 250 Hz, Internal Hysteretic Damping $\eta_H = 2 \times 10^{-4}$, Internal Viscous Damping $\eta_V = 2 \times 10^{-6}$

Again, a number of different PID controllers were tested in an attempt to stabilize the rotor above its critical speed. Increasing (or decreasing) the proportional, integral, and derivative constants had little effect on the stability of the system. The Nichols plot in Figure 64 shows how the PID controller was limited by the complex rotordynamics. The gain and phase margins for the controller are 11 dB and 5 degrees. Although the open loop system is stable at this spin speed (250 Hz), these margins will decrease even further as the rotor spin speed increases, leading to instability.

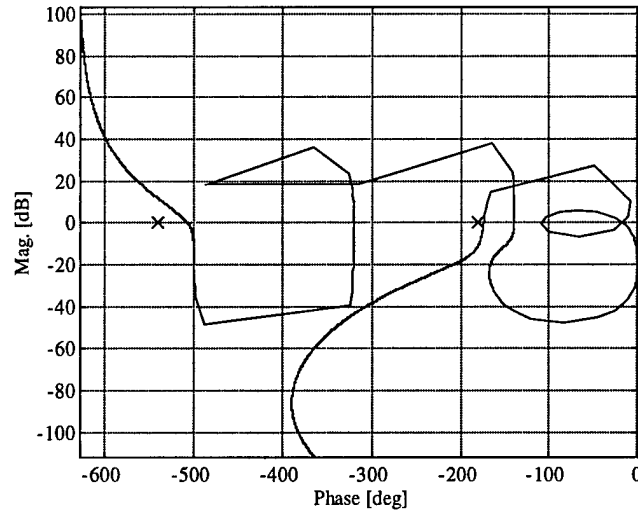


Figure 64: Open Loop Gain vs. Phase at 250 Hz, Internal Hysteretic Damping
 $\eta_H = 2 \times 10^{-4}$, Internal Viscous Damping $\eta_V = 2 \times 10^{-6}$

Figure 65 presents the open and closed loop frequency response of the controlled bearing furthest away from the motor. The dashed line corresponds to the uncontrolled rotor (open loop plant and controller response combined case from Figures 63 and 64) and the solid line shows the controlled rotor.

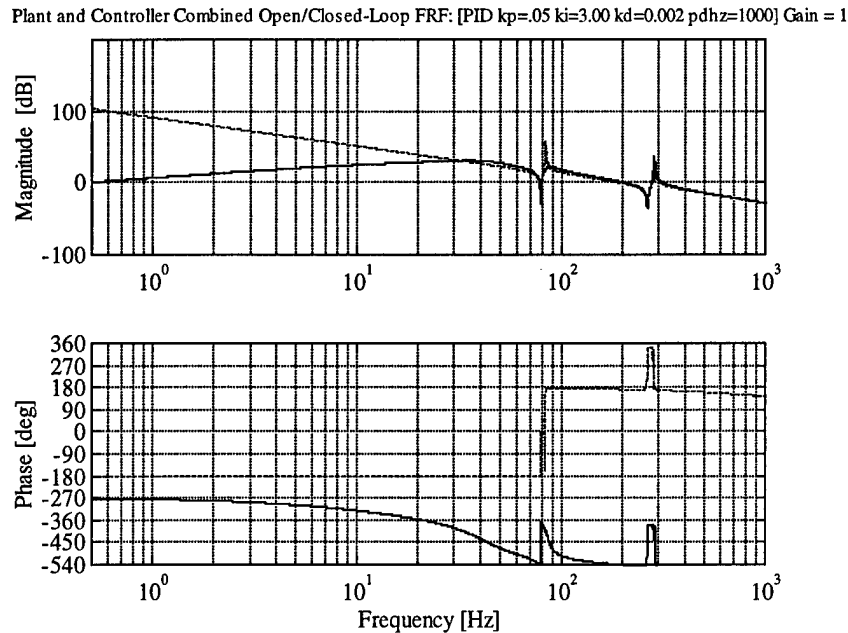


Figure 65: Open and Closed Loop Frequency Response, Internal Hysteretic Damping
 $\eta_H = 2 \times 10^{-4}$, Internal Viscous Damping $\eta_V = 2 \times 10^{-6}$

Based on the results from Figures 63-65, and based on the earlier results of the root loci plots (Figure 51) it appears that a PID controller is not sufficient to control a rotor with internal viscous and hysteretic damping above its critical speed.

Again, it is important to point out how similar these results are to the case with only internal viscous damping. This tends to suggest that the stabilizing effects of internal viscous damping at speeds below its critical speed was sufficient to overcome the destabilizing effects of the internal hysteretic damping in the rotor. This is consistent with the root loci plots in Figure 53, the stabilizing term in equation (72), and is also shown in Figure 16.

To summarize, several PID controllers were designed and implemented in an effort to stabilize a rotor system with internal damping. These efforts focused on controller design in the frequency domain with subsequent testing in the full simulation. For the cases with internal viscous damping, the PID controller was able to maintain stability for sub-critical speeds only. For the internal hysteretic damping case, the PID controller was able to maintain control for all speeds tested, although in reality the inherent limitations of a PID controller will eventually cause the rotor to become unstable. Table 8 compares the simulation and FEM results for all cases of internal damping.

Although PID controllers were effective in stabilizing the rotor systems at sub-critical speeds, the model developed during this thesis showed that these controllers were unable to counteract the destabilizing effects of internal damping during supercritical operation. Other more complex controllers should be designed specifically to achieve improved control and increase the instability threshold for the system.

Other important findings regarding internal damping include:

- The erratic changes in the phase angle for systems with internal damping could be a factor in determining the stability of the system. Further study should be performed to determine specifically how the phase angle and internal damping are related.
- The results of the rotor with internal viscous damping were very similar to the results of the case where both internal viscous and hysteretic damping were included. This tends to suggest that the stabilizing effects of internal viscous damping at speeds below its critical speed was sufficient to overcome the destabilizing effects of the internal hysteretic damping in the rotor.

Table 8: Comparison of Instability Threshold Predictions
FEM Model: Bearing Stiffness = 50 lbs/in, Bearing Damping = 1.5×10^{-2} lbs-sec/in
Simulation: $K_P = 0.05$ lb/mil, $K_I = 3.00$ lb/mil-s, $K_D = 0.002$ lb-sec/mil,
Derivative Bandwidth = 1000 Hz

Internal Damping	Critical Speeds (Hz)		Instability Threshold (Hz)	
	FEM ¹	Simulation ²	FEM ¹	Simulation ²
$\eta_V = 2 \times 10^{-6}$	272.5	289	441	289
$\eta_H = 0.0002$	272.5	289	Stable for all Speeds	Stable for all Speeds
$\eta_V = 2 \times 10^{-6}, \eta_H = 0.0002$	272.5	289	425	289

¹ Extended FEM model has constant bearing properties

² Modified Simulation

Chapter 8 Summary and Conclusions

In the first few chapters of this thesis the concepts of external and internal damping were explored. Internal damping was defined and divided into two distinct types: internal viscous and internal hysteretic damping. Next, internal damping was included in a rotating system and it was shown how under certain conditions, internal damping can cause the rotor to become unstable. The following general conclusions regarding internal and external damping and their effects on stability were made:

- If the external and internal damping are both viscous in nature, then the rotor will always be stable in its sub-critical speed range. Stability can be extended into the supercritical regime by adding external damping according to the results obtained by Smith, equation (56).
- If the external and internal damping are both hysteretic, the rotor will be unstable for all speeds unless the external damping is large enough to establish stability. In this case, the rotor will be stable for all speeds.
- If the external damping is viscous and the internal damping is hysteretic, the rotor will be unstable in a range of speeds beginning at $\Omega = 0+$. As the external viscous damping increases, this speed range shrinks toward $\Omega = 0$ until the external damping reaches a value that results in stability for all speeds, i.e. for $\Omega \geq 0$.

After the general characteristics of internal damping were discussed, a finite element model that included internal damping was developed and validated using a standard test case from the references. This model was then used to produce state space matrices that fully described a rotor with and without internal damping. To make use of

these matrices, a Matlab™ magnetic bearing simulation developed by Draper Laboratory (Scholten) was modified to include internal damping. The modified simulation was able to predicted rigid body modes, critical speeds, rotor displacements and instability thresholds.

Prior to entering the rotor model with internal damping into the simulation, the original FEM model (Antkowiak) and simulation (Scholten) predictions were compared to actual rotor test results. The FEM model critical speed prediction was slightly lower than the actual rotor rig critical speed. This was probably due to the simplicity of the FEM model since it did not take into account rotor unbalance and it did not model any other overall system effects such as magnetic bearing material non-linearity, actuator lag, etc.

In contrast to the simple FEM model, the high fidelity simulation predicted a first critical speed that closely matched the actual rotor test data, although the rigid body mode predictions were not as accurate. With regard to the displacements predicted by the simulation, good agreement was seen in terms of the predicted and actual displacements for the bearing furthest away from the elastic coupling, although the simulation predicted somewhat lower displacements for the closer bearing. This suggests that more work needs to be done on the elastic coupling block of the simulation. In terms of the vertical displacements at the bearings, the simulation had good correlation to the actual rotor data, while the predicted horizontal displacements were slightly smaller than the actual rotor data.

The only area where the simulation had poor accuracy with regard to the actual rotor displacements was in the speed range near the rigid body mode. Since the

simulation predicted the rigid body mode at 47 Hz, its displacement predictions at the actual rigid body mode of 52 Hz would not be as large.

After verifying the high fidelity simulation and incorporating the destabilizing effects of internal damping, several PID controllers were designed and implemented in an effort to stabilize a rotor system with internal damping. These efforts focused on controller design in the frequency domain with subsequent testing in the full simulation. For the cases with internal viscous damping, the PID controller was able to maintain stability for sub-critical speeds only. For the internal hysteretic damping case, the PID controller was able to maintain control for all speeds tested, although in reality the inherent limitations of a PID controller will eventually cause the rotor to become unstable above its critical speed. Other important findings regarding internal damping and the PID controller included:

- The erratic changes in the phase angle for systems with internal damping could be a factor in determining the stability of the system. Further study should be performed to determine specifically how the phase angle and internal damping are related.
- The results of the rotor with internal viscous damping were very similar to the results of the case where both internal viscous and hysteretic damping were included. This tends to suggest that the stabilizing effects of internal viscous damping at speeds below its critical speed was sufficient to overcome the destabilizing effects of the internal hysteretic damping in the rotor.

To continue this study, a number of tasks should be undertaken. First, a proper measurement of the internal viscous and hysteretic damping of the shaft should be made. Next, a higher speed motor must be acquired to test where the rotor actually becomes unstable. Based on these actual rotor results, the internal damping models might need to be extended. In addition, instability threshold predictions of shaft with an additional inertia, such as a disc, should be compared to actual test data. This would lead to a more useful simulation, since it is more representative of real-world applications. A final suggestion for further study in the realm of magnetic bearings and controls should include testing whether centralized control, as opposed to the current decentralized control, could improve the system stability margin.

The PID controllers were effective in stabilizing the rotor systems at sub-critical speeds. However, the model developed during this thesis showed that these controllers were unable to counteract the destabilizing effects of internal damping during supercritical operation. Other more complex controllers should be designed and tested specifically to achieve improved control and increase the instability threshold for the system. This improved rotordynamic model and magnetic bearing simulation is now available to test these designs in the supercritical regime.

References

1. Baur, P., "Field Balancing of Rotating Machinery," *Power*, vol 127, n. 10, October 1983
2. Zorzi, E.S., Nelson, H.D., "Finite Element Simulation of Rotor-Bearing Systems with Internal Damping", *Journal of Engineering for Power*, January 1977
3. Den Hartog, J.P., *Mechanical Vibrations*, McGraw Hill Book Company, 1956
4. Rao. Singiresu, S., *Mechanical Vibrations*, Addison-Wesley Publishing Company, 1990
5. Nashif, Jones, Henderson, *Vibration Damping*, John Wiley and Sons, Inc., 1985
6. Nelson, Frederick, *Damping in Structural Analysis and Design, Impact and Friction Solids, Structures, and Machines* Birkhäuser In Press, 1999
7. Bert, C.W., *Material Damping: An Introductory Review of Mathematical Models, Measures and Experimental Techniques*, *Journal of Sound and Vibration*, Vol. 29, p. 129-153, February 1973
8. Graham, W.B., "Material Damping and Its Role in Linear Dynamic Equations", *UTIAS Review*, No. 36, 1973
9. Gunter, Edgar, J., "Dynamic Stability of Rotor-Bearing Systems", NASA SP-113, 1966
10. Kimball, A.L., *Vibration Prevention in Engineering*, John Wiley & Sons, London, 1932
11. Lund, J.W., "Stability and Damped Critical Speeds of a Flexible Rotor in Fluid Film Bearings", ASME Design Engineering Division, Publication DE v 2 pt. 1, 11th Biennial Conference on Mechanical Vibration and Noise, Rotating Machinery Dynamics, 1987, Boston, MA
12. Kramer, Erwin *Dynamics of Rotors and Foundations*, Springer-Verlag Berlin Heidelberg, 1993
13. Ehrich, F.F., "Shaft Whirl Induced by Rotor Internal Damping", *Journal of Applied Mechanics*, June 1964
14. Dimarogonis, A.D., *Analytical Methods in Rotor Dynamics*, Applied Science Publishers, London, 1983
15. Dimentberg, F. M., *Flexural Vibrations of Rotating Shafts*, Butterworths, London, 1961
16. Nelson, H.D., McVaugh, J.M., "The Dynamics of Rotor Bearing Systems: Using Finite Elements", *Journal of Engineering for Industry*, May 1976
17. Nelson, H.D., "A Finite Rotating Shaft Element Using Timoshenko Beam Theory," Engineering Research Center Report ERC-R-77023, Arizona State University, 1977.
18. Antkowiak, B.M., Scholten, J. R., Nelson, F.C., "Rotordynamic Modeling and Control System for an Aircraft Gas Turbine Rotor Suspended on Magnetic Bearings," 1998
19. Antkowiak, B.M., The Charles Stark Draper Laboratory, Personal Communications, 1998-99
20. Scholten, J.R., The Charles Stark Draper Laboratory, Personal Communications, 1998-99
21. Kaiser, K.W., The Charles Stark Draper Laboratory, Personal Communications, 1998-99

Appendix A - Detailed Information on Draper Magnetic Bearing Test Apparatus

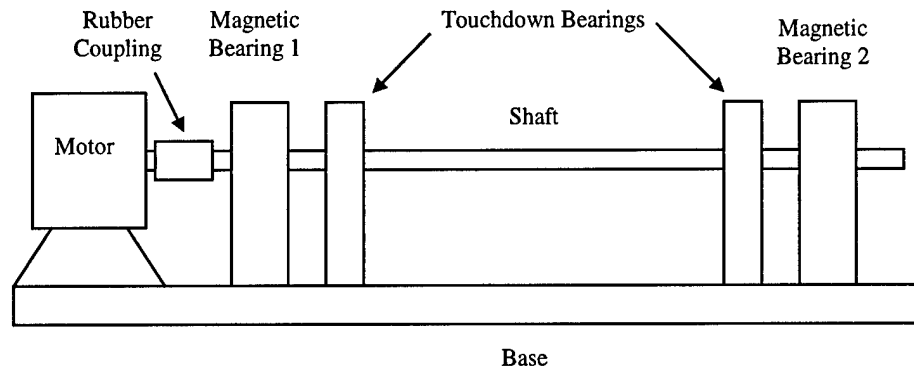


Figure A1: Draper Magnetic Bearing Test Rig

Motor Base -

The base structure for the test rig is from a Bently Nevada RK-3 rotor kit. This kit includes an electric motor mounted on a base plate that drives the shaft. The motor and controller have the capability to operate in the range of 0 to 10,000 rpm. The motor is connected to the shaft via an elastic coupling.

Rotor –

The rotating assembly is comprised of two actuator rotors designed by Draper Laboratory pressed onto a 3/8" diameter stainless steel shaft. The actuator is an aluminum spool surrounded by multiple magnetic material laminations and a ferrous iron ring, which is used as the sensor plate for the eddy current sensors. A threaded brass nut is used to secure the laminations to the spool. The iron ring is mounted with a shrink fit.

Magnetic Actuators-

A four-pole hetro polar bearing design at Draper Laboratory was used on the rotor test rig. A frameless stator design was selected so that the stator laminations could easily be mounted in a common aluminum housing. A nominal radial air gap of 0.012" was selected.

The lamination stack for the stator and rotor were made out of Carpenter Hiperc alloy 50 in 14 mil sheets. Hiperc50 is an iron-cobalt-vandium soft magnetic alloy. This alloy was advertised to have a saturation of 2 Tesla when heat-treated accordingly.

The stator was designed to accommodate 120 turns of #20 gauge wire. To minimize thermal heating in the copper coil, a maximum current density of 5,000 amps/in² was used. For desirable operation in the linear range of the BH curve, less than 1.74 tesla, and a bearing load capacity of 10 lbs, sized the cross sectional area of the pole to be 0.025 in². This calculation dictated that a stack of 9 laminations (0.126 in thick by 0.2 pole width) was used in the stator design, [21].

Touchdown Bearings-

In case of excess shaft vibration or controller failure, touchdown bearings were provided to protect the stators of the magnetic bearings. They provided a radial clearance of 0.008" from the center of the bearing.

Computer hardware and software-

The digital signal processing (DSP) hardware is based on a single Texas Instruments C40 DSP operating at 50 megahertz. Several PC-hosted circuit boards were used for processing, digital to analog conversion, and analog to digital conversions. All of these boards were manufactured by dSpace, inc. Along with their hardware, dSpace provided low-level support software libraries for running and monitoring the DSP. The magnetic bearing control software running on the DSP was written by Draper Laboratory in the C language (Scholten). For speed and calculation robustness, linear transfer functions were coded in assembly language as Z-transform biquad filters, (Scholten, [22]). The sample rate was 10 kHz.

The DSP system was hosted on a Pentium PC. It provided support for the following:

- Data logging, using Trace40 application from dSpace;
- Analysis of logged data, using Draper developed software routines;
- System Simulation using the Matlab and Simulink Applications;
- A custom user interface written in C which provided for monitoring the dSpace real time (Scholten).

Appendix B - A Timoshenko Rotor Element

No Internal Damping

In line with its work on magnetic bearings, The Charles Stark Draper Laboratory has produced a rotor dynamic finite element model that is based on Timoshenko beam theory. A Timoshenko rotor uses an element with 2 nodes and 8 Degrees of Freedom and uses third order shape functions to describe the bending of the element. All additional inertia are assumed to be rigid discs with lump mass properties and the bearings are assumed to be discrete and linear. The model includes rotary inertia, gyroscopic moments, and shear deformation effects ($\bar{\Phi}$). Following the derivation described by Nelson [16, 17] the shape functions are:

Translational Shape Functions:

$$\begin{aligned}\Lambda_1 &= \frac{1}{1+\bar{\Phi}} \left[1 - 3\left(\frac{s}{l}\right)^2 + 2\left(\frac{s}{l}\right)^3 + \bar{\Phi} \left(1 - \frac{s}{l}\right) \right] \\ \Lambda_2 &= \frac{1}{1+\bar{\Phi}} \left[s \left(1 - 2\left(\frac{s}{l}\right) + \left(\frac{s}{l}\right)^2 \right) + \bar{\Phi} \frac{l}{2} \left(\left(\frac{s}{l}\right) - \left(\frac{s}{l}\right)^2 \right) \right] \\ \Lambda_3 &= \frac{1}{1+\bar{\Phi}} \left[3\left(\frac{s}{l}\right)^2 - 2\left(\frac{s}{l}\right)^3 + \bar{\Phi} \frac{s}{l} \right] \\ \Lambda_4 &= \frac{1}{1+\bar{\Phi}} \left[l \left(-\left(\frac{s}{l}\right)^2 + \left(\frac{s}{l}\right)^3 \right) + \bar{\Phi} \frac{l}{2} \left[-\left(\frac{s}{l}\right) + \left(\frac{s}{l}\right)^2 \right] \right]\end{aligned}\tag{B.1a,b,c,d}$$

Rotational Shape Functions:

$$\begin{aligned}
\Theta_i &= \frac{1}{1+\overline{\Phi}} [\phi_i + \overline{\Phi} v_i] \\
\Theta_1 &= \frac{1}{1+\overline{\Phi}} \left[\frac{1}{l} \left(-6 \left(\frac{s}{l} \right) + 6 \left(\frac{s}{l} \right)^2 \right) \right] \\
\Theta_2 &= \frac{1}{1+\overline{\Phi}} \left[1 - 4 \left(\frac{s}{l} \right) + 3 \left(\frac{s}{l} \right)^2 + \overline{\Phi} \left(1 - \frac{s}{l} \right) \right] \\
\Theta_3 &= \frac{1}{1+\overline{\Phi}} \left[\frac{1}{l} \left(6 \left(\frac{s}{l} \right) - 6 \left(\frac{s}{l} \right)^2 \right) \right] \\
\Theta_4 &= \frac{1}{1+\overline{\Phi}} \left[-2 \left(\frac{s}{l} \right) + 3 \left(\frac{s}{l} \right)^2 + \overline{\Phi} \frac{s}{l} \right]
\end{aligned} \tag{B.2a,b,c,d}$$

The matrix $[\underline{\Lambda}]$ transforms the nodal displacement vector (V, W) into the rotor translational displacements (V_{bend} , W_{bend}), while the matrix $[\underline{\Theta}]$ converts the displacements into the rotor cross-section center line translations (V_{shear} , W_{shear}).

$$\begin{aligned}
[\underline{\Lambda}] &= \begin{bmatrix} \Lambda_1 & 0 & 0 & \Lambda_2 & \Lambda_3 & 0 & 0 & \Lambda_4 \\ 0 & \Lambda_1 & -\Lambda_2 & 0 & 0 & \Lambda_3 & -\Lambda_4 & 0 \end{bmatrix} \\
[\underline{\Theta}] &= \begin{bmatrix} 0 & -\Theta_1 & \Theta_2 & 0 & 0 & -\Theta_3 & \Theta_4 & 0 \\ \Theta_1 & 0 & 0 & \Theta_2 & \Theta_3 & 0 & 0 & \Theta_4 \end{bmatrix}
\end{aligned} \tag{B.3a,b}$$

From the rotor configuration shown in Figure B1, the rotations β and Γ are defined as:

$$\beta = -\frac{\partial W}{\partial z} \tag{B.4}$$

$$\Gamma = \frac{\partial V}{\partial z} \tag{B.5}$$

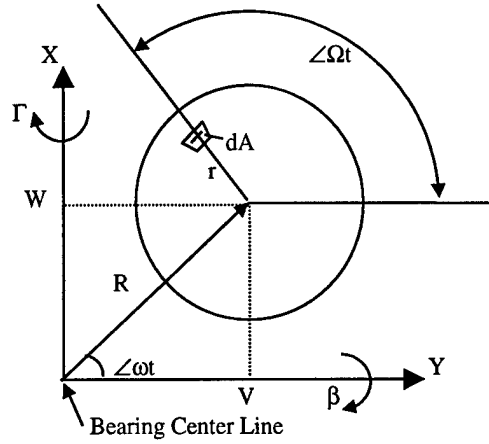


Figure B1: Rotor System Configuration, Nelson

Using the Lagrangian approach, Nelson calculated the potential and kinetic energy of the rotating element. The rotor potential energy of the rotor was stored in two forms, bending deformation, and shear deformation (axial loads neglected):

$$V = \int_0^l \frac{1}{2} EI \begin{Bmatrix} V_{bend}'' \\ W_{bend}'' \end{Bmatrix}^T \begin{Bmatrix} V_{bend}'' \\ W_{bend}'' \end{Bmatrix} dz + \int_0^l \frac{1}{2} \kappa A G \begin{Bmatrix} V_{shear}'' \\ W_{shear}'' \end{Bmatrix}^T \begin{Bmatrix} V_{shear}'' \\ W_{shear}'' \end{Bmatrix} dz \quad (B.6)$$

where the shear deformation factor is given by κ and the second derivative of the bending deformation in the y direction is represented by V_{bend}'' . The rotor kinetic energy included Timoshenko effects of rotary inertia, shear deformation, and the gyroscopic energy:

$$T = \int_0^l \frac{1}{2} \rho A \begin{Bmatrix} \dot{V} \\ \dot{W} \end{Bmatrix}^T \begin{Bmatrix} \dot{V} \\ \dot{W} \end{Bmatrix} dz + \int_0^l \frac{1}{2} \rho I_d \begin{Bmatrix} \dot{\beta} \\ \dot{\Gamma} \end{Bmatrix}^T \begin{Bmatrix} \dot{\beta} \\ \dot{\Gamma} \end{Bmatrix} dz + \int_0^l \frac{1}{2} \rho I_p \Omega^2 ds - \int_0^l I_p \Omega \beta \dot{\Gamma} dz \quad (B.7)$$

Nelson, then proceeded to derive the following matrices:

$$[M_{trans}] = \frac{\rho A l}{420(1 + \bar{\Phi})^2} \begin{bmatrix} m_1 & & & & & & & \\ 0 & m_1 & & & & & & \\ 0 & -m_3 & m_2 & & & & & \\ m_3 & 0 & 0 & m_2 & & & & \\ m_4 & 0 & 0 & m_5 & m_1 & & & \\ 0 & m_4 & -m_5 & 0 & 0 & m_1 & & \\ 0 & m_5 & -m_6 & 0 & 0 & m_3 & m_2 & \\ -m_5 & 0 & 0 & -m_6 & -m_3 & 0 & 0 & m_2 \end{bmatrix} \quad (B.8)$$

where the elements in the translational mass matrix are defined by:

$$\begin{aligned} m_1 &= 156 + 249\bar{\Phi} + 140\bar{\Phi}^2 \\ m_2 &= l^2(4 + 7\bar{\Phi} + 3.5\bar{\Phi}^2) \\ m_3 &= l(22 + 38.5\bar{\Phi} + 17.5\bar{\Phi}^2) \\ m_4 &= 54 + 126\bar{\Phi} + 70\bar{\Phi}^2 \\ m_5 &= l(13 + 31.5\bar{\Phi} + 17.5\bar{\Phi}^2) \\ m_6 &= l^2(3 + 7\bar{\Phi} + 3.5\bar{\Phi}^2) \end{aligned} \quad (B.9a,b,c,d,e,f)$$

$$[M_{rot}] = \frac{\rho A l}{120(1 + \bar{\Phi})^2} \begin{bmatrix} n_1 & & & & & & & \\ 0 & n_1 & & & & & & \\ 0 & -n_3 & n_2 & & & & & \\ n_3 & 0 & 0 & n_2 & & & & \\ -n_1 & 0 & 0 & -n_3 & n_1 & & & \\ 0 & -n_1 & n_3 & 0 & 0 & n_1 & & \\ 0 & -n_3 & -n_4 & 0 & 0 & n_3 & n_2 & \\ n & 0 & 0 & -n_4 & -n_3 & 0 & 0 & n_2 \end{bmatrix} \quad (B.10)$$

where the elements in the rotational mass matrix are defined by:

$$\begin{aligned} n_1 &= 36 \\ n_2 &= l^2(4 + 5\bar{\Phi} + 10\bar{\Phi}^2) \\ n_3 &= l(3 - 15\bar{\Phi}) \\ n_4 &= l^2(1 + 5\bar{\Phi} - 5\bar{\Phi}^2) \end{aligned} \quad (B.11a,b,c,d)$$

$$[K] = \frac{EI}{l^3(1+\bar{\Phi})} \begin{bmatrix} k_1 & & & & & & & \\ 0 & k_1 & & & & & & \\ 0 & -k_3 & k_2 & & & & & \\ k_3 & 0 & 0 & k_2 & & & & \\ -k_1 & 0 & 0 & -k_3 & k_1 & & & \\ 0 & -k_1 & k_3 & 0 & 0 & k_1 & & \\ 0 & -k_3 & k_4 & 0 & 0 & k_3 & k_2 & \\ k_3 & 0 & 0 & -k_3 & -k_3 & 0 & 0 & k_2 \end{bmatrix} \quad (B.12)$$

where the individual elements in the stiffness matrix are defined by:

$$\begin{aligned} k_1 &= 12 \\ k_2 &= (\text{length } l)^2 (4 + \bar{\Phi}) \\ k_3 &= 6l \\ k_4 &= l^2 (2 - \bar{\Phi}) \end{aligned} \quad (B.13,a,b,c,d)$$

$$[G] = \frac{\rho A r^2}{60l(1+\bar{\Phi})^2} \begin{bmatrix} 0 & & & & & & & \\ g_1 & 0 & & & & & & \\ -g_3 & 0 & 0 & & & & & \\ 0 & -g_3 & g_2 & 0 & & & & \\ 0 & g_1 & -g_3 & 0 & 0 & & & \\ -g_1 & 0 & 0 & -g_3 & g_1 & 0 & & \\ -g_3 & 0 & 0 & g_4 & g_3 & 0 & 0 & \\ 0 & -g_3 & g_4 & 0 & 0 & g_3 & g_2 & 0 \end{bmatrix} \quad (B.14)$$

where the individual element in the gyroscopic matrix are defined by:

$$\begin{aligned} g_1 &= 36 \\ g_2 &= (4 + 5\bar{\Phi} + 10\bar{\Phi}^2)l \\ g_3 &= (-3 + 15\bar{\Phi})l \\ g_4 &= (-1 - 5\bar{\Phi} + 5\bar{\Phi}^2)l^2 \end{aligned} \quad (B.15a,b,c,d)$$

By the application of Hamilton's extended principle, and using the above matrices and energy and work functions, Nelson produced the following undamped matrix equations of motion:

$$([M_{trans}] + [M_{rot}])\{\ddot{q}\} - \Omega[G]\{\dot{q}\} + [K_{bend}]\{q\} = \{f\} \quad (B.16)$$

where:

$\{q\}$ - fixed frame physical coordinates

$\{f\}$ - fixed frame external forces

Ω - rotor spin speed

The eigenvalues for the undamped equation of motion occur in conjugate pairs and are given by: $S_j = \pm i\omega_j$, where the imaginary pair $\pm i\omega$ represents the forward and backward whirl frequencies of the shaft.

Addition of Internal Damping

Based on the work of Zorzi and Nelson, [2], the previous derivation of the rotordynamic equations of motion can be modified to include the contributions of internal damping. Nelson used both of the internal viscous and hysteretic damping models discussed in the previous chapters. Adding this combination of internal damping terms into the constitutive relationship yields:

$$\sigma_x = E \left\{ \frac{\varepsilon_x}{\sqrt{1 + \eta_H^2}} + \left(\eta_V + \frac{\eta_H}{\Omega \sqrt{1 + \eta_H^2}} \right) \dot{\varepsilon}_x \right\} \quad (B.17)$$

Further, by defining the whirl radius as R and the shaft radius as r (see Figure B1), the strain and strain rate are:

$$\begin{aligned}\varepsilon_x &= -r \cos[(\Omega - \omega)t] \frac{\partial^2 R}{\partial^2 x} \\ \dot{\varepsilon}_x &= (\Omega - \omega)r \sin[(\Omega - \omega)t] \frac{\partial^2 R}{\partial^2 x} - r \cos[(\Omega - \omega)t] \frac{\partial}{\partial t} \frac{\partial^2 R}{\partial^2 x}\end{aligned}\quad (\text{B.18a,b})$$

Again from Figure B1, the internal bending moments M_z and M_y can be expressed as:

$$\begin{aligned}M_y &= \int_A [W + r \sin(\Omega t)] \sigma_x dr (rd(\Omega t)) \\ M_z &= \int_A -[V + r \cos(\Omega t)] \sigma_x dr (rd(\Omega t))\end{aligned}\quad (\text{B.19a,b})$$

After substituting the modified constitutive relationship into the internal bending moments and performing the integrations, the moments can be expressed as:

$$\begin{Bmatrix} M_z \\ M_y \end{Bmatrix} = EI \begin{bmatrix} \frac{1+\eta_H}{\sqrt{1+\eta_H^2}} & \left(\frac{1+\eta_H}{\sqrt{1+\eta_H^2}} + \eta_v \Omega \right) \\ \left(\frac{1+\eta_H}{\sqrt{1+\eta_H^2}} + \eta_v \Omega \right) & -\frac{1+\eta_H}{\sqrt{1+\eta_H^2}} \end{bmatrix} \begin{Bmatrix} V'' \\ W'' \end{Bmatrix} + EI \begin{bmatrix} \eta_v & 0 \\ 0 & -\eta_v \end{bmatrix} \begin{Bmatrix} \dot{V}'' \\ \dot{W}'' \end{Bmatrix} \quad (\text{B.20})$$

$$[\eta] = \begin{bmatrix} \frac{1+\eta_H}{\sqrt{1+\eta_H^2}} & \left(\frac{1+\eta_H}{\sqrt{1+\eta_H^2}} + \eta_v \Omega \right) \\ \left(\frac{1+\eta_H}{\sqrt{1+\eta_H^2}} + \eta_v \Omega \right) & -\frac{1+\eta_H}{\sqrt{1+\eta_H^2}} \end{bmatrix} \quad (\text{B.21})$$

Now placing the energy contributions from these moment equations into the appropriate kinetic or potential energy equations defined in section 4.1, gives:

$$\begin{aligned}V &= \int_0^l \frac{1}{2} EI \begin{Bmatrix} V_{bend}'' \\ W_{bend}'' \end{Bmatrix}^T \begin{Bmatrix} V_{bend}'' \\ W_{bend}'' \end{Bmatrix} dz + \int_0^l \frac{1}{2} \kappa AG \begin{Bmatrix} V_{shear}' \\ W_{shear}' \end{Bmatrix}^T \begin{Bmatrix} V_{shear}' \\ W_{shear}' \end{Bmatrix} dz + \\ &+ \int_0^l \frac{1}{2} EI \begin{Bmatrix} V_{bend}'' \\ W_{bend}'' \end{Bmatrix}^T [\eta] \begin{Bmatrix} V_{bend}'' \\ W_{bend}'' \end{Bmatrix} dz\end{aligned}\quad (\text{B.22})$$

$$\begin{aligned}
T = & \int_0^l \frac{1}{2} \rho A \left\{ \begin{matrix} \dot{V} \\ \dot{W} \end{matrix} \right\}^T \left\{ \begin{matrix} \dot{V} \\ \dot{W} \end{matrix} \right\} dz + \int_0^l \frac{1}{2} \rho I_d \left\{ \begin{matrix} \dot{\beta} \\ \dot{\Gamma} \end{matrix} \right\}^T \left\{ \begin{matrix} \dot{\beta} \\ \dot{\Gamma} \end{matrix} \right\} dz + \\
& + \int_0^l \frac{1}{2} \rho I_p \Omega^2 dz - \int_0^l I_p \Omega \beta \dot{\Gamma} dz + \int_0^l \frac{1}{2} \eta_v EI \left\{ \begin{matrix} V_{bend}'' \\ W_{bend}'' \end{matrix} \right\}^T \left\{ \begin{matrix} V_{bend}'' \\ W_{bend}'' \end{matrix} \right\} dz
\end{aligned} \tag{B.23}$$

Again using the Lagrangian approach, Nelson finally proceeds to derive the equation of motion for a Timoshenko shaft finite element with internal damping. This is given by:

$$\begin{aligned}
& ([M_{trans}] + [M_{rot}])\{\ddot{q}\} + (\eta_v[K] - \Omega[G] + [C_e])\{\dot{q}\} + \\
& \left[\frac{1 + \eta_H}{\sqrt{1 + \eta_H^2}} [K] + \left(\eta_v \Omega + \frac{\eta_H}{\sqrt{1 + \eta_H^2}} \right) [K_{cir}] \right] \{q\} = \{f\}
\end{aligned} \tag{B.24}$$

All of the instabilities of the system are characterized by the new skew-symmetric circulation stiffness matrix, [2]. It is given by:

$$[K_{cir}] = \frac{EI}{l^3} \begin{bmatrix} 0 & & & & & & & \\ -12 & 0 & & & & & & \\ 6l & 0 & 0 & & & & & \\ 0 & 6l & -4l^2 & 0 & & & & \\ 0 & -12 & 6l & 0 & 0 & & & \\ 12 & 0 & 0 & 6l & -12 & 0 & & \\ 6l & 0 & 0 & 2l^2 & -6l & 0 & 0 & \\ 0 & 6l & -2l^2 & 0 & 0 & -6l & -4l^2 & 0 \end{bmatrix} \tag{B.25}$$

Solving the equations of motion with internal damping results in eigenvalues in the form of: $S_j = \lambda_j \pm i\omega_j$, where ω provides shaft whirl and λ provides an orbit growth/decay after a perturbation.

Appendix C: Input Files for Draper Rotor FEM Program

Input File for Rotor - No Internal Damping, No Constraints

ELEMENT	1	3	0.500	0.3125
ELEMENT	2	1	0.675	0.3748
ELEMENT	3	1	0.675	0.3748
ELEMENT	4	2	0.360	0.3748
ELEMENT	5	2	0.500	0.3748
ELEMENT	6	2	0.440	0.3748
ELEMENT	7	1	1.000	0.3748
ELEMENT	8	1	1.000	0.3748
ELEMENT	9	1	1.000	0.3748
ELEMENT	10	1	1.000	0.3748
ELEMENT	11	1	1.000	0.3748
ELEMENT	12	1	1.000	0.3748
ELEMENT	13	1	1.000	0.3748
ELEMENT	14	1	1.000	0.3748
ELEMENT	15	1	1.000	0.3748
ELEMENT	16	2	0.440	0.3748
ELEMENT	17	2	0.500	0.3748
ELEMENT	18	2	0.360	0.3748
ELEMENT	19	1	0.625	0.3748
ELEMENT	20	1	0.625	0.3748
MATERIAL	1		29.5E+06	.33 7.27-04
MATERIAL	2		69.3E+06	.33 8.40-04
MATERIAL	3		10.0E+06	.45 7.50-04
CONSTRAINT	1		000.0	000.0
CONSTRAINT	5		0.000E+00	0.000E+00
CONSTRAINT	6		0.000E+04	0.000E+04
CONSTRAINT	8		0.000E+00	0.000E+00
CONSTRAINT	11		0.000E+00	0.000E+00
CONSTRAINT	15		0.000E+00	0.000E+00
CONSTRAINT	17		0.000E+04	0.000E+04
CONSTRAINT	18		0.000E+00	0.000E+00
CONSTRAINT	21		0.000E+00	0.000E+00
ADDMASS	4		32.00E-06	1.500E-06 2.700E-06
ADDMASS	5		68.00E-06	4.100E-06 5.800E-06
ADDMASS	6		62.00E-06	3.600E-06 5.300E-06
ADDMASS	7		26.00E-06	1.200E-06 2.200E-06
ADDMASS	16		26.00E-06	1.200E-06 2.200E-06
ADDMASS	17		62.00E-06	3.600E-06 5.300E-06
ADDMASS	18		68.00E-06	4.100E-06 5.800E-06
ADDMASS	19		32.00E-06	1.500E-06 2.700E-06

Input File for Rotor - No Internal Damping, With Constraints from Estimated Bearing

ELEMENT	1	3	0.500	0.3125	
ELEMENT	2	1	0.675	0.3748	
ELEMENT	3	1	0.675	0.3748	
ELEMENT	4	2	0.360	0.3748	
ELEMENT	5	2	0.500	0.3748	
ELEMENT	6	2	0.440	0.3748	
ELEMENT	7	1	1.000	0.3748	
ELEMENT	8	1	1.000	0.3748	
ELEMENT	9	1	1.000	0.3748	
ELEMENT	10	1	1.000	0.3748	
ELEMENT	11	1	1.000	0.3748	
ELEMENT	12	1	1.000	0.3748	
ELEMENT	13	1	1.000	0.3748	
ELEMENT	14	1	1.000	0.3748	
ELEMENT	15	1	1.000	0.3748	
ELEMENT	16	2	0.440	0.3748	
ELEMENT	17	2	0.500	0.3748	
ELEMENT	18	2	0.360	0.3748	
ELEMENT	19	1	0.625	0.3748	
ELEMENT	20	1	0.625	0.3748	
MATERIAL	1		29.5E+06	.33	7.27-04
MATERIAL	2		69.3E+06	.33	8.40-04
MATERIAL	3		10.0E+06	.45	7.50-04
CONSTRAINT	1		000.0	000.0	
CONSTRAINT	5		0.000E+00	0.000E+00	
CONSTRAINT	6		5.000E+01	5.000E+01	1.500E-02 1.500E-02
CONSTRAINT	8		0.000E+00	0.000E+00	
CONSTRAINT	11		0.000E+00	0.000E+00	
CONSTRAINT	15		0.000E+00	0.000E+00	
CONSTRAINT	17		5.000E+01	5.000E+01	1.500E-02 1.500E-02
CONSTRAINT	18		0.000E+00	0.000E+00	
CONSTRAINT	21		0.000E+00	0.000E+00	
ADDMASS	4		32.00E-06	1.500E-06	2.700E-06
ADDMASS	5		68.00E-06	4.100E-06	5.800E-06
ADDMASS	6		62.00E-06	3.600E-06	5.300E-06
ADDMASS	7		26.00E-06	1.200E-06	2.200E-06
ADDMASS	16		26.00E-06	1.200E-06	2.200E-06
ADDMASS	17		62.00E-06	3.600E-06	5.300E-06
ADDMASS	18		68.00E-06	4.100E-06	5.800E-06
ADDMASS	19		32.00E-06	1.500E-06	2.700E-06

Input File for Rotor - Internal Damping Included, No Constraints

```

ELEMENT      1  3 0.500  0.3125
ELEMENT      2  1 0.675  0.3748
ELEMENT      3  1 0.675  0.3748
ELEMENT      4  2 0.360  0.3748
ELEMENT      5  2 0.500  0.3748
ELEMENT      6  2 0.440  0.3748
ELEMENT      7  1 1.000  0.3748
ELEMENT      8  1 1.000  0.3748
ELEMENT      9  1 1.000  0.3748
ELEMENT     10  1 1.000  0.3748
ELEMENT     11  1 1.000  0.3748
ELEMENT     12  1 1.000  0.3748
ELEMENT     13  1 1.000  0.3748
ELEMENT     14  1 1.000  0.3748
ELEMENT     15  1 1.000  0.3748
ELEMENT     16  2 0.440  0.3748
ELEMENT     17  2 0.500  0.3748
ELEMENT     18  2 0.360  0.3748
ELEMENT     19  1 0.625  0.3748
ELEMENT     20  1 0.625  0.3748
MATERIAL      1  29.5E+06 .33  7.27-04  2.00E-04  2.00E-06
MATERIAL      2  69.3E+06 .33  8.40-04  2.00E-04  2.00E-06
MATERIAL      3  10.0E+06 .45  7.50-04
CONSTRAINT    1    000.0  000.0
CONSTRAINT     5    0.000E+00 0.000E+00
CONSTRAINT     6    0.000E+04 0.000E+04
CONSTRAINT     8    0.000E+00 0.000E+00
CONSTRAINT    11    0.000E+00 0.000E+00
CONSTRAINT    15    0.000E+00 0.000E+00
CONSTRAINT    17    0.000E+04 0.000E+04
CONSTRAINT    18    0.000E+00 0.000E+00
CONSTRAINT    21    0.000E+00 0.000E+00
ADDMASS       4    32.00E-06 1.500E-06 2.700E-06
ADDMASS       5    68.00E-06 4.100E-06 5.800E-06
ADDMASS       6    62.00E-06 3.600E-06 5.300E-06
ADDMASS       7    26.00E-06 1.200E-06 2.200E-06
ADDMASS      16    26.00E-06 1.200E-06 2.200E-06
ADDMASS      17    62.00E-06 3.600E-06 5.300E-06
ADDMASS      18    68.00E-06 4.100E-06 5.800E-06
ADDMASS      19    32.00E-06 1.500E-06 2.700E-06

```

Input File for Rotor - Internal Damping Included, With Constraints

ELEMENT	1	3	0.500	0.3125			
ELEMENT	2	1	0.675	0.3748			
ELEMENT	3	1	0.675	0.3748			
ELEMENT	4	2	0.360	0.3748			
ELEMENT	5	2	0.500	0.3748			
ELEMENT	6	2	0.440	0.3748			
ELEMENT	7	1	1.000	0.3748			
ELEMENT	8	1	1.000	0.3748			
ELEMENT	9	1	1.000	0.3748			
ELEMENT	10	1	1.000	0.3748			
ELEMENT	11	1	1.000	0.3748			
ELEMENT	12	1	1.000	0.3748			
ELEMENT	13	1	1.000	0.3748			
ELEMENT	14	1	1.000	0.3748			
ELEMENT	15	1	1.000	0.3748			
ELEMENT	16	2	0.440	0.3748			
ELEMENT	17	2	0.500	0.3748			
ELEMENT	18	2	0.360	0.3748			
ELEMENT	19	1	0.625	0.3748			
ELEMENT	20	1	0.625	0.3748			
MATERIAL	1		29.5E+06	.33	7.27-04	2.00E-04	2.00E-06
MATERIAL	2		69.3E+06	.33	8.40-04	2.00E-04	2.00E-06
MATERIAL	3		10.0E+06	.45	7.50-04		
CONSTRAINT	1		000.0	000.0			
CONSTRAINT	5		0.000E+00	0.000E+00			
CONSTRAINT	6		5.000E+01	5.000E+01	1.500E-02	1.500E-02	
CONSTRAINT	8		0.000E+00	0.000E+00			
CONSTRAINT	11		0.000E+00	0.000E+00			
CONSTRAINT	15		0.000E+00	0.000E+00			
CONSTRAINT	17		5.000E+01	5.000E+01	1.500E-02	1.500E-02	
CONSTRAINT	18		0.000E+00	0.000E+00			
CONSTRAINT	21		0.000E+00	0.000E+00			
ADDMASS	4		32.00E-06	1.500E-06	2.700E-06		
ADDMASS	5		68.00E-06	4.100E-06	5.800E-06		
ADDMASS	6		62.00E-06	3.600E-06	5.300E-06		
ADDMASS	7		26.00E-06	1.200E-06	2.200E-06		
ADDMASS	16		26.00E-06	1.200E-06	2.200E-06		
ADDMASS	17		62.00E-06	3.600E-06	5.300E-06		
ADDMASS	18		68.00E-06	4.100E-06	5.800E-06		
ADDMASS	19		32.00E-06	1.500E-06	2.700E-06		